IS-T--1565

DE91 016160

# Single Vortex Motion and Elementary Pinning Force in SNIS Josephson Junctions

by

Li, Qiang

PHD Thesis submitted to Iowa State University

Ames Laboratory, U.S. DOE

Iowa State University

Ames, Iowa 50011

Date Transmitted: July 18, 1991

PREPARED FOR THE U.S. DEPARTMENT OF ENERGY

UNDER CONTRACT NO. W-7405-Eng-82.

# DISCLAIMER

# Single vortex motion and elementary pinning force in SNIS Josephson junctions

Qiang Li

Under the supervision of Dr. D. K. Finnemore
From the Department of Physics and Astronomy
Iowa State University

A new family of superconductor - normal metal - insulator - superconductor (SNIS) Josephson junctions has been developed to study the motion of a single Abrikosov vortex under the influence of a Lorentz force from an applied transport current. The location of the vortex within the junction is determined by the diffraction pattern. Methods have been developed to nucleate a single vortex by applying a transport current in one strip of the junction and systematically to push the vortex to nearly any desired location within the junction by applying currents in either of the cross-strip legs of the junction. The vortex in thin film Pb was found to move stepwise from one pinning center to another. The average distance separating pinning centers in thin film Pb is about 1.0 $\mu$m. The elementary pinning force $f_p$ for a vortex in a pure Pb film was measured to be on the order of $10^{-13}$ N at reduced temperature $t=T/T_c=0.9$, which is about one order of magnitude smaller than that for a Pb-Bi film at this reduced temperature. The temperature dependance of $f_p$ was found to be $f_p \sim (1-T/T_c)$ above 6.5 K and $f_p \sim (1-T/T_c)^{2/3}$ below 6.5 K. The feasibility of using the motion

# Single vortex motion and elementary pinning force in SNIS Josephson junctions

by

Qiang Li

A Dissertation Submitted to the
Graduate Faculty in Partial Fulfillment of the
Requirements for the Degree of
DOCTOR OF PHILOSOPHY

Department: Physics and Astronomy
Major: Solid State Physics

Approved:

In Charge of Major Work

For the Major Department

For the Graduate College

Members of the Committee:

Iowa State University
Ames, Iowa

1991

of a single vortex to store information and perform logic has been investigated. Since the Josephson voltage is in the range of tens of millivolts, the read and write operations can be done with rather simple electronics.

TABLE OF CONTENTS

# CHAPTER 1. INTRODUCTION

The pinning of magnetic flux in superconductors is a subject of intense study for both fundamental physics and practical applications. Basically, the pinning is accomplished by the flux lines interacting with defects which change the local superconducting properties.

Numerous works have been devoted to the study of various flux pinning mechanisms that can be effective. A. T. Larkin and Y. N. Ovchinnikov[1] attribute the flux pinning to the breakdown of long-range order of the flux line lattice due to the randomly distributed pinning sites, such as dislocations, voids, precipitates. The calculation made by Thumberg et al.[2] shows the enhanced electron scattering at the grain boundary. The difference of $H_{c2}$ across the grain boundary from the anisotropy was proposed by A. M. Campbell and J. E. Evetts[3] to be one of the causes of the flux pinning. It is the change in the Ginzburg-Landau free energy of the mixed state as the vortex moves across the boundary that leads to a pinning force. P. H. Kes[4] has given an excellent review of the flux pinning, both theoretical and experimental, in conventional superconductors.

In the high $T_c$ cuprate superconductors, the high operating temperatures, combined with large anisotropies and short coherence length, provide new features that can alter the nature of the superconducting properties and the mechanism by which flux lines are pinned. Recently, many other sources of pinning centers were proposed, for instance: the oxygen vacancies in the Cu-O layers,

suggested by Daeumling et al.[5]; a large density of local defects on the $CuO_2$ planes, proposed by Hylton and Beasley[6]; twin planes suggested by Dolan et al.[7]

Somehow, many problems related to the flux pinning mechanism, in both conventional and high $T_c$ superconductors, still remain unsolved. It is necessary to identify experimentally all those kinds of pinning centers individually, and to measure their strength $f_p$ so as to characterize them. However, the majority of the experimental investigations of the flux line pinning mechanism has been focused on the collective pinning behavior, where the volume pinning force $F_p$ (the pinning force/unit volume) is measured[8]. $F_p$ is a summation over all vortices of the individual forces which act on each vortex, while taking into account the vortex-vortex interaction[1]. Most superconducting material studied often contains more than one type of pinning center, which can not be easily distinguished from each other just from the measured $F_p$. Furthermore, most of the studies have been carried out in the high field regime, where the interactions between vortices are rather strong, which complicates the relationship between $F_p$ and the elementary pinning force $f_p$ produced by each pinning center[9]. Nevertheless, $f_p$ characterizes the individual pinning behavior. It is this fundamental quantity that can be used to compare directly the strengths of various kinds of pinning centers in different materials without the complication of interacting vortices. Thus, experimental studies on an isolated single vortex are essential to the understanding of the flux pinning mechanism.

Flux pinning and motion is another big issue with regard to applications of superconducting materials. Strong pinning is desirable to fabricate conductors able to carry large current density as used in transmission lines, high-field magnets, and magnetic resonance imaging (MRI) devices. Sensitive superconducting electronics, on the other hand, usually operates in low fields. The motion of a few vortices can be a serious problem because of the noise produced and other anomalies. All of these problems are closely related to the properties of $f_p$ with respect to the specified material and application. It is therefore necessary to have a relatively convenient technique for the experimental study of single vortex motion and measurement of $f_p$. To achieve such a goal motivates the present research.

Some measurements of $f_p$ have been carried out by several groups using different techniques. First, Mannhart et al.[10] used low temperature scanning electron microscopy to image trapped magnetic flux quanta through imaging the supercurrent distribution in Josephson tunnel junction. Extending this technique, they have been able to expose the flux quanta to external forces and observe their resulting displacement on the video-screen of the microscope. They found the elementary pinning force $f_p \sim 10^{-6}$ N/m for a 300 nm thick Pb-5 wt% In film that was the top electrode in an SIS Josephson junction. This technique however requires sophisticated experimental equipment and it has difficulty increasing the image resolution high enough to give the location of the flux quanta. A second type of measurement of the

elementary pinning force was performed by DasGupta and co-workers.[11] They prepared a bicrystal of Nb and studied the pinning of vortices trapped on the grain boundary. Although their work was at high field (≈2800 Oe), the special geometry of the bicrystal allowed them to avoid contributions from interactions between vortices and obtain a value for the elementary pinning force, $f_p \approx 7 \times 10^{-6}$ N/m at 4.2 K. However, the unusual geometry of the sample restricts the application of this method. In the third type of measurement, Allen and Claassen[12] used an rf-biased SQUID system with a pickup coil to detect moving flux and found $f_p \sim 10^{-7}$ N/m, and $f_p \sim (1-T/T_c)^{2.7}$ for a 20 nm thick Nb single crystal film (MBE deposited). For a polycrystalline film, they found $f_p \sim 10^{-6}$ N/m, and $f_p \sim (1-T/T_c)^{3.5}$. They proposed that dislocations are the pinning centers in the low pinning film, while grain boundaries are the pinning centers in the high pinning film.

Using a different method, Hyun, Finnemore et al.[13] directly measured the elementary pinning force of a single vortex trapped in a Pb-2.5 at% Bi thin film. The PbBi films were made as the superconducting electrodes of an SNS Josephson junction. A single vortex was successfully trapped inside one layer of the Pb-Bi films through the field cooling process. The $f_p$ was studied by measuring the minimum amount of depinning current applied to remove the vortex from one trapped site. It was found that $f_p$ varied for different sites, but was on the order of $10^{-6}$ N/m near $T_c$, and $f_p \sim (1-T/T_c)^{3/2}$. The cause of pinning there was not identified, but it was speculated to be due to the Bi precipitates.

Each method of $f_p$ measurement, as mentioned above, has its own advantage and experimental conditions. The one originated by Hyun et al. is particularly interesting because only a single vortex is involved and the location of the vortex is determined by simple voltage measurements. It is not only able to measure $f_p$ but also able to find the vortex location precisely.

The basic idea for locating the vortex inside Josephson junctions was given by Miller et al.[14] in 1985, through measuring both the parallel and perpendicular magnetic field dependence of the maximum Josephson current (so-called diffraction pattern). The Josephson tunneling current is strongly affected by the local magnetic field enclosed in the junction barrier through the induced phase difference across the junction from the wave function of two superconducting electrodes. A particular vortex configuration inside the junctions gives rise a unique field distribution in the barrier. Such a vortex field together with its external field generates a specified phase term, that, in turn, changes the Josephson current density distribution in such a way that the diffraction pattern functions as a fingerprint of the vortex configuration inside the junction. The unique connection between the location of the vortex and the $I_c$ vs $H_{/}$ curves makes it possible to determine the location of the vortices. The experiment performed by Hyun and Finnemore[13,15] shows excellent accuracy in locating the vortex (within 1% of the junction width). With the success of the precise determination of the vortex location, a conceptual framework for a flux shuttle had been

demonstrated to be able to serve as a memory device.

However, the experiment was done in an SNS Josephson junction which has a junction resistance in the micro-ohm range, so that a SQUID had to be used to detect the voltage signal on the order of a few tenths of a nanovolt. From a practical point of view, this makes the devices slow and rather difficult to use in large junction arrays. A higher junction impedance is needed in order to apply these ideas with conventional electronics. Consequently, an insulator layer has to be introduced to increase the junction impedance at least to a few tenths of an ohm. The problem whether the single vortex can be formed and moved in an SINS junction as well as in an SNS junction has to be studied.

The long-term goal of the present research is to develop a new family of Josephson junctions suitable for an Abrikosov vortex memory. The basic circuit element will have a stacking sequence Pb-Al-$Al_xO_y$-PbBi. The short-term goals are to work out the basic physics of locating the vortex and moving it from place to place in this SNIS junction. This also will give a measure of $f_p$ for Pb thin film.

A large part of the present research is similar to the previous work by O. B. Hyun[16] who investigated single vortex motion in an SNS Josephson junction made of PbBi(2.5 at%)-AgAl(4 at%)-PbBi(2.5 at%). The theory used to locating the vortex inside a Josephson junction was addressed thoroughly there and is essentially the same as being applied here. The new work here involves the introduction of an insulating layer, the development of methods for pushing the vortex in

any desired direction, and the measurement of $f_p$ in a low pinning material where grain boundaries are expected to dominate.

In Chapter 2, the theory of locating the vortex inside Josephson junctions will be discussed briefly. The detailed experimental techniques will be presented in Chapter 3. A large part of this chapter will be devoted to the equipment set-up for sample preparation, as well as to the electronics used for measurement. In addition, the basic properties of this new family of junctions also will be discussed there. Chapter 4 will contain the main experimental results. There, we will show how a single vortex was created successfully by the nucleation process, and pushed to the most desired locations within the junction by applying currents in either leg of this cross-strip junction. The measurement of the elementary pinning force $f_p$ for a vortex trapped in a thin film Pb will be presented, as well as the temperature dependence of $f_p$. The results will be discussed and compared to those found in PbBi thin film by Hyun et al.[13,15] At end of this chapter, some future work by means of this technique will be proposed. In the final chapter, conclusions will be given.

# CHAPTER 2. THEORY AND MODELS

We begin this chapter with the description of the nature of the magnetic field dependence of the Josephson current, the so-called Fraunhofer pattern. Then we will present the theory, which explains how the pattern may be distorted by the trapped vortex inside the Josephson junction. The distorted Fraunhofer pattern is usually called the diffraction pattern of the vortex. It will be shown that such a diffraction pattern can be used as a fingerprint to determine the location of the vortex.

## 2.1 Magnetic Field Dependence of the Critical Current

When two superconductors are brought close enough to one another, Cooper pair tunneling can occur from one side to another without a bias voltage across the junction. Such a current carried by the Cooper pairs is called the Josephson current. The Josephson current density in the z-direction for an SNIS Josephson junction that lies in the x-y plane is expressed by the following equation,

$$J_z(\mathbf{r}) = J_o \cdot \sin\gamma(\mathbf{r}) \ , \qquad (2.1)$$

where $\gamma(\mathbf{r})$ is the gauge invariant phase difference across the junction at the polar coordinate $\mathbf{r}$, and $J_o$ is the temperature-dependant amplitude which characterizes the Josephson tunneling.

As a function of local magnetic field inside the junction, the

phase $\gamma$ varies as[17]

$$\frac{\partial\gamma(r)}{\partial x}\hat{\underline{x}}+\frac{\partial\gamma(r)}{\partial y}\hat{\underline{y}} = \left(\frac{2\pi d_{eff}}{\Phi_o}\right)H\times\hat{\underline{z}} \ , \tag{2.2}$$

where $\Phi_o$ is one flux quantum, $2.07\times10^{-7}$ gauss-cm$^2$, $d_{eff}=t+\lambda_{L1}+\lambda_{L2}$ is the effective thickness, t is the physical thickness of the barrier, $\lambda_L$ is the effective London penetration depth of the superconducting thin film forming the junction. The subscripts 1 and 2 denote the bottom and the top superconducting layers respectively. Here, the thickness of each superconducting film is assumed larger than twice its penetration depth.

This phase and field relation, represented by Eq. 2.2, together with Eq. 2.1, can be combined with the Maxwell equation,

$$\nabla\times\boldsymbol{H} = \frac{4\pi}{c}\boldsymbol{J}+\frac{1}{c}\frac{\partial\boldsymbol{D}}{\partial t} \ ,$$

to give a two-dimension time-dependant sine-Gordon equation[18]. In the steady state it reduces to

$$\frac{\partial^2\gamma}{\partial x^2}+\frac{\partial^2\gamma}{\partial y^2} = \frac{\sin\gamma}{\lambda_J^2} \ , \tag{2.3}$$

where $\lambda_J=[\hbar c/(8\pi e d_{eff}J_o)]^{1/2}$ is the Josephson penetration depth. It defines the length within which d.c. Josephson currents are confined near the edges of the junction. When $\lambda_J$ is larger than the size of the junction W (small junction limit), the current density throughout the junction area is nearly uniformly distributed. In most of our experiments, $\lambda_J$ is larger than the width of the junction; ie. $\lambda_J\geq W$. In addition, $J_o$ will be assumed to be constant within the junction area. The occasion where $J_o$ should not be taken as a constant will be pointed

out later.

By integrating Eq. 2.2, we obtain the phase as

$$\gamma(\mathbf{r}) = \gamma_o + \theta(\mathbf{r}) \ , \tag{2.4a}$$

where $\gamma_o$ is a field-independent constant, and the magnetic-field-dependent phase angle $\theta(\mathbf{r})$ is given by

$$\theta(\mathbf{r}) = 2\pi\cdot[\Phi(\mathbf{r})/\Phi_o] \ , \tag{2.4b}$$

and

$$\Phi(r) = d_{eff}\cdot\iint_S H\cdot(\hat{z}\times dr) \ , \tag{2.5}$$

where $\Phi(\mathbf{r})$, given in Eq. 2.5, is the total flux enclosed in the area, S, defined by the junction width and effective thickness $d_{eff}$. After inserting Eq. 2.4a in Eq. 2.1, and integrating over the area S, we obtain the total current

$$I = \sin\gamma_o\iint_S dxdy[J_o\cdot\cos\theta(x,y)] + \cos\gamma_o\iint_S dxdy[J_o\cdot\sin\theta(x,y)] \tag{2.6a}$$

or

$$I = I_1\sin\gamma_o + I_2\cos\gamma_o \ , \tag{2.6b}$$

where $I_1$ and $I_2$ are the cosine and sine integrations over the area S respectively. Maximization of Eq. 2.6b with respect to $\gamma_o$ gives the maximum Josephson current, or the critical current, normalized to the maximum zero-field Josephson current, $I_o=\iint_S J_o dxdy$, as

$$I_c/I_o=[\langle\sin\theta(x,y)\rangle^2 + \langle\cos\theta(x,y)\rangle^2]^{1/2} \ . \tag{2.7}$$

Next we consider a square junction, of width W and effective thickness $d_{eff}$, sandwiched between two crossed superconducting strips. The junction lies in the x-y plane and is centered at the origin, such that it extends from $-W/2$ to $+W/2$ in both x and y directions and from $-d_{eff}/2$ to $+d_{eff}/2$ in the z direction. We also assume the small

junction limit, ie $\lambda_J > W$. Here we discuss two special cases where a uniform magnetic field is applied.

*1) Uniform field parallel to the junction*

Let us consider a constant field $H_y$ being applied along the y direction. The phase can be obtained from Eq. 2.4b as

$$\theta(x) = 2\pi d_{eff} H_y \cdot x/\Phi_o \ , \tag{2.8}$$

By inserting the above expression for $\theta(x)$ into Eq. 2.7, and performing the integral, we obtain the following equation,

$$\frac{I_c}{I_o} = \left| \frac{\sin(\pi\Phi/\Phi_o)}{\pi\Phi/\Phi_o} \right| , \tag{2.9}$$

in which the normalized critical current $I_c$ is expressed in terms of the total magnetic flux threading the junction barrier, $\Phi = W d_{eff} H_y$. As a function of $H_y$, $I_c$ oscillates in a familiar way known as the Fraunhofer pattern.

Equations 2.8 and 2.9 also can be expressed in terms of the parallel field needed for one flux quantum threading the junction barrier, $H_o$, as

$$\theta(x) = 2\pi \cdot (H_y/H_o)(x/W) \ , \tag{2.10}$$

and

$$\frac{I_c}{I_c} = \left| \frac{\sin(\pi H_y/H_o)}{\pi H_y/H_o} \right| , \tag{2.11}$$

Specifically, $H_o$ is given by $H_o = \Phi_o/(d_{eff} W)$, a quantity defined by the junction geometry only. It is important to know that when $H_y$ reaches a

value equal to n times $H_o$ (where n = ±1, 2, ...), the critical current, $I_c$, drops to zero.

*2) Uniform field perpendicular to the junction*

In the case where a uniform field is applied perpendicular to the junction, screening currents are induced at the surface of the superconducting films. These currents, in turn, generate the local magnetic field parallel to the plane of the junction, which changes the phase $\gamma(x,y)$ across the junction, and then alters the Josephson current density. Miller et al.[6] worked out appropriate expressions for the local field and phase terms. To a first approximation, $\theta(x,y)$ is given as

$$\theta(x,y) = -8\pi\cdot\left(\frac{H_z}{H_o}\right)\cdot\left(\frac{xy}{W^2}\right) . \tag{2.12}$$

The critical current can be calculated by inserting Eq. 2.12 into Eq. 2.7. The result, expressed in terms of sine integral, is

$$\frac{I_c}{I_o} = \left|\frac{Si(\alpha)}{\alpha}\right| , \tag{2.13}$$

where

$$Si(\alpha) = \int_0^{\alpha}\cdot\frac{\sin(x)}{x}dx, \quad \alpha = 2\pi\cdot\frac{H_z}{H_o} .$$

$I_c$ decreases quadratically as $H_z$ increases at low field ($\alpha<<1$), and as $1/H_z$ at large field ($\alpha>>1$). The width of the central peak is approximately $H_o$. This behavior was confirmed experimentally by Miller et al.[6] using their SNS Josephson junctions.

## 2.2 Diffraction Pattern of Trapped Vortices

Consider a vortex only trapped in the bottom superconducting layer of a Josephson junction as illustrated in Fig. 2.1. Since the top superconducting layer expels the flux from the vortex, the flux lines have to be confined in the barrier, and leak out of the edge of the junction. The confined flux produces a magnetic field, $H_{vortex}(\mathbf{r})$, parallel to the junction, as shown in Fig. 2.1. $H_{vortex}(\mathbf{r})$ has spatial dependence on the position of the vortex at $\mathbf{r}_{\pm}$, and is given by[14]

$$H_{vortex} = \pm \frac{\phi_0}{2\pi|\mathbf{r}-\mathbf{r}_{\pm}|} \cdot \frac{(\mathbf{r}-\mathbf{r}_{\pm})}{|\mathbf{r}-\mathbf{r}_{\pm}|} , \tag{2.14}$$

where the "+" or "−" signs are associated with a positive or negative vortex respectively. If an additional external field, $H_x$, is present, the total field, $H_T$, by superposition, is

$$H_T = H_x + H_{vortex}(\mathbf{r})$$

Consequently, the phase difference across the junction changes so that the Josephson current density has to redistribute according to the vortex location. If a uniform external field is applied in the presence of a vortex, the Fraunhofer pattern will be distorted in a way uniquely determined by the vortex configuration. In this section, we will briefly present the theory used to locate the vortex configuration by measuring its diffraction pattern. A rather detailed discussion of this theory can be found in the previous work done by O. B. Hyun[16].

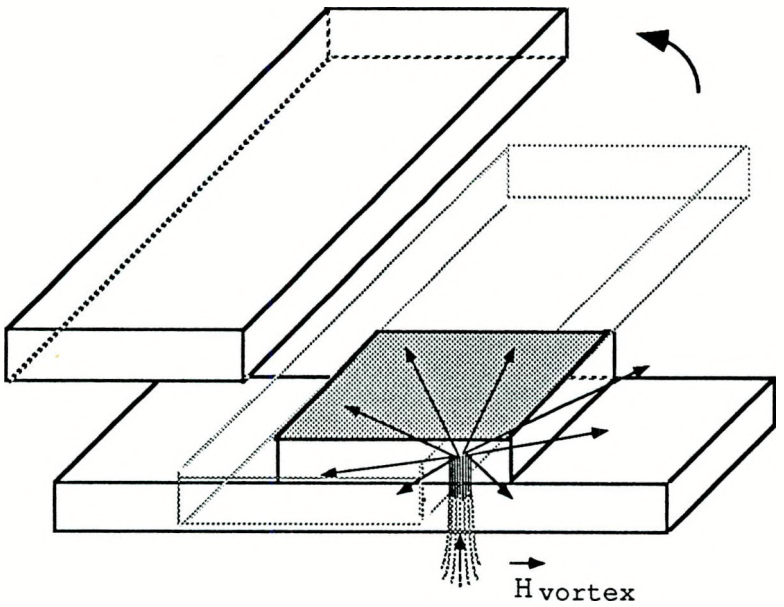


Fig. 2.1. A sketch shows magnetic flux lines generated by a vortex trapped in the bottom superconducting layer of a Josephson junction, where the top superconducting layer has been lifted up to show the flux lines in the barrier which are parallel to the junction

When a single vortex is trapped inside a junction, as shown in Fig. 2.1, the inner pole acts like a source (or a sink) of magnetic flux with total flux equal to $\Phi_0$. The outer pole is completely shielded by the superconductor so that it does not have any influence on the local magnetic field within the barrier. As far as this local field is concerned only, such a single vortex may be approximated as a magnetic monopole. It is assumed here that the core size of the vortex is much smaller than the size of a junction.

Two types of vortex need to be distinguished here. A positive vortex acts like a source of magnetic flux. Similarly, a negative vortex corresponds to a sink of magnetic flux. Their relations are illustrated in Fig. 2.2.

Now, we present the basic assumptions used in the theory. Later, we will not specify them during the theoretical treatment.

*Assumptions*

(a) The magnetic coupled vortex (or dipole) is assumed to be a linear superposition of two single vortices. (Fig. 2.2c)

(b) The single vortex can be approximated by a magnetic monopole charge. (Fig. 2.2d)

(c) Individual single vortices are independent from each other, so that the total field arising from the vortices inside a junction is the linear superposition of the fields contributed by all individuals.

(d) The total phase difference across the junction is assumed to be the linear superposition of phases contributed by all individual vortices plus the external field.

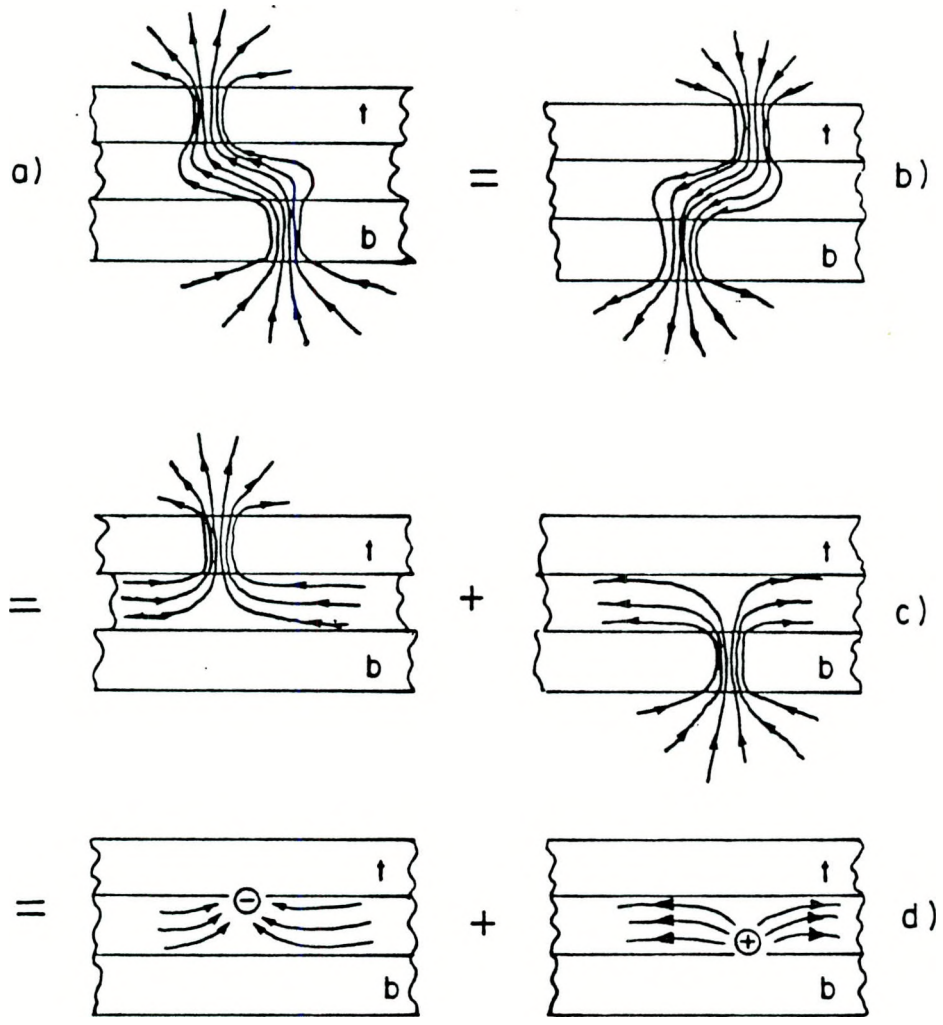


Fig. 2.2. Theoretical treatment of a vortex

(a) A misaligned dipole vortex in a junction. t and b denote the top and bottom superconductor respectively

(b) Theoretically equivalent dipole to (a). The theory treats the flux lines inside the junction only

(c) Linear superposition

(d) Magnetic monopole charge approximation

Now, let's consider the field and phase produced by a single vortex at $\mathbf{r}_{\pm}$, shown in Fig. 2.3, where the + sign is associated with a positive vortex, the − sign with a negative one. The magnetic field intensity at $\mathbf{r}$ due to the vortex is given by Eq. 2.14.

$H_{vortex}$ is radial in the x–y plane, centered at $\mathbf{r}_{\pm}$. The magnetic flux enclosed in the area between the z axis and $\mathbf{r}$ is $\Phi_{\pm}=\pm\Phi_0\cdot(\theta_{\pm}/2\pi)$, where $\theta_{\pm}$ is the angle between $-\mathbf{r}_{\pm}$ and $\mathbf{r}-\mathbf{r}_{\pm}$, shown in Fig. 2.3. The significance of $\theta_{\pm}$ becomes obvious when the phase at $\mathbf{r}$ is calculated from Eq. 2.4. It exactly represents the relative phase at point $\mathbf{r}$ caused by the vortex at $\mathbf{r}_{\pm}$. After a simple calculation, and properly choosing the constant $\gamma_0$, we find that the phase at $\mathbf{r}$ can be written as

$$\theta_{\pm}(x,y) = -\tan^{-1}\left(\frac{y-y_{\pm}}{x-x_{\pm}}\right) . \tag{2.15}$$

The total phase from all individual vortices is

$$\theta_v(\mathbf{r})=\Sigma_+\theta_+(\mathbf{r})-\Sigma_-\theta_-(\mathbf{r}) . \tag{2.16}$$

The above expression is deduced without considering the boundary conditions; that is, Eq. 2.16 assumes infinite extent of the planar films. Actually, when a single vortex is trapped in a junction, screening currents are generated to expel the vortex field from penetrating into the interior of superconducting layers. Near the vortex, screening currents are circular, while at the boundary of the junction, they must be parallel to the edge, since the currents can not flow outside of the junction. Therefore, the induced field will be perpendicular to the edge. This configuration can be achieved by

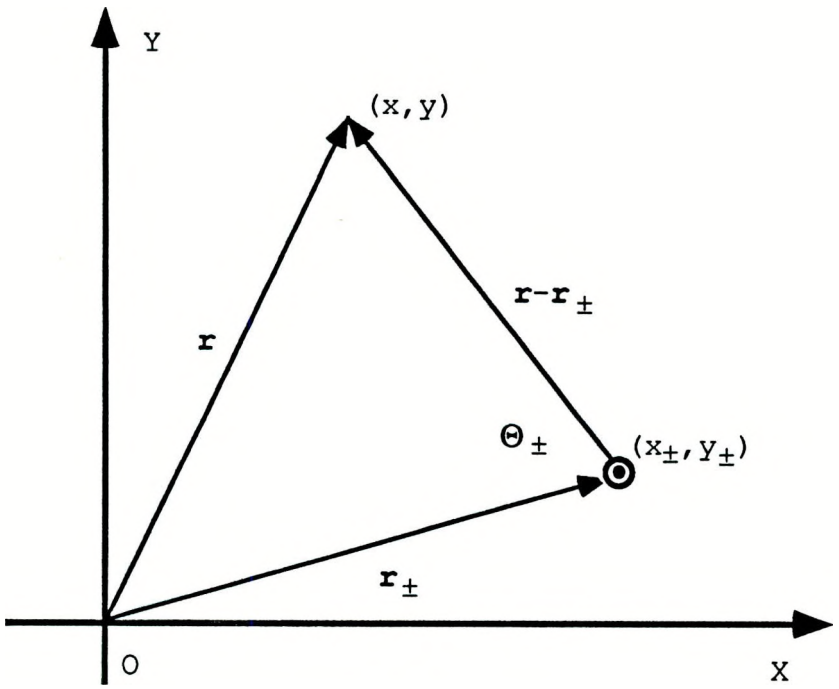


Fig. 2.3. Construction used to calculate the phase at **r** due to a vortex at $\mathbf{r}_{\pm}$. The angle $\Theta_{\pm}$ is just the relative phase at **r**

introducing image vortices outside the junction area.

By assuming the single vortex to be a magnetic monopole charge, the problem becomes mathematically the same as a 2-D electrostatic problem, where an electric charge is in a grounded rectangular box. The charge generates an infinite number of image charges outside the box. In the single vortex situation, an infinite number of image vortices are produced to form the image vortex lattice[16]. The actual phase due to the vortex will be the sum of that from the real vortex, plus an infinite number of image vortices:

$$\theta(\text{vortex}) = \theta(\text{real vortex}) + \Sigma_{all}\theta(\text{images}) \ , \qquad (2.17)$$

where each term can be calculated by using Eq. 2.15. According to Eqs. 2.14 and 2.15, those images further away from the point $\mathbf{r}_{\pm}$ contribute less to the phase change. An analytical solution has been obtained by J. R. Clem[19] which includes an infinite number of image vortices, and can be found in the previous work[16].

The phase term contributed by image vortices is not negligible, especially when the vortex is near the edge of the junction. The magnetic field line generated by a single vortex near the edge is strongly bent toward the edge and perpendicular to it in order to satisfy the boundary conditions. The phase induced by such a kind of field greatly differs from that of the single vortex in the infinitely large plane. Thus, the image correction is rather important. Hereafter, the phase and field produced by the vortex addressed in the following text should be considered to have been corrected by including all the images.

When an additional field **H** from an external source is present, the total phase induced can be obtained by linear superposition as

$$\gamma(x,y) = \theta_H(x,y) + \Sigma_{all}\theta_{vortex}(x,y) \ , \qquad (2.18)$$

where $\theta_H(x,y)$ is contributed by the external field **H**, while $\Sigma_{all}\theta_{vortex}(x,y)$ is due to all the vortices inside the junction area, including their images.

The diffraction patterns for both $I_c/I_o$ vs $H_x/H_o$, and $I_c/I_o$ vs $H_z/H_o$ due to trapped vortices can be obtained by substituting $\gamma(x,y)$ of Eq. 2.18 into Eq. 2.7 and performing the appropriate integrations in Eq. 2.7.

Shown in Fig. 2.4, are three theoretically calculated diffraction patterns corresponding to three different single vortex positions together with the perfect Fraunhofer pattern which represents no trapped vortex. It is easy to see that as the single vortex position gets closer to the center, the Fraunhofer pattern gets more severely distorted, and $I_c(H_x=0)$ becomes more suppressed and finally the central peak of $I_c$ vs $H_x$ splits into two parts. It is especially interesting to note that the value of $I_c$ at zero field diminishes to zero when the vortex is at the center.

The diffraction pattern changing as a function of the vortex position, **r**, can be better understood by means of critical current density, $J_c(\mathbf{r})$. Shown in Fig. 2.5a, is the normalized critical current density $J_c(r)/J_o$ for a positive vortex at $\mathbf{r}_+ = (0.01, 0.01)$, in reduced coordinates, near the center of the square junction. From Eq. 2.15, the phase due to this vortex changes from $-\pi$ to $\pi$ as the observing

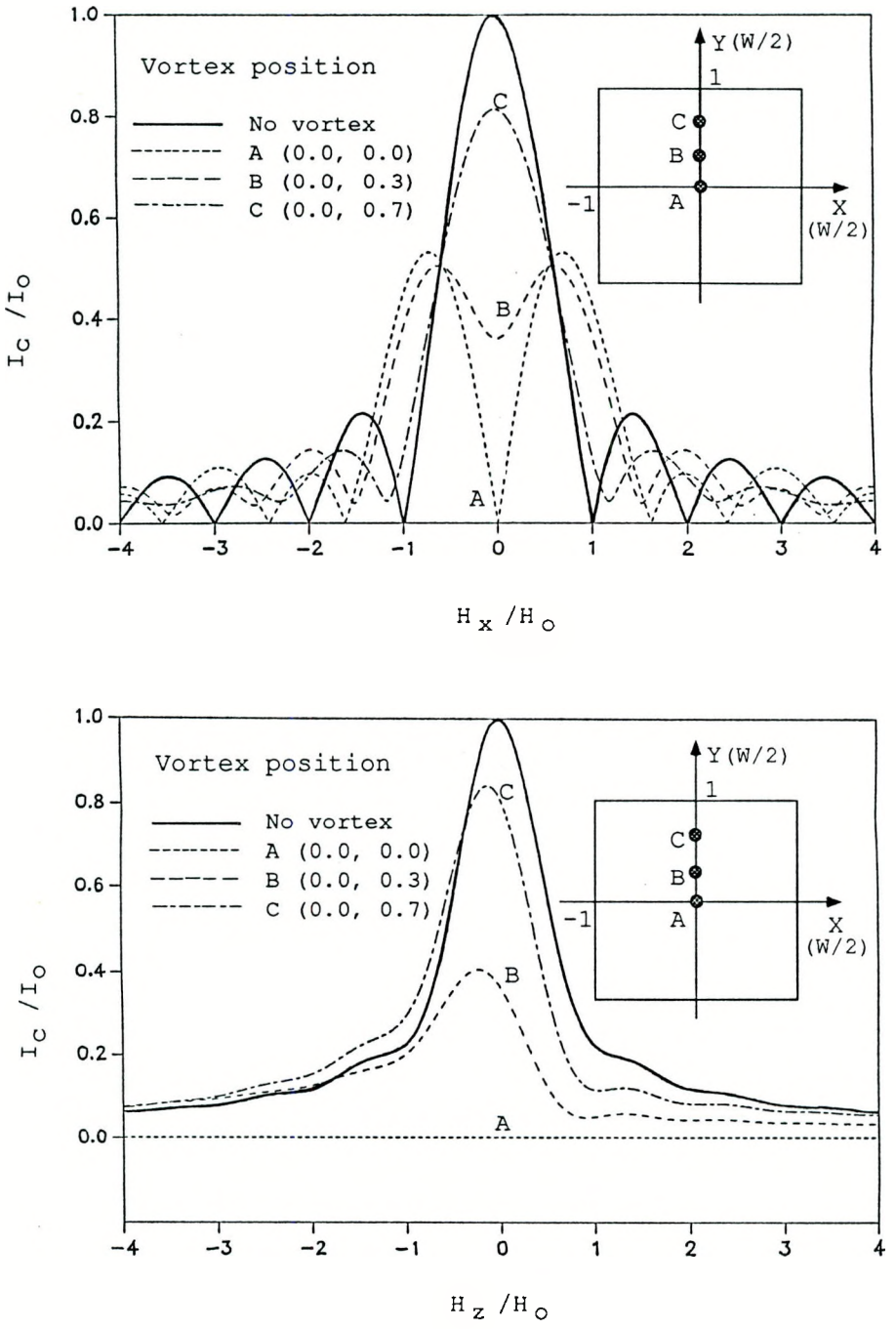


Fig. 2.4. Diffraction patterns, $I_c/I_o$ vs $H_x/H_o$, and $I_c/I_o$ vs $H_z/H_o$, for various single vortex positions

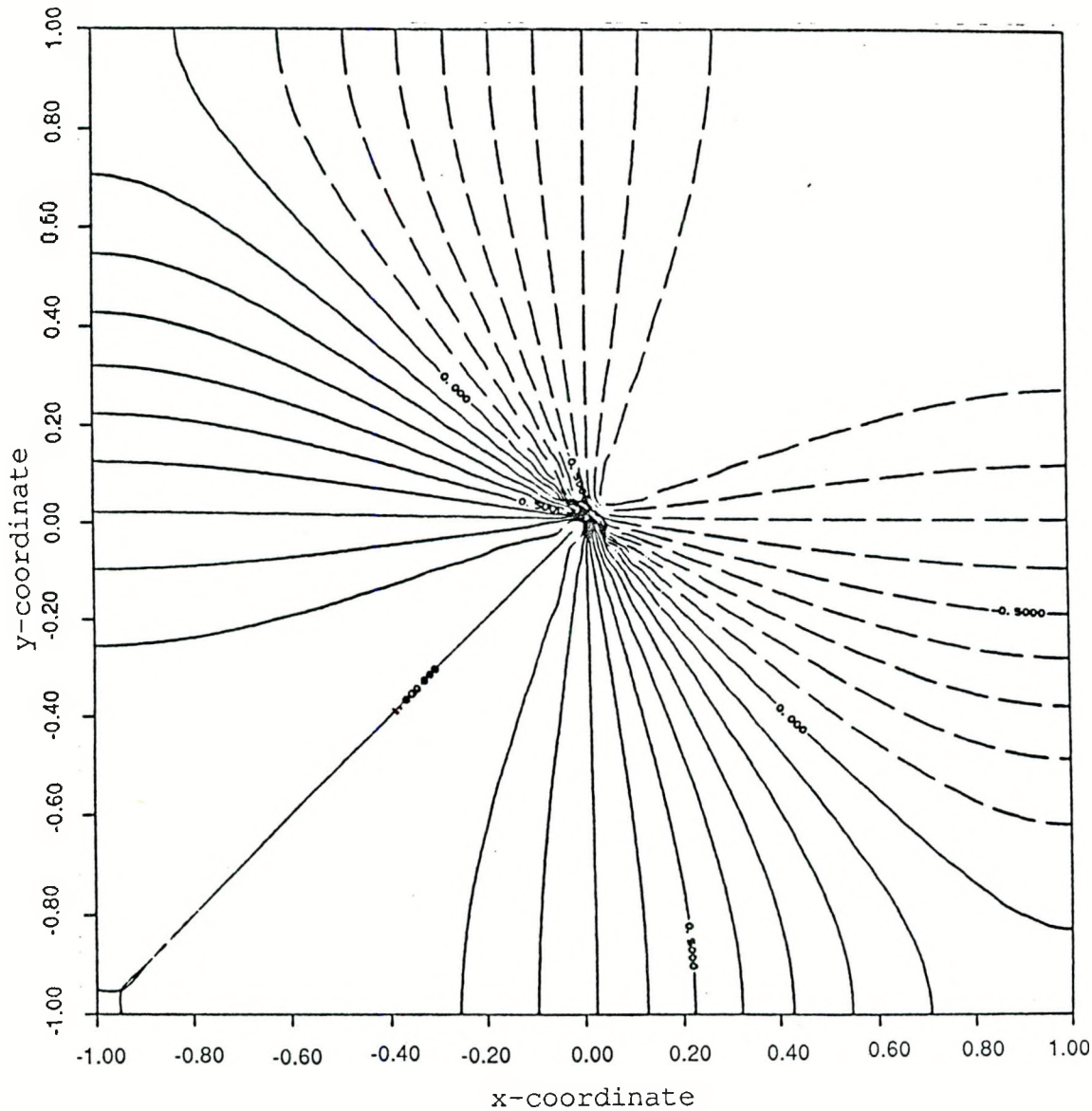


Fig. 2.5a. Normalized critical current density, $J_c(r)/J_o$, at zero field due to a positive vortex at (0.01, 0.01) in the unit of W/2

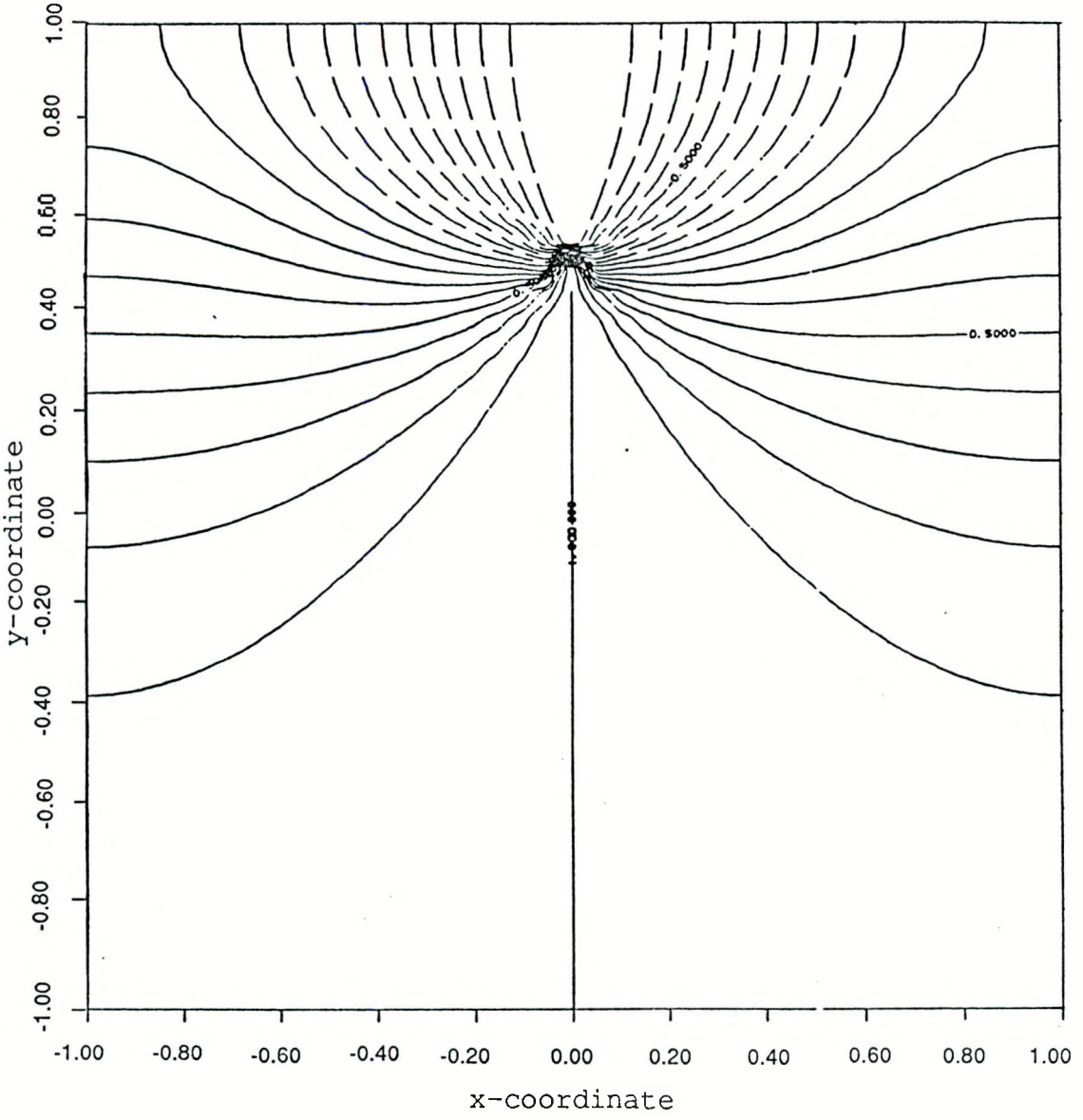


Fig. 2.5b. Normalized critical current density, $J_c(r)/J_o$, at zero field due to a positive vortex at (0.0, 0.5) in the unit of W/2

point moves around it and across the diagonal line of the first quadrant. Consequently, the Josephson current density changes from $-J_o$ to $J_o$, because it is the sine function of the phase term. The solid contour lines in Fig. 2.5 represent +J, while the broken lines represent −J. If the vortex is right in the center of the junction, $+J_o(\mathbf{r})$, the contribution from one half of the junction plane is exactly canceled by $-J_o(\mathbf{r})$, the contribution from the other half, and that results in zero total critical current $I_{co}$. As the vortex moves away from the center of the junction, the well balanced Josephson current density distribution is broken. Shown in Fig. 2.5b, is another plot of $J_c(\mathbf{r})/J_o$ for a positive vortex at (0.0, 0.5). The +J contribution corresponding to the solid contour lines occupies the most of the junction area, while the −J occupies about 20% of the total junction area. This makes the total Josephson current $I_{co}$ increase to 60% of $I_o$. Some detailed calculations and plots concerning the Josephson current density distribution by many other trapped vortices have been worked out by O. B. Hyun[16]. Also in his work, a dipole was calculated to show less effect than a single vortex on the distortion of the perfect Fraunhofer pattern, because the magnetic fields from a dipole are localized approximately between the poles.

The vortex diffraction pattern is strongly affected by the parallel component of the vortex field inside the junction. When the vortex is near the edge, this component is quite well localized between the vortex and its nearest image, so that the influence to the perfect Fraunhofer pattern is weak. When the vortex gets near the

center, the image effect has little influence, so that the vortex field affects all the junction area. Hence, the diffraction pattern is severely distorted. Because each vortex has only one flux quantum involved, the most noticeable feature in the diffraction pattern of the Josephson junction containing a single vortex happens in a range of a few $H_o$, typically $H_x$ and $H_y$ in between $\pm 2H_o$. Most information needed to determine the vortex location is included in this low field data.

From the experimental point of view, the ratio of the critical current of a junction containing a vortex and having zero applied field, $I_{co}$, to the critical current of the same junction without a vortex and having zero applied field, $I_o$, is a very useful diagnostic tool to give the first sign of motion of a vortex. Shown in Fig. 2.6, is this ratio, $I_{co}/I_o$, monotonically decreasing as a function of the single vortex position changing from the edge of the junction to the center of the junction.

The geometrical symmetries[16] of a few vortex configurations in a junction can possibly produce the same diffraction pattern, which makes it difficult to correctly map out a vortex configuration. Shown in Fig. 2.7a is an example, where a two fold symmetric location of a single vortex with respect to the x axis produces the same diffraction pattern, $I_c$ vs $H_x$. By measuring an additional diffraction pattern, $I_c$ vs $H_y$, one can tell which one of the groups, shown in Figures 2.7b and 2.7c, is possible. The two fold antisymmetric locations shown in Figures 2.7b and 2.7c can be distinguished by the response of the

vortex to the external forces such as those caused by transport current or perpendicular field. In Chapter 4 section 4.2.3, we will give more detailed discussion on this symmetry problem by means of experimental results.

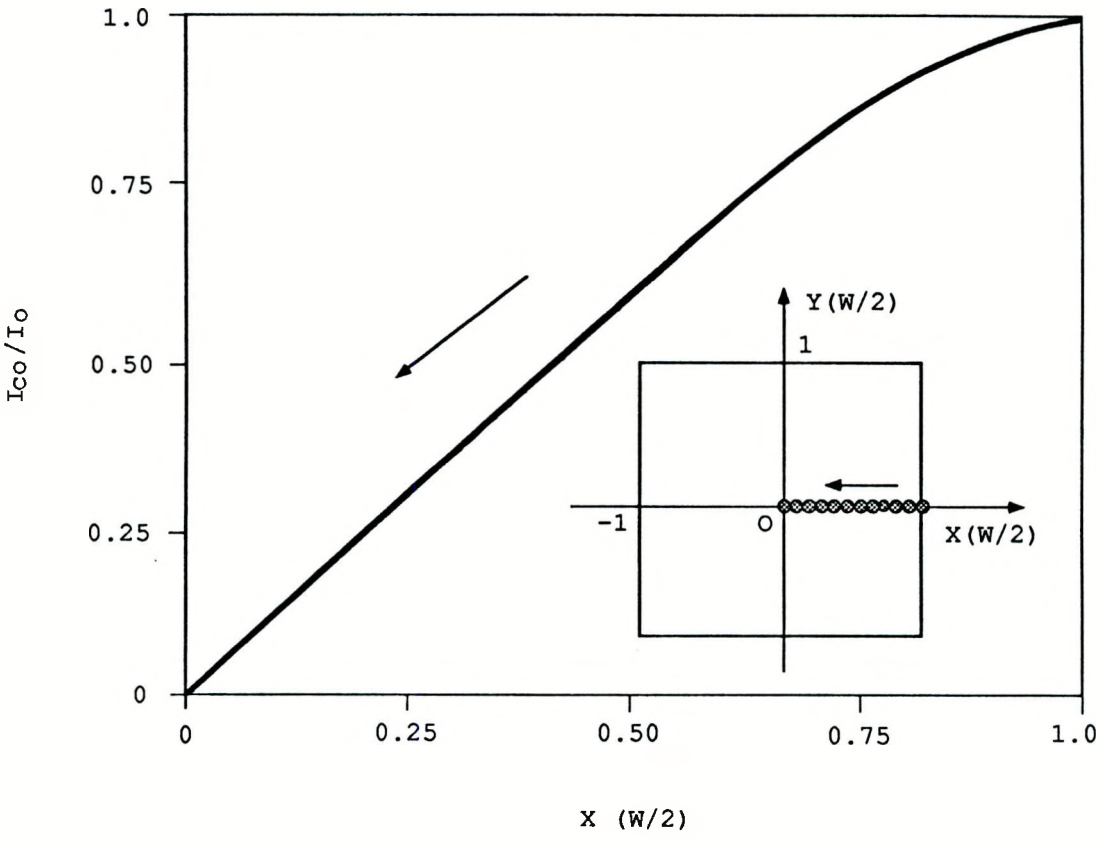


Fig. 2.6. $I_{co}/I_o$ monotonically changes as a function of the single vortex position in the junction. The insert shows a vortex progressing from the edge to the center

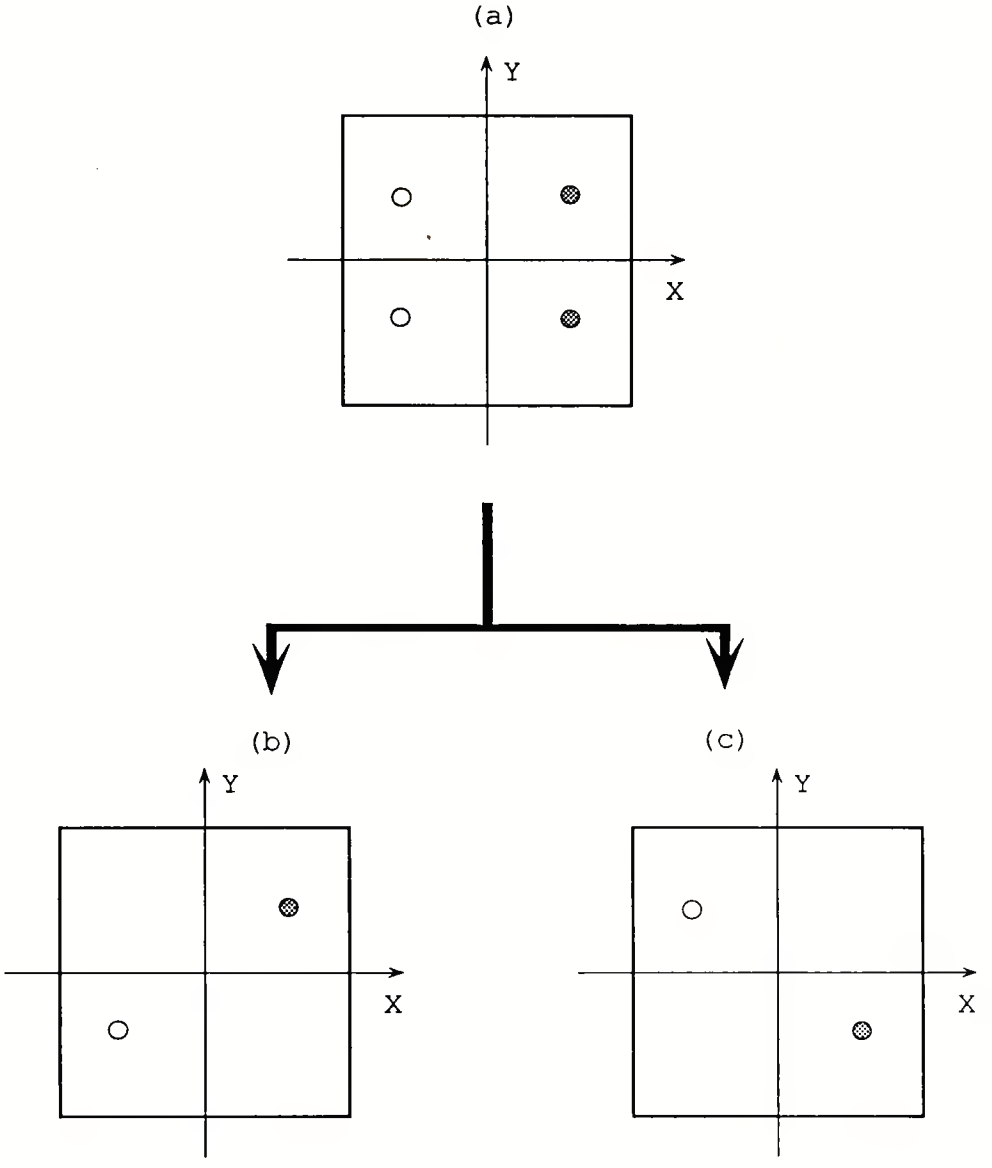


Fig. 2.7. Sketch to show that different vortex locations can produce the same diffraction patterns, where the vortex pole symbolized by O is opposite to that of ⊛. Any of the four locations in (a) has the same $I_c$ vs $H_x$ pattern. Two locations in either (b) or (c) give the same $I_c$ vs $H_x$ and $I_c$ vs $H_y$ patterns

# CHAPTER 3. EXPERIMENTAL TECHNIQUES AND CONDITIONS

In this chapter we will describe the detailed techniques of sample fabrication and data acquisition. The proper data analysis will be discussed, as well as basic properties of this type of Josephson junction.

## 3.1. Sample Fabrication and Experimental Condition

### 3.1.1. Sample Preparation

To make a good quality SNIS Josephson junction, the materials used have to be chosen carefully in order to meet several requirements. First, interface diffusion between the normal metal and superconducting films has to be minimized to provide a reproducible proximity effect. Second, the growth of an insulating layer has to be controllable so as to provide a uniform barrier thickness of a few atomic layers. Third, the materials used have to be capable of being thermally evaporated to form those desired thin films. Bearing these basic rules in mind, we finally decided to choose pure aluminum for the normal metal, since a native $Al_2O_3$ insulating layer can be grown right on the normal layer with rather high quality. For the superconducting electrodes, pure Pb or a Pb-Bi(2.5% a/o) alloy was selected, because the Al/Pb interface has been shown by A. Gilabert et al.[20] and P. Nedellee et al.[21] to yield reproducible proximity

effects.

Once the materials are chosen, the procedure of fabrication of a SNIS Josephson junction is important to ensure good quality. The entire cross strip SNIS junctions used in these experiments were prepared through successive evaporations, and oxidation in high vacuum without opening the vacuum chamber.

The Pb–Bi alloy was made by E. D. Gibson (EDG 8.151–3) in the Metallurgy and Ceramics Division of Ames Laboratory, USDOE, in the form of a rod. Its oxide layer outside the master rod was scratched off; then shiny pieces were cut off with a non-magnetic razor blade about 15 minutes before closing the evaporator. Small Pb chunks were prepared from a high purity (99.999%) Pb ingot (American Smelting and Refining Company) in the same way as for Pb–Bi. An aluminum ingot (high purity 99.999%, Alfa Products, Ventron) was cut and rolled into a 0.5 mm thick sheet. About 3x30 $mm^2$ long strips were cut from those sheets, cleaned, and etched in 10% NaOH solution for 2 minutes. Distilled water, acetone, methyl alcohol were used as the final rinses.

In Fig. 3.1, there is a sketch of the evaporation system used for sample preparation. High vacuum was normally maintained through a turbo pump on the order of $10^{-9}$ Torr. The plasma oxidation (or glow discharge) on the freshly deposited Al surface was done by a gaseous anodizing system[23], where a negative voltage Al ring having inner diameter of 11 cm was placed 3 cm below the substrate holder. Oxygen gas was supplied through a leak valve inlet. The discharge process

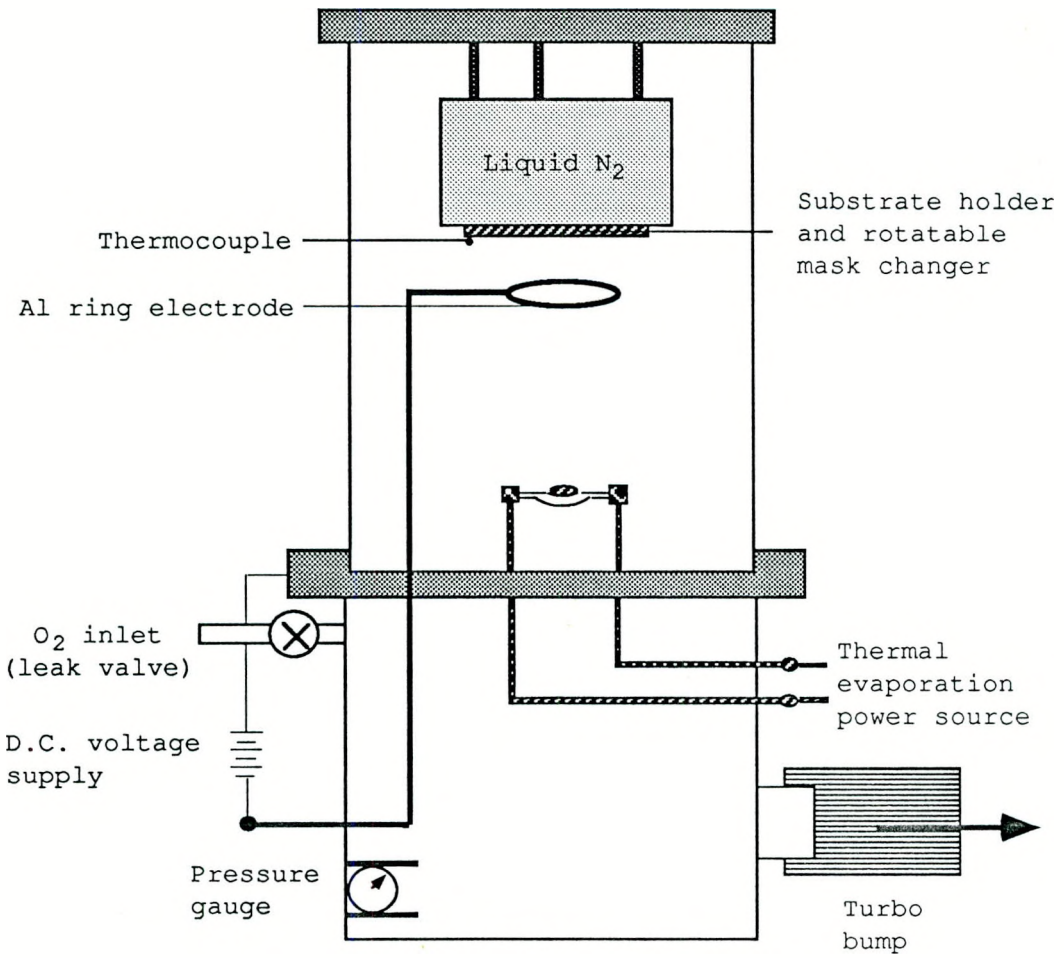


Fig. 3.1. A sketch of the evaporation system for sample preparation

was carried out by a high DC voltage source outside the chamber. A thermocouple is attached to the substrate holder for monitoring the temperature of the substrate. The sample holder was mounted right underneath a liquid nitrogen tank inside the vacuum chamber so that the superconducting and normal films could be deposited on a cold substrate to maintain a well-defined film and a clean interface between them. The rotatable mask changer was employed to rotate various masks for each film evaporation. During the last superconducting film deposition, the mask for the first superconducting film had been rotated by 90 degrees so that the two superconducting films had exactly the same width and were perpendicular to each other to form a cross strip junction. The substrate, Corning glass, 1.0" long, 0.5" wide, 0,048" thick, was cleaned in NaOH dilute solution, hot microcleaning solution and acetone-ultrasonic cleaner. In the evaporator, it was then attached to a copper block (1"x0.5"x0.5") with Apiezon-N grease. The copper block acts as a heat reservoir during evaporation. The substrate was always lifted by a string attached to the copper block in order to avoid scratching the pre-deposited film while changing the masks. The thickness of the film was controlled by a calibrated thickness monitor made of a quartz crystal oscillator and frequency meter. The real thickness of each films was measured by a sophisticated Tencor thickness profiler after all measurement were finished.

The mask for a superconducting layer was a slit of 55 $\mu$m wide, in a 25 $\mu$m thick steel plate. The distance between the mask and the

substrate was about 13 $\mu$m giving a sharp fall-off in the thickness at the edge. The mask for a normal layer is a plate about 75 $\mu$m thick with an open area (0.3mmx0.7mm).

The procedure for fabricating SINS Josephson junctions was usually strictly observed. The sequence is now given as follows:

1) The first strip of superconducting film was evaporated from an electrically heated molybdenum boat at a rate of about 50 Å/sec. The deposit condition is that the substrate was held at a stabilized temperature between -55°C and liquid nitrogen temperature, and at a pressure around $5x10^{-9}$ Torr, where the ionization gauge is located near the bottom of the chamber as shown in Fig. 3.1.

2) A pure Al film was evaporated from an electrically heated tungsten coil basket at a rate of 20 Å/sec, immediately after the first film was deposited. The pressure usually went up to $2x10^{-8}$ Torr during the deposition.

3) The substrate was warmed up to 5°C in 1~2 hours. Pure oxygen gas was fed in through a well controlled leak valve to 50 millitorr. The glow discharge was initiated by applying a D.C. voltage of about -400 volts to -500 volts on the aluminum ring. During 5 minutes of oxidation, the pressure varied less than 5%, the temperature of the substrate varied less than ±2°C.

4) Then the chamber was evacuated to a pressure below $1x10^{-7}$ Torr; liquid $N_2$ was filled into cold sink to cool the substrate down below -50°C again. After the pressure drops to $1x10^{-8}$ Torr, the last superconducting strip was deposited from another molybdenum boat

through the same mask used for the first strip except rotated 90 degrees.

5) After evaporation, the sample was warmed to room temperature. The junction surface was checked, and a picture was taken under a high resolution optical microscope before making electric connections for low temperature measurement. A good sample was usually mounted in the cryostat right after deposition. The total time the sample was exposed to air was less than 30 minutes.

### 3.1.2. Cryostat

Shown in Fig. 3.2 is the cryostat in which the sample was mounted. It can be operated between 0.4K and 15K. The sample was attached to a copper block holder with a thin layer of Apiezon N grease. On the back of the copper holder is a calibrated germanium thermometer. A temperature controller (Lake Shore Cryotronics, Model DTC 500-SP) was used to control the sample at a temperature constant to a precision of a few millikelvin. A heater was also mounted on the copper block. To ensure a stable operating temperature, a fairly low pressure (always better than $5 \times 10^{-6}$ Torr) was maintained in the vacuum can. The part of the vacuum can surrounding the sample was placed inside the two orthogonal magnetic fields provided by two pairs of properly oriented Helmholtz coils. Outside the vacuum can and the Helmholtz coils was a lead cylinder which is submerged in liquid $^4$He. Another $\mu$ metal shield was mounted just outside the helium dewar. This shielding not only provided the desired and stable magnetic

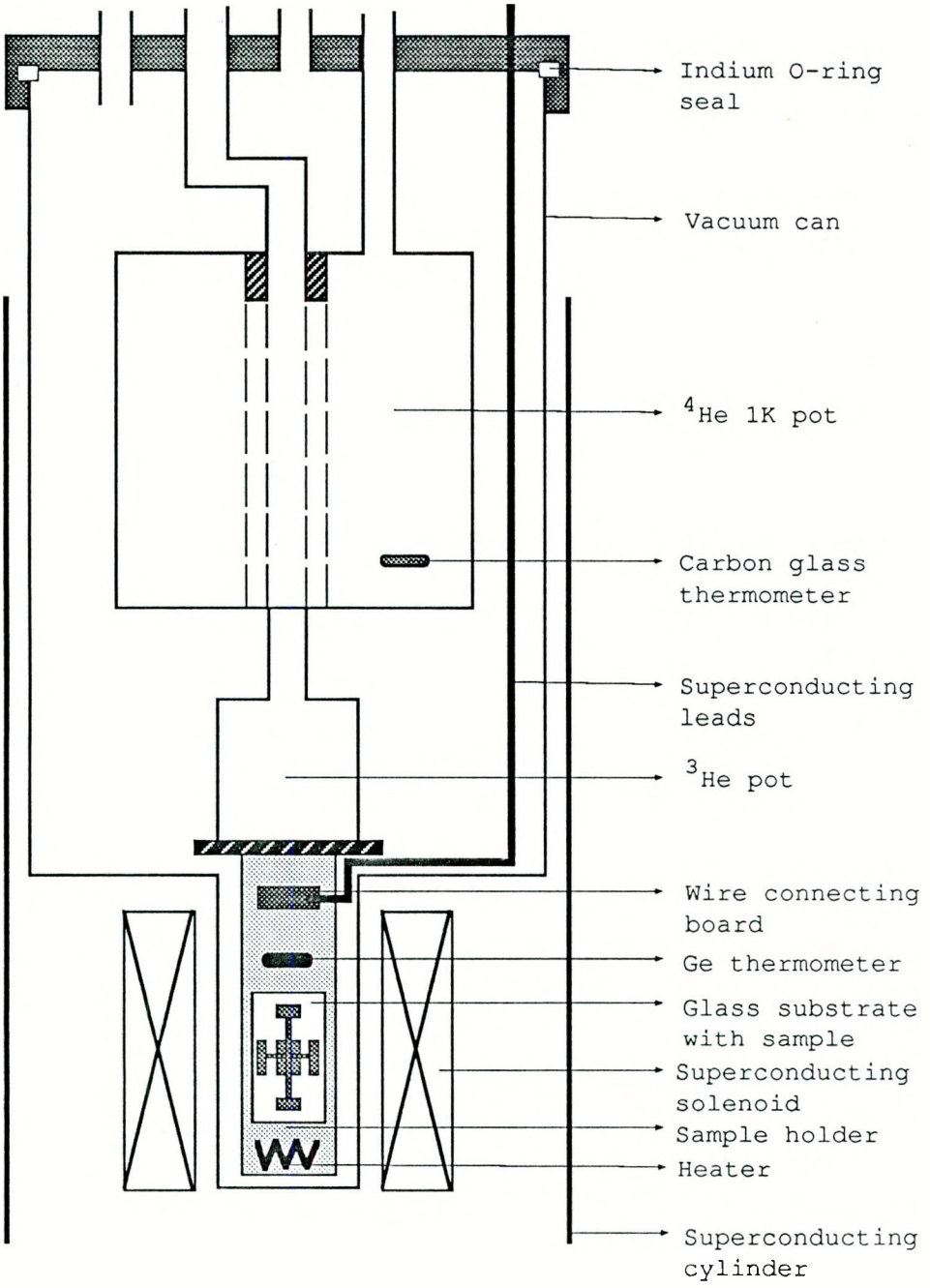


Fig. 3.2. Longitudinal section of cryostat

environment surrounding the sample, but also sufficiently screened out electric and magnetic noise from outside environment. The magnets were calibrated to 3% error range.

A temperature below 4.2K, but above 1.1K could be obtained by condensing $^4$He gas into the $^4$He 1K pot, and subsequently lowering the vapor pressure of $^4$He through a large mechanical pump. By condensing $^3$He gas into the $^3$He pot, a temperature between 1.8K and 0.4K could be achieved.

Superconducting niobium wires were used for current and voltage leads, which were extended to outside of the vacuum can. Those leads were soldered to the superconducting films with a Pb-Bi (50% a/o) eutectic alloy which has a $T_c > 8.5$K.

Shown in Fig. 3.3, is the electronic circuit designed to supply currents and to pick up the voltage signal. Two low pass LC filters were used to feed low noise transport current, $I_p$, through one of the superconducting films. The symmetric Josephson current feed-in was obtained by splitting $I_J$ through two identical 100 Ω resistors (R). The total resistance of all connecting wires (around 0.02Ω) is negligibly small compared to R. Since all electric connections inside the vacuum can are superconducting, Joule heat arising from various operations was normally less than $0.5 \times 10^{-6}$ watts so that it could be neglected.

### 3.1.3. Data acquisition and analysis

In the present experiment, the data to be taken were mostly the

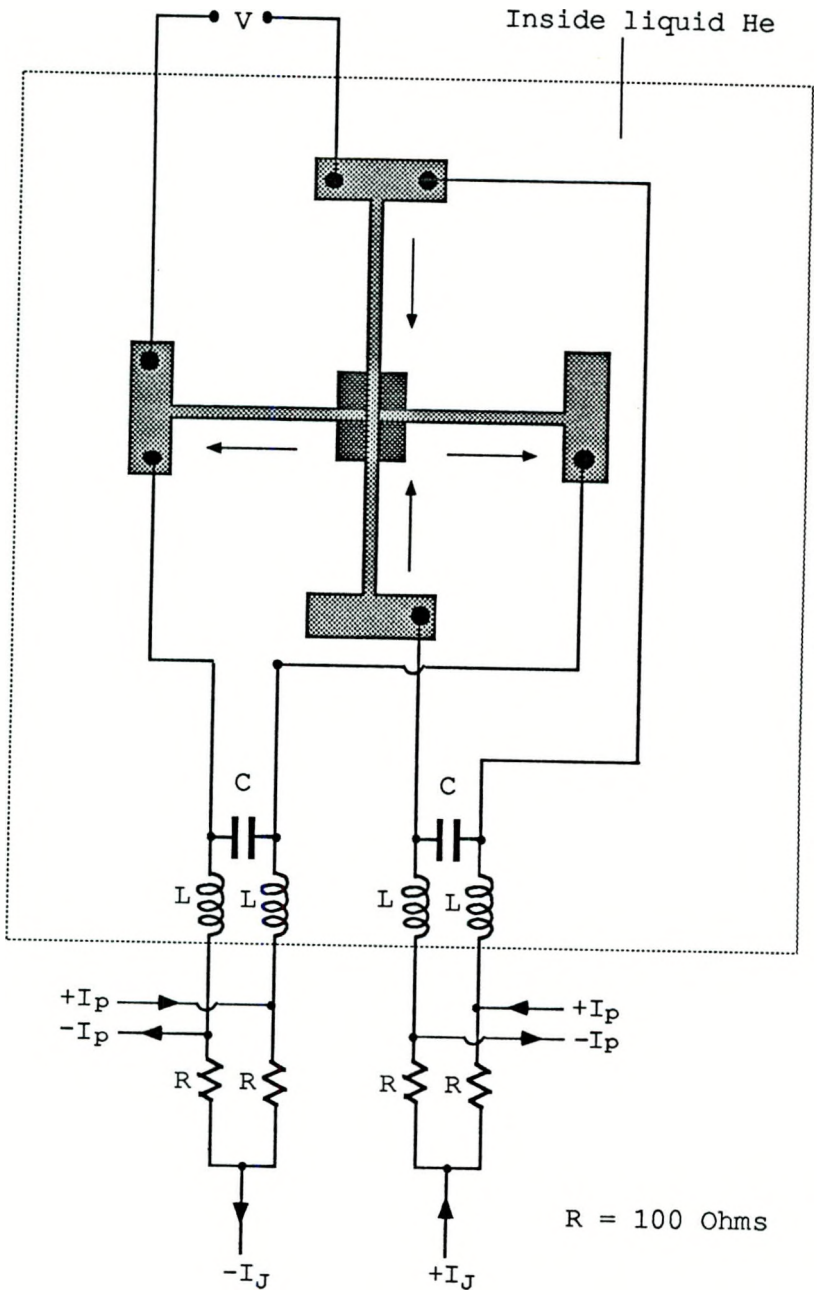


Fig. 3.3. The electronic circuit designed to supply low noise currents and pick up voltage signal

critical currents as a function of fields and temperatures. The critical currents were measured by taking junction V–I characteristics at various conditions on a X–Y recorder. A schematic of junction V–I characteristic measurement system is shown in Fig. 3.4.

All transport currents and Josephson currents were supplied by a battery operated constant current supplier (S.H.E. Model CCS). $I_p$ was read directly from the supply with an error less than 1%. For reading the $I_J$ value, a helipot was mechanically connected via a stepper motor to a potentiometer while the current itself was connected to the sample. The stepper motor was operated by a hand held control. The potentiometer voltage was displayed on the x axis of the X–Y recorder. The current calculated from that voltage differed from the actual value by less than 1.5%. The voltage output in a SNIS junction is approximately 100 $\mu$V so that a Keithley 155 microvoltmeter could be used to pick up the signal and amplified through a low pass filter ($F_c$ ~ 5 Hz). The voltage output from the filter was displayed on the y axis of the X–Y recorder. The error in reading the voltage signal is less than 2% so that this is good enough to give an accuracy about 1% of the width of the junction in determining the location of the vortex.

Temperature measurement was automated with a system made of an Apple II+ microcomputer, IEEE–488 bus, HP3495A scanner, and Keithley 181 nanovoltmeter. The resistance of the Ge thermometer was determined by reading the voltage across the thermometer and a standard resistor; then reversing the current and repeating the above

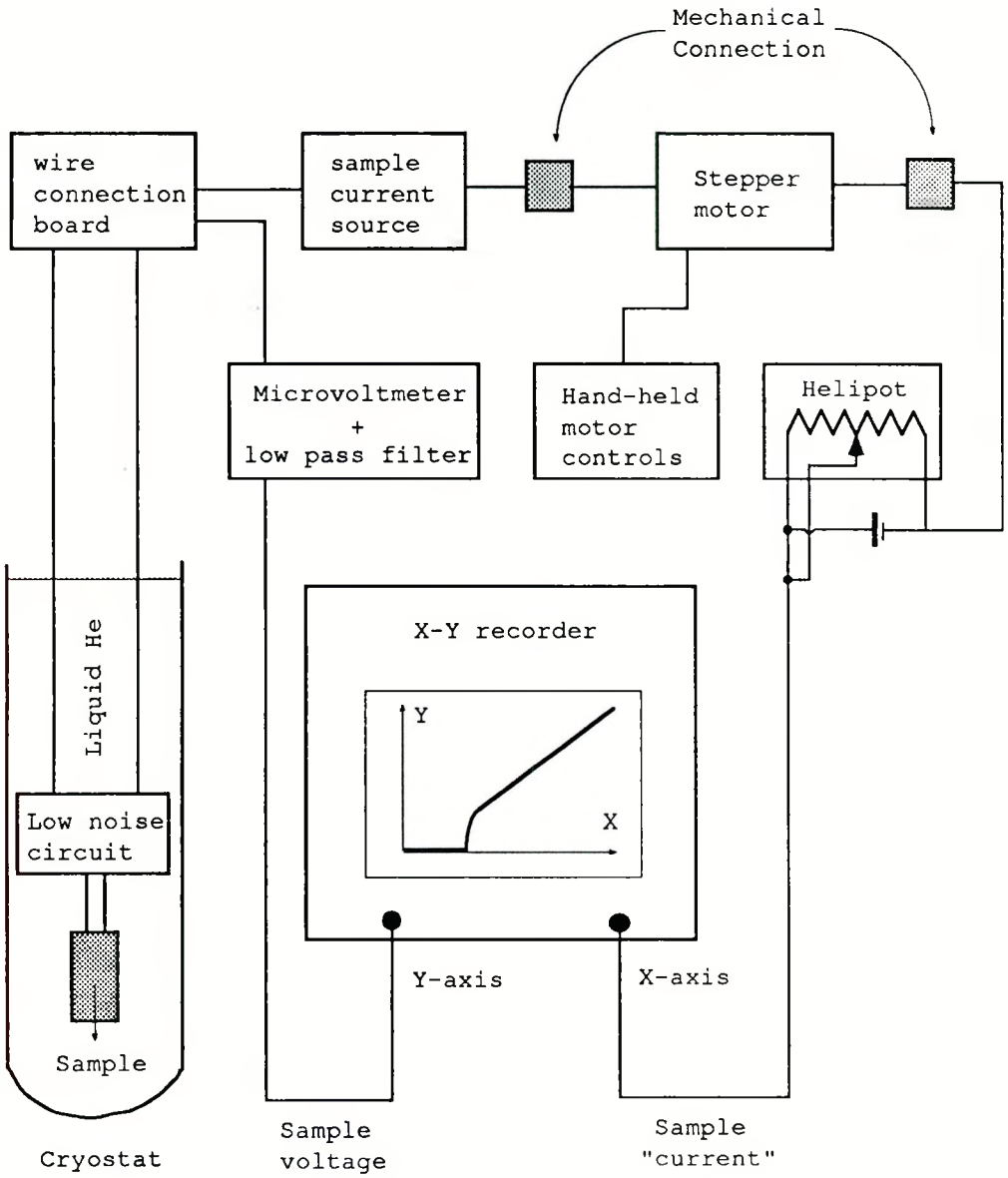


Fig. 3.4. Schematic of junction V–I characteristic measurement system

measurement to average out the thermal emf's. The temperature was calculated from the thermometer resistance to a precision of one mK.

The magnitude of the field applied through two pairs of Helmholtz coils was determined by reading the current (supplied by SCC) through the coils. This was done by measuring the voltage across a standard resistor in series with the coils. There was another way to apply a parallel field to the junction just by passing transport currents through either layer of the superconducting films. By reading the transport currents, $I_p$, we could calculate the field to less than 2% error as compared to the field generated by the coils. This will be discussed more in the next section.

For each data point of $I_c$, the following action was normally taken. After a proper field was applied and recorded, the sample temperature was measured; then a V-I characteristic was measured on the X-Y recorder by slowly increasing the Josephson current until the appearance of the Josephson voltage. This action was immediately followed by measuring the sample temperature again. Normally, the sample temperature measured before and after $I_c$ measurement differed by less than 0.002 K.

A Vax 11/780 was employed for most of the data analysis which involves curve fitting to the measured diffraction patterns so as to determine the vortex configuration in the junction. The program used in the present research is the same as that used by O. B. Hyun[16] for his Ph.D thesis work where the fitting method and quality was discussed in detail. Using that program, we calculated and compiled a

"dictionary" which gives the theoretical diffraction patterns (parallel field only) with respect to an array of single vortex positions located in the first quadrant of the junction square. Symmetry may be employed to determine the patterns in the other quadrants. However, the general fitting procedure was taken as following: One of two measured parallel field diffraction patterns $I_c$ vs $H_x$ and $I_c$ vs $H_y$ was first fitted with one single vortex having two variables, x and y coordinates as its position. In our experiments, the diffraction pattern of $I_c$ vs $H_x$ provided much better quality than that from $I_c$ vs $H_y$ so that the fitting was done to the pattern $I_c$ vs $H_x$. The one from $I_c$ vs $H_y$ then was used to verify so as to insure the fitting reliability. If one vortex fitting was not successful, two vortices with four variables (as position coordinates) were used to do the fitting, and so on. Due to the computation capability and the experimental errors, no fitting was tried for more than four vortices.

## 3.2. Basic Properties of the SNIS Josephson Junctions

In this section we will present basic properties of the SNIS Josephson junctions used in our experiments. The V-I characteristics of this family will be discussed qualitatively. Some important parameters of the junction will be given here, in addition to the diffraction patterns of the junctions and temperature dependence of the critical currents. Most discussion in this section will have an

emphasis on the qualitative understanding the physics involved, rather than on the quantitative fitting to the data.

### 3.2.1. Voltage current characteristics

The voltage-current, V-I, curves of our junctions are typical of an SNIS Josephson junction[24] as shown in Fig. 3.5. The voltage is zero out to a value close to the critical current, $I_c$, and rises rapidly to the normal ohmic behavior at high currents. A reversible characteristic behavior shown in Fig. 3.5a was normally observed at temperature higher than 3.6K. Below 3.6K, the hysteresis gradually increases and shows the behavior of Fig. 3.5b at 0.53K, where the "normal" metal actually becomes superconducting. The hysteresis of V-I curve can be estimated by the hysteresis parameter $\alpha = I_{SW}/I_c$, where $I_c$ is the critical current and $I_{SW}$ is the value of the bias current at which the junction switches from the voltage state back to the Josephson tunneling state. For sample SNIS#9, at temperatures higher than 3.6K, the V-I curve was found reversible within the limit of our X-Y recorder, so that $\alpha = 1$. Below 3.6K, a rather small amount of hysteresis can be found on the V-I curves which gradually increases as the temperature decreases. At 2.0K, it was found that $I_c = 0.87$mA, and $I_{SW} = 0.83$mA so that $\alpha = 0.95$. Below 1.05K, very large hysteresis appears, as shown in Fig. 3.5b, because Al becomes superconducting at $T_c = 1.19$K. For a temperature of 0.53K, it was found that $I_c = 3.18$mA and $I_{SW} = 1.24$mA so $\alpha = 0.39$.

This overall behavior can be qualitatively described by

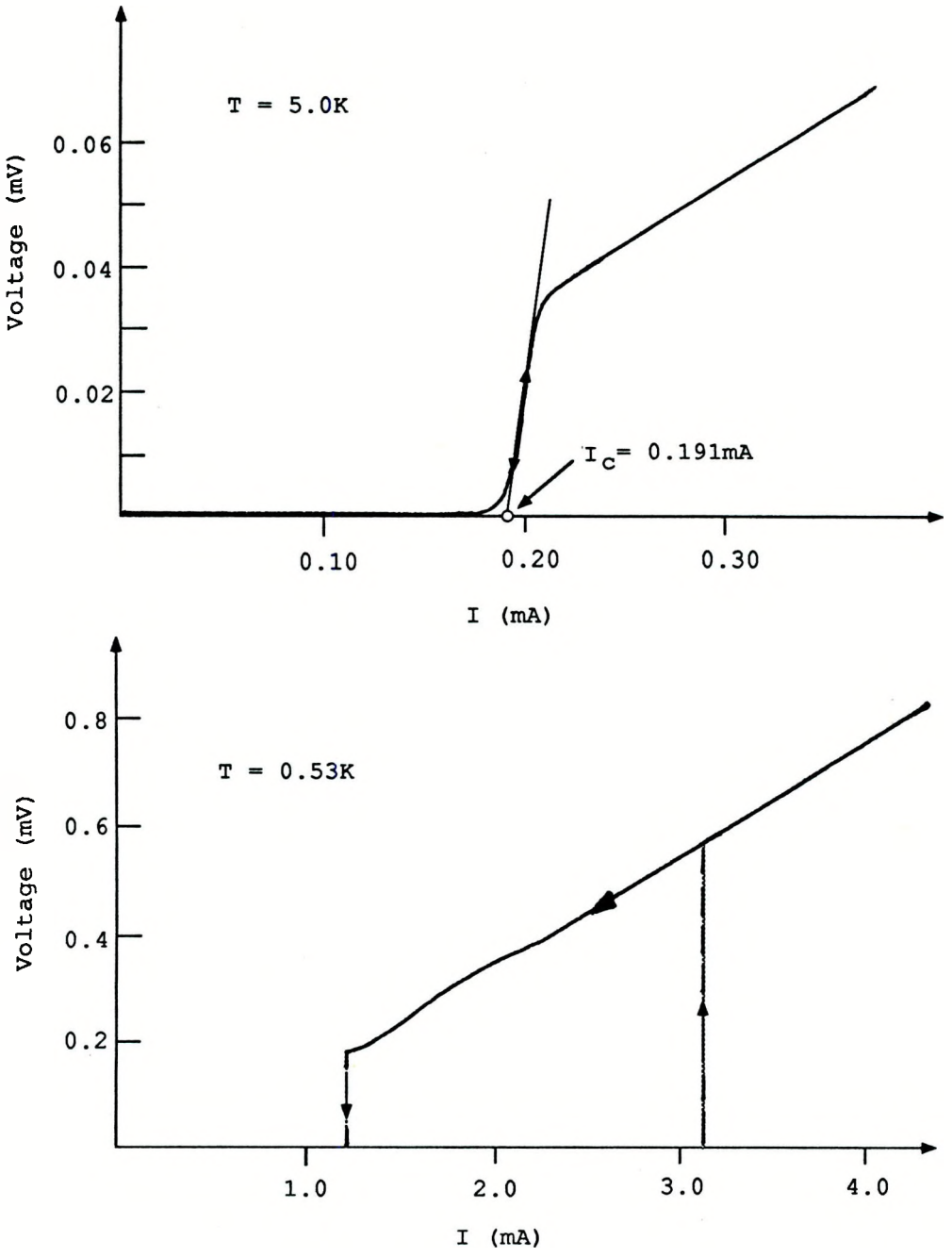


Fig. 3.5. V-I characteristics of sample SNIS#9 measured at (a) T=5.0K, reversible, and (b) T=0.53K, hysteretic

Resistively Shunted Junction (RSJ) model.[24,25] Within the framework of the RSJ model, the detailed shape of the V–I characteristic is determined by the magnitude[26,27] of a dimensionless parameter $\beta_c$ which is given by

$$\beta_c = 2eR^2I_cC/\hbar \ , \tag{3.1}$$

where R is the junction resistance and C is the capacitance.

Generally, the small SNS junctions are in the small capacitance limit, or $\beta_c \approx 0$, which corresponds to the reversible V–I curve. Ideal SIS thin-film junctions are usually in the large capacitance limit, or $\beta_c \approx \infty$, which usually yields hysteretic behavior on V–I curves. Using the RSJ model, four Josephson junction parameters are essential: (1) the critical current $I_c$, (2) the normal state resistance R, (3) the capacitance C, and (4) the maximum Josephson current density $J_o$ (or $\sin\phi$–amplitude). The parameters, $I_c$ and R, are readily determined from the V–I curve. Unlike SNS Josephson junctions having low resistance, and a negligibly small capacitance, the SNIS junction usually has a capacitance which should be seriously considered in order to correctly do the V–I curve fitting. To measure the capacitance, C, essentially two methods exist: (1) a measurement of the geometrical resonance frequency from the position of the cavity induced step[28] in the V–I curve, and (2) a determination of the McCumber parameter[27] $\beta$ ( $\propto$ C ) using measured values of the hysteresis parameter[27] $\alpha$. Both methods have drawbacks; the former requires knowledge of the temperature– and frequency–dependent penetration depth, and the latter depends on the hysteresis parameter $\alpha$, and value of $J_o$ which are normally determined

from the microwave measurements. It is generally argued[26] that the V-I curve itself does not provide such information. For lack of the actual value of capacitance, it is not possible to perform the theoretical fitting to the V-I curve in the present work.

Whether the V-I curve of a Josephson junction shows hysteresis or not depends on the magnitude of $\beta_c$. For an SNIS junction, $\beta_c$ is finite. Values of $\beta_c$ less than 0.5 are usually believed to give reversible V-I characteristics.[24, 26-29] Here, we make a rough estimation of the order of magnitude of $\beta_c$ for sample SNIS#9 near $T_c$ so as to be used for comparing with the experimental results. By assuming the dielectric nature of the oxide film contributes most to the capacitor of the SNIS junction, the capacitance C for a $55x55\mu m^2$ junction at temperature near $T_c$ is on the order of 1pF to 100pF, estimated from the work by Soerensen, Mygind, and Pederson[29]. The resistance R is around $0.2\Omega$, and $I_c$ is of the order of $100\mu A$ near $T_c$. From Eq. 3.1, $\beta_c$ is calculated to be of the order of $10^{-2}$ to 1 for sample SNIS#9, which results in reversible V-I curves near $T_c$.

The critical current $I_c$ increases fast as the temperature decreases. Below 3.0K, $I_c$ for sample SNIS#9 is on the order of 1mA, which is about one order of magnitude higher than the value of $I_c$ at 6.0K. This makes the value of $\beta_c$ increase to the range of 0.1 to 10, which could result in hysteresis in the V-I curves.

The critical current, $I_c$, is defined to be the extrapolation of the steepest slope portion of the curve to the zero voltage line as shown in Fig. 3.5a. The rounding near V=0 is typical of these SNIS

junctions.[24] This rounding was usually found less severe in the SNS Josephson junction,[16] where the very low resistance and capacitance of the junction give much less sensitivity to noise and thermal fluctuation, for $< V > \propto RC$. The rounding makes it more difficult to get a correct value of $I_c$, especially when $I_c$ is less than 10$\mu$A. The $I_c$ measured for the diffraction pattern, however, is normally around 150$\mu$A so that the error in determining $I_c$ is usually less than 3% $I_c$, as long as $I_c$ is larger than 50$\mu$A.

Listed in Table 3.1 are some important parameters of our SNIS junctions. The thickness of all films was measured by quite accurate Tencor thickness profiler. The transition temperature $T_c$ for each film was obtained directly from four probe resistance measurement. They usually vary less than 0.05 degree from junction to junction. The zero temperature London penetration depth, $\lambda_L^{Pb}(0)$,[34] $\lambda_L^{PbBi}(0)$,[35] was obtained from earlier work, and verified via $H_o$ measured from all our diffraction patterns with accuracy of 5%. The resistivity of the normal metal Al in sample SNIS#3 was measured on a co-evaporated Al film by using a four probe method. The Fermi velocity $v_{Fn}$ was determined from equation $v_{Fn}=(k_B^2 S)/(12\pi\hbar\gamma)$[36], where S is the area of the Fermi surface and $\gamma$ is the electronic specific heat parameter. If we let the subscript "o" signify the free electron model, then

$$v_{Fn}/v_{Fno} = (S/S_o)\cdot(\gamma_o/\gamma)$$

The relevant numerical values are $v_{Fno} = 2.02\times10^8$ cm/s,[37] $\gamma_o = 0.912\times10^{-3}$ $Jmol^{-1}K^{-2}$,[38] $\gamma = 1.35\times10^{-3}$ $Jmol^{-1}K^{-2}$,[38] $S = 0.99S_o$,[39] from which we find the Fermi velocity of Al, $v_{Fn}$, equal to $1.35\times10^8$ cm/s. Then, the mean

Table 3.1. Parameters for Junctions SNIS#3, and SNIS#9

| Sample ID | $d_n$ (nm) | $d_{Pb}$ (nm) | $d_{PbBi}$ (nm) | $T_c$(Pb) (K) | $T_c$(PbBi) (K) |
|---|---|---|---|---|---|
| SNIS#3 | 40 | 410 | 650 | 7.29 | 7.33 |
| SNIS#9 | 310 | 380 | 560 | 7.28 | 7.35 |

| Sample ID | $\rho_n$ ($\mu\Omega$-cm) | $v_{Fn}$ (cm/s) | $l_n$ (nm) | $K_n^{-1}$ (nm) | $K_n^{-1}$ (nm) |
|---|---|---|---|---|---|
| Temp. | 4.2K | ——— | 4.2K | T | 4.2K |
| SNIS #3 | 0.26 | $1.35 \times 10^8$ | 1000 | $230/T^{1/2}$ | 110 |

| Sample ID | $\lambda_L^{Pb}(0)$ (nm) | $\lambda_L^{PbBi}(0)$ (nm) | $\lambda_L^{Pb}(4.2K)$ (nm) | $\lambda_L^{PbBi}(4.2K)$ (nm) |
|---|---|---|---|---|
| SNIS #3,#9 | 39 | 104 | 41 | 110 |

free path for Al can be calculated from $\rho_n l_n = v_{Fn}(m_e/ne^2) = 264$ $(\mu\Omega\cdot cm)\cdot\text{Å}$, where $n_{Al} = 18.1x10^{22}/cm^3$ , and the decay length for Al layer can be obtained from $K_n^{-1} = (\hbar v_{Fn} l_n/6\pi k_B T)^{1/2}$, as shown in Table 3.1.

3.2.2. Temperature dependence of $I_c$

Shown in Fig. 3.6, are plots of $I_c$ vs T, for two different samples SNIS#3 and SNIS#9. The major difference between them, as illustrated in Table 3.1, is the thickness of the normal metal Al film, where 40nm for sample SNIS#3 and 310nm for SNIS#9.

In contrast to SNS Josephson junctions, relatively little theoretical work has been done on SNIS Josephson junction systems. Rowell,[30] Smith,[30] Blackburn,[24] and J. P. Romagnan[31] et at. suggested a treatment of SNIS junctions similar to that of SIS junctions. For convenience of description, we arrange SNIS junction from left to right as $S^{left}$–Normal layer–Insulator–$S^{right}$, as shown in Fig. 3.7a. The amplitude of Josephson current was approximately treated to be proportional to the product of the order parameters immediately on either side of the insulating barrier. The order parameter near I–N boundary in normal metal could be provided by the proximity effect from the N–S interface. Within the superconducting layer, the linear Ginzburg–Landau equation is used to describe the behavior of the order parameter. Within the normal metal, Werthamer's solution[32] is used with the application of the boundary condition suggested by de Gennes[33]. Based on such an argument, we will give a qualitative explanation of the measured temperature dependance of $I_c$ for our SNIS

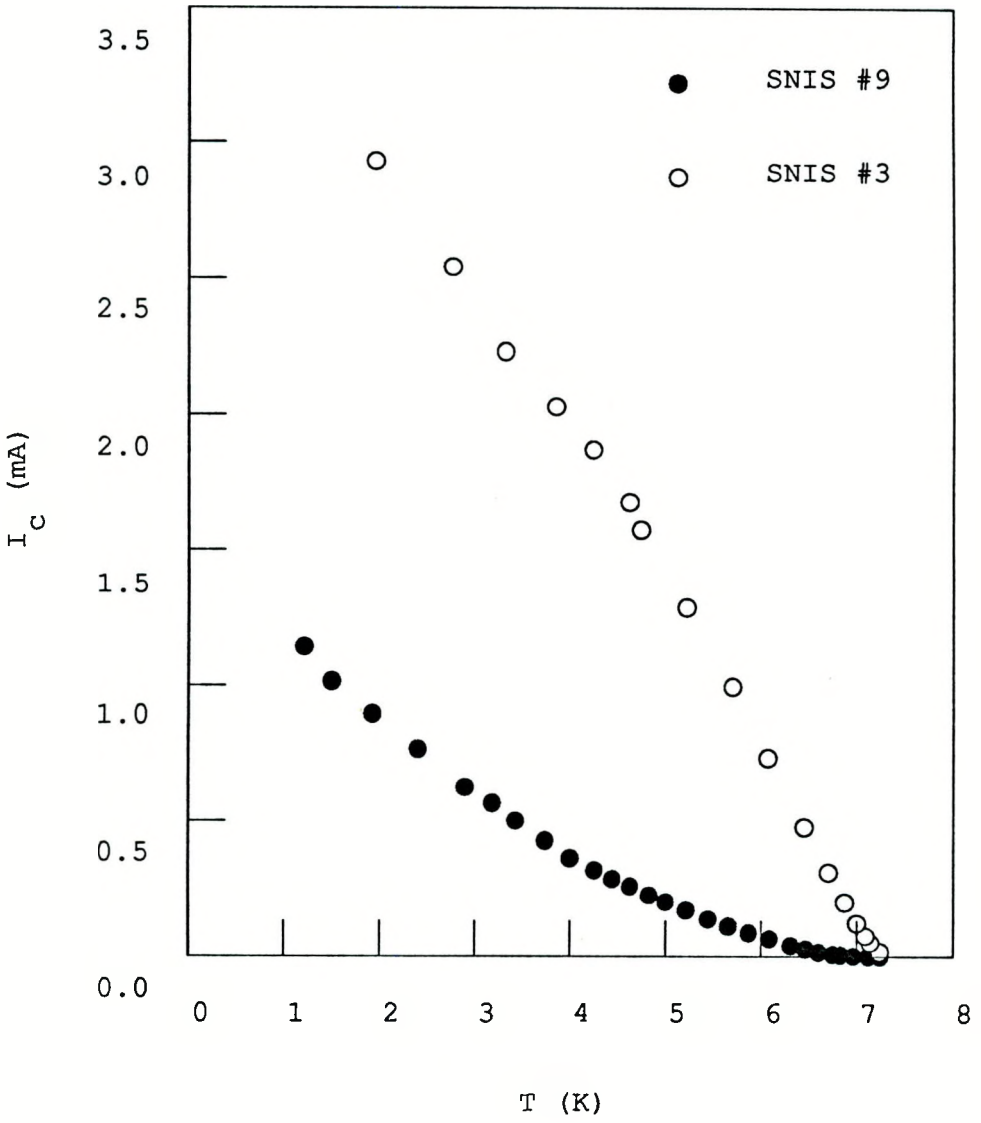


Fig. 3.6. Plots of $I_c$ vs T for sample SNIS#3, and SNIS#9

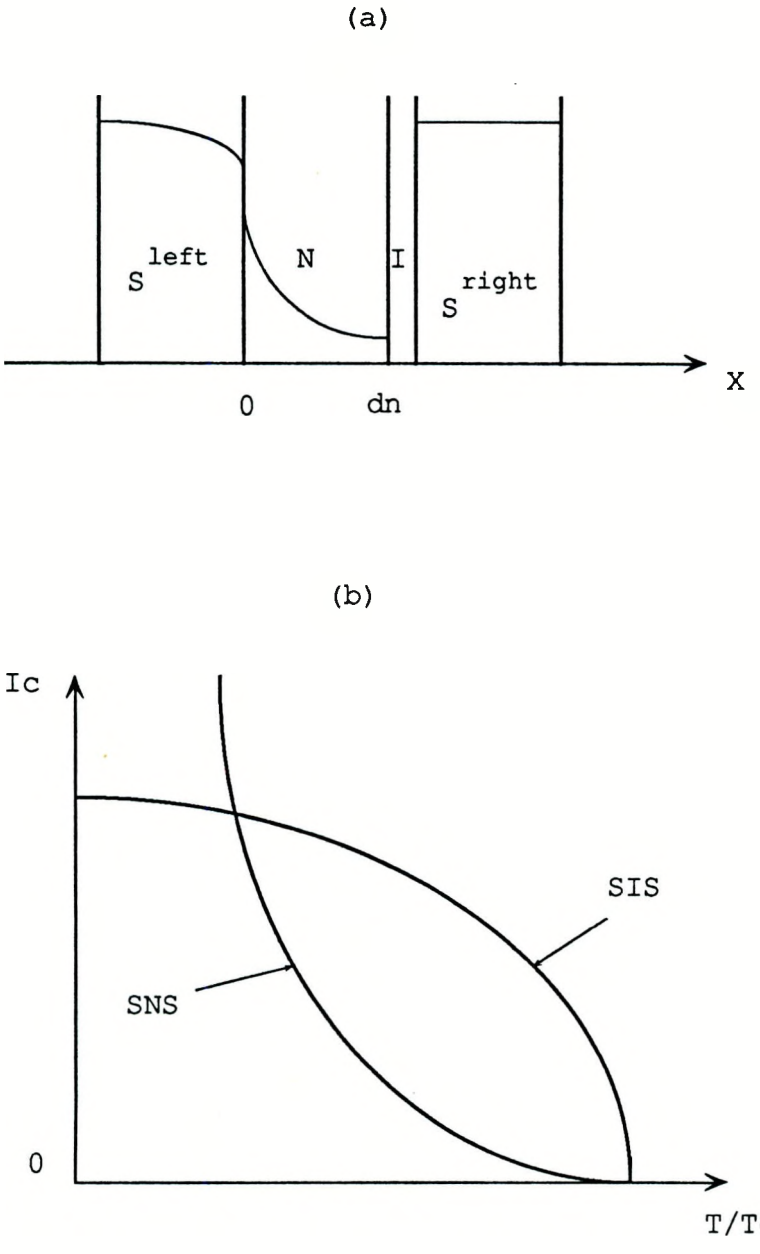


Fig. 3.7. (a) Qualitative sketch of the order parameter behavior for a SNIS junction. (b) Qualitative sketch of $I_c$ as a function of temperature for ideal SIS junction and SNS junction

junctions.

$I_c$ is proportional to the product of two condensation amplitudes on both sides of insulator, as

$$I_c = F_n(d_n) \cdot F_{BCS}^{right} , \tag{3.2}$$

where $F_{BCS}^{right}$ is that from the right side superconducting film, and $F_n(d_n)$ is that near the N-I boundary due to the proximity effect, which is given as[36]

$$F_n(d_n) = \mathrm{csch}(k_n d_n) \cdot (C/k_n \xi_{n,GL}) \cdot F_{BCS}^{left} . \tag{3.3}$$

It is worth noting here that BCS stands for the value calculated from BCS theory from the measured $T_c$; C is a temperature independent parameter; $\xi_{n,GL}$ is the Ginzburg-Landau coherence length for the normal metal. Eq. 3.3 is simply derived from the proximity effect plus the de Gennes boundary condition.[33,36] The theory introduced here is somewhat empirical as stated by Greenspoon and Smith[36]. It is not adequate to fit $I_c$ vs T curves over the entire range of temperature. But a fit to the high temperature part is possible. The overall shape of the $I_c$ vs T curve depends on the thickness of the normal layer, which is reflected by the curvature of the entire $I_c$ vs T curve. It is worthwhile to give a more discussion of two of important features of this new type of junctions. First, we will present the theoretical fitting to the data in the high temperature regime, and then discuss the overall shape of $I_c$ vs T curve in the entire temperature range.

*(1) High temperature regime (T near $T_c$)*

The temperature dependence of $I_c$ at high temperatures for a SNIS

junction has been studied by Greenspoon and Smith[36]. Considering the fact that $T_c$ for Pb and PbBi films are very close, we could approximately treat our junction as if the two superconducting layer are identical. Near $T_c$, $F_{BCS}(T)$ and $\xi_{n,GL}^{-1}(T)$ vary with temperature as $(1-T/T_c)^{1/2}$. Since our superconducting film is very thick so that the transition temperature of the N-S system, $T_{cs}$, will be close to the transition temperature of S. Near $T_{cs}$ the $T^{1/2}$ dependance of $K_n(T)$ (see Table 3.1) will be small with respect to $F_{BCS}(T)$ and $\xi_{n,GL}^{-1}(T)$. Then, to a good approximation, we have from Eq. 3.3,

$$F_n(d_n) \propto (1-T/T_{cs}) \ ,$$

and from Eq. 3.2

$$I_c \propto (1-T/T_{cs})^{3/2} \ .$$

This relation is different from that of either an ordinary SIS Josephson junction, $I_c \propto (1-T/T_{cs})$, or an SNS Josephson junction with a thick normal layer, $I_c \propto [1-(T/T_{cs})^2]$.

In Fig. 3.8, we have plot the experimental values of $I_c^{2/3}$ vs T for junction SNIS#3 and SNIS#9. Least-squares fit linear regression lines have been drawn for junction SNIS#3 based on results above 6.2K, and for junction SNIS#9 above 5K. Rather good agreement was found.

*(2) Curvature of $I_c$ vs T for SNIS junctions*

The temperature dependence of $I_c$ for a SNIS junction is strikingly different from either that of an ordinary SIS junction, or that of SNS junction. Shown in Fig. 3.7b, is a qualitative sketch of $I_c$ as a function of temperature for ideal SIS junctions and SNS

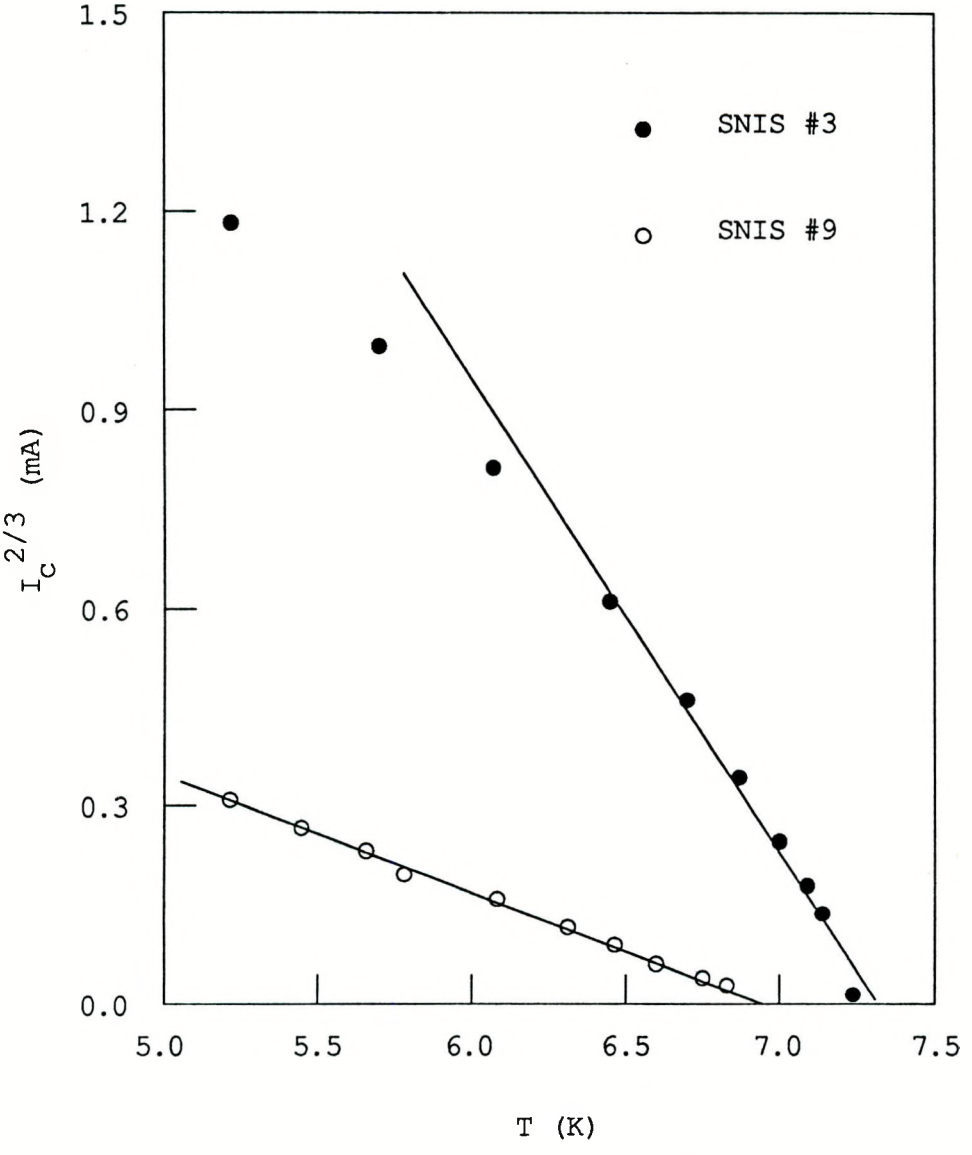


Fig. 3.8. $I_c$ vs T curves for sample SNIS#3 and SNIS#9 at high temperature. The least-squares fit linear regression lines have been drawn for SNIS#3 based on the results above 6.2K, for SNIS#9 based on the results above 5K

junctions. For SIS junctions, $I_c$ is essentially reflecting the behavior of the condensation amplitudes in the superconducting films which is normally saturated at low temperature. For ordinary SNS junctions, $I_c$ increase rapidly with decreasing temperature, caused by the exponential dependance on $K_n^{-1}$, which is proportional to $T^{-1/2}$. At temperatures away from $T_c$, the curvature of $I_c$ vs T is convex for a SIS junction, but concave for a SNS junction. As for a SNIS junction, if the thickness of the normal layer is extremely small, i.e., $K_n d_n \ll 1$, we should have approached to the SIS limit. In the opposite sense, i.e., extremely thick normal layer, $k_n d_n \gg 1$, it is not difficult to see that the temperature dependance of $I_c$, at low temperature $T < 0.5T_c$, is controlled by the condensation amplitude at the normal metal-insulator interface, $F_n(d_n)$, since the $F_{BCS}$ for superconducting films is near constant. Thus, according to Eq. 3.2, we have

$$I_c(T) \propto F_n(-d_n) \propto \{T^{1/2}[\sinh K_n(T)d_n]\}^{-1} . \qquad (3.4)$$

Furthermore, when $K_n d_n \gg 1$, $\sinh(K_n d_n) \approx (1/2)\exp(K_n d_n)$, such that $I_c(T) \propto [(T)^{1/2}\exp(k_n d_n)]^{-1}$, It should be noted immediately that the behavior of $I_c$ is identical with that which would be followed if the junction were considered to be an SNS point contact,[40] whose curvature of $I_c$ vs T is concave. Therefore, $I_c$ vs T for SNIS junctions should change in curvature from convex to concave, as the thickness of the normal layer decreases.

A. Gilabert et al.[41] have calculated the theoretical curves, $I_c/I_o(T=0)$ vs $t=T/T_c$, for their Nb-$Nb_xO_y$-Al/Pb junctions with different

values of tunneling parameter $\Gamma_n$ which is inversely proportional to $d_n$. Let $\Delta_s$ be the energy gap of Pb, tunneling parameter $\Gamma_n = \hbar v_{Fn}/(4\rho_n B d_n)$, while B is a function of $l_n$ and $d_n$. Their results are shown as solid lines in Fig. 3.9. Also shown in the Figure are our experimental data for junction SNIS#3 and SNIS#9, where $I_o(0)$ was substituted by $I_c(T=1.2K)$, since $T_c$ is 1.19K for aluminum. Even though the direct comparison of our data to their calculation is not theoretically rigorous, it is clearly meaningful to compare the qualitative feature in the sense of curvature.

After comparing the value, $d_n$, to decay length, $K_n$, for our junctions, it is possible to see a reasonable agreement between our data and their calculation, as shown in Fig. 3.9. $d_n$ for SNIS#9 is 310nm, which is larger than $K_n^{-1}$ at entire operating temperatures. This means that $K_n d_n > 2$, so that the junction behaves more like an SNS point contact, which gives concave curvature in $I_c$ vs T. For SNIS#3, $d_n$ is only 40nm, while $K_n^{-1}$ is about 100nm at temperature below 6K. Thus, low value of $k_n d_n$ (less than 0.4) should makes the junction more like the SIS type, which has a convex curvature.

### 3.2.3. External field dependence of $I_c$ and quality of insulating film

Most of the difficult aspects of preparing a high quality SNIS Josephson junction arise from the need to prepare a uniform insulating $Al_xO_y$ barrier free of microshorts, or pinholes. It was found much easier to control the growth of the oxide if the Al pad had a larger area with a small pad just covering the junction in the middle.

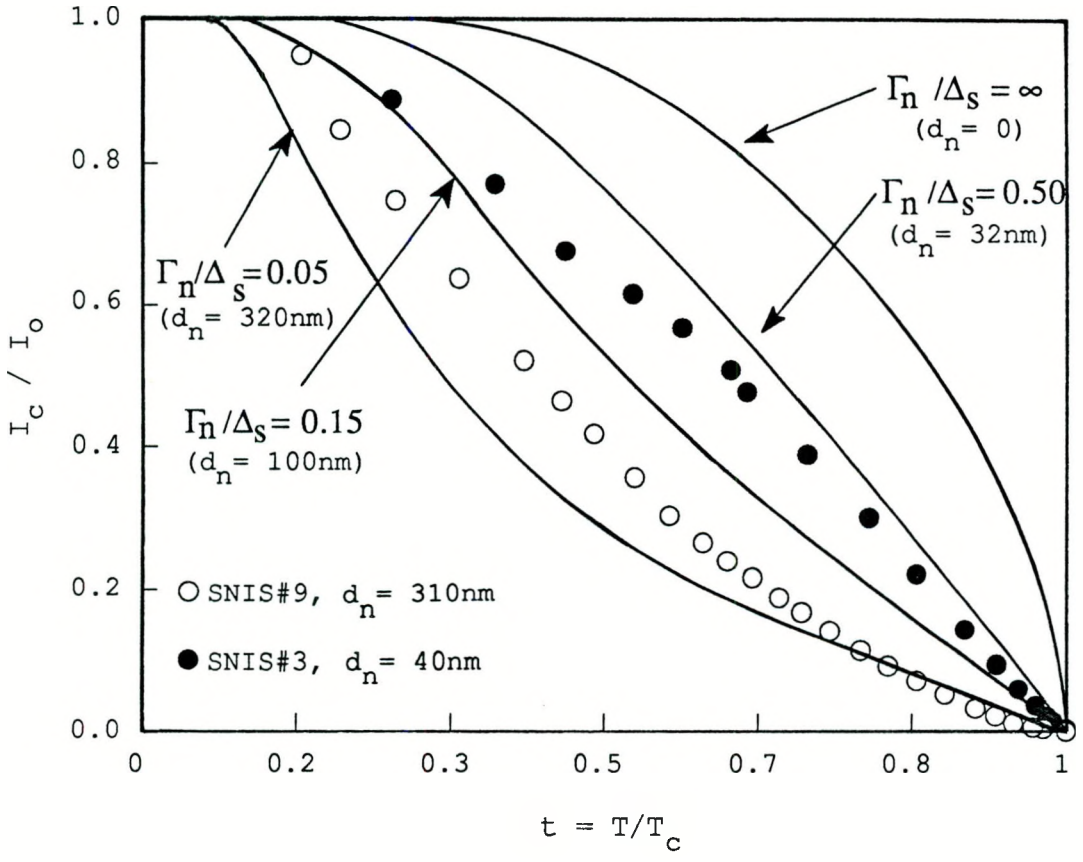


Fig. 3.9. The temperature dependence of normalized $I_c$ for SNIS junctions with different Al thickness. The experimental points are for our PbBi-$Al_xO_y$-Al-Pb junctions, where $I_o$=$I_c$(T=1.2K); the theoretical curves are for the Nb-$Nb_xO_y$-Al-Pb junctions, with $I_o$=$I_c$(T=0)

For convenience of discussion, we choose a coordinate system shown in Fig. 3.10. The bottom Pb layer is along the y-direction, while the PbBi layer is along the x-direction. The external fields generated by two sets of Helmholtz pairs give the parallel magnetic field along the y-direction, with the perpendicular field along the z-direction.

The traditional method to check the quality of the oxide barrier is to measure the Fraunhofer pattern, where the regular periodicity of the Fraunhofer oscillations in the presence of an externally applied parallel magnetic field indicates a uniform barrier without microshorts. Shown in Fig. 3.11a, are the experimental data, $I_c/I_o$ vs $H_y/H_o$, for sample SNIS#3 measured at 6.65K, which was fitted to an ideal Fraunhofer pattern of

$$I_c/I_o = |\sin(\theta)/\theta| \ , \qquad (3.5)$$

where $\theta = \pi H_y/H_o$ with $H_o = 1.094$ gauss, the period of oscillations of junction SNIS#3 at 6.65K. Such a good fitting was obtained even at temperatures down to 6.0K, where $\lambda_J = 0.95W$. For this value of $\lambda_J$, the Josephson current density is uniform across the junction to about 2% at zero field.

With the magnetic field perpendicular to the junction surface, the normalized critical currents as a function of $H_z/H_o$ for sample SNIS#3 are shown as solid circles in Fig. 3.11b. A good theoretical fitting was done by using the formula

$$I_c/I_o = | \ Si(\alpha)/\alpha \ | \ ,$$

where $\alpha = -2\pi H_z/H_o$ and $H_o = 1.094$ gauss at 6.5K. The theoretical

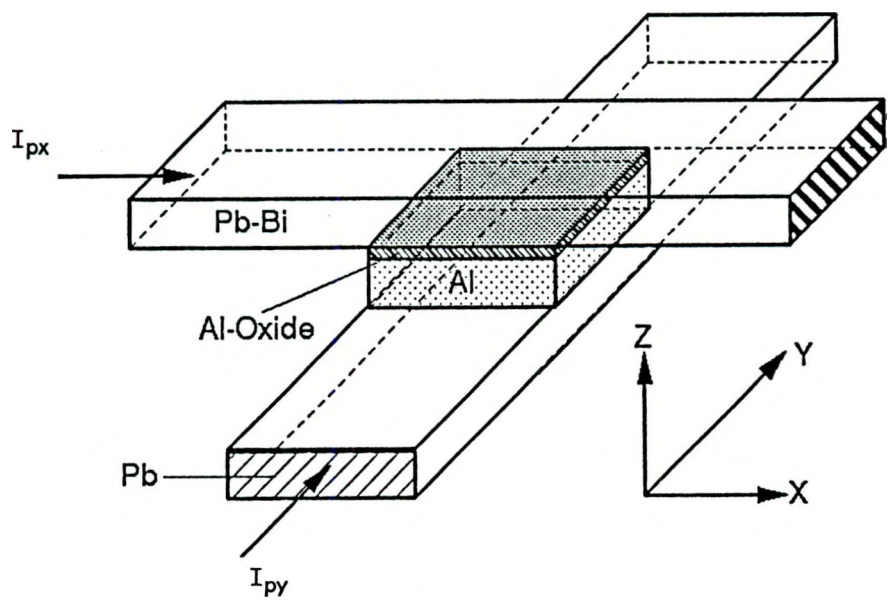


Fig. 3.10. Sketch of the SNIS junction geometry and the coordinate system chosen for the convenience of discussion

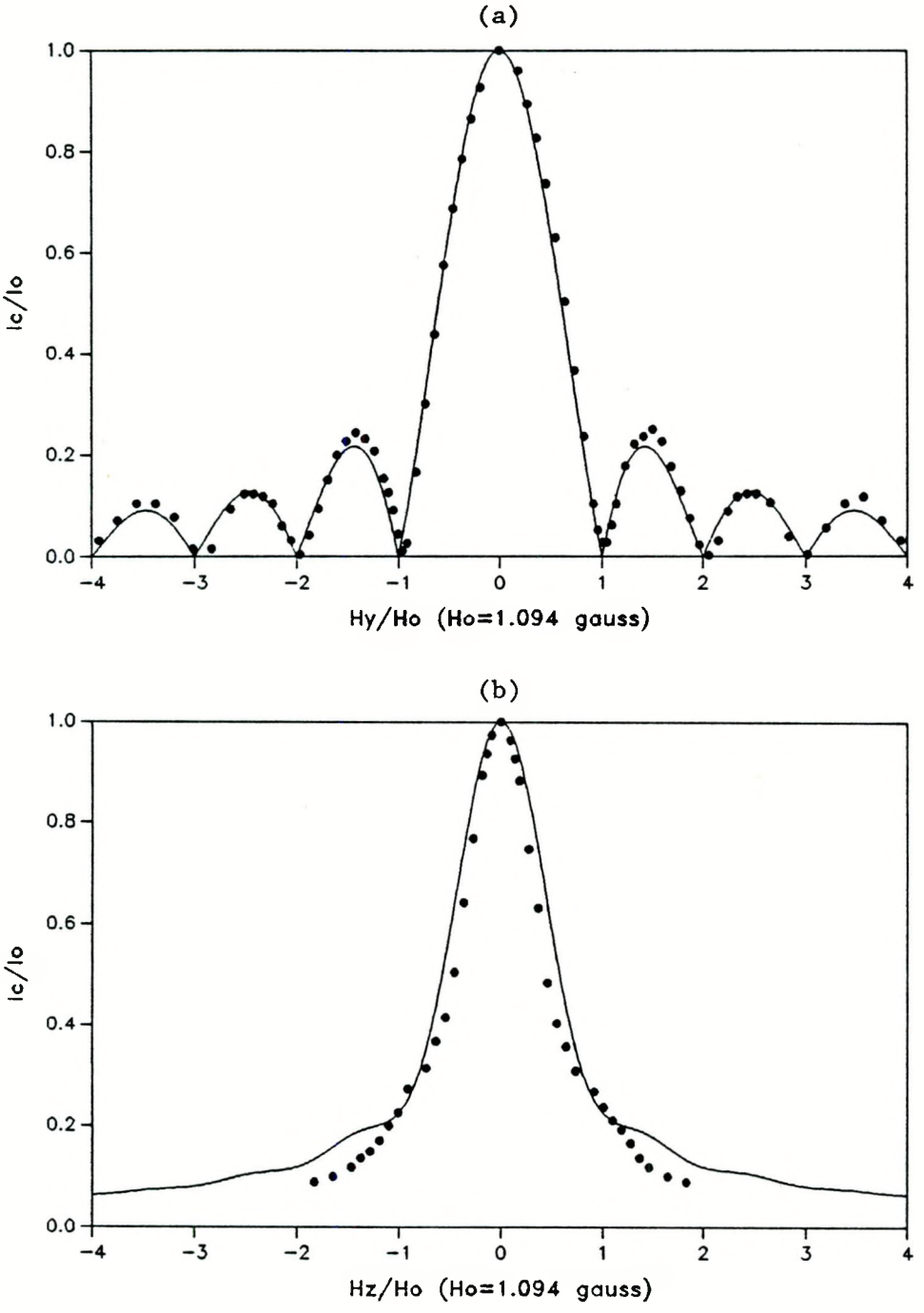


Fig. 3.11. The external field dependence of $I_c/I_o$ for sample SNIS#3, where $I_o$ = 0.63mA, $H_o$ = 1.094 gauss. The solid circles are experimental data taken at 6.65K; the lines are theoretical patterns. (a): $I_c/I_o$ vs $H_y/H_o$; (b): $I_c/I_o$ vs $H_z/H_o$

fitting curve is a little higher than that corresponding experimental data, which was also observed by S. Miller[14], and O. B. Hyun[16] in their SNS junctions. It should be noted that the theoretical curve is calculated from the approximate solution where only the lowest order terms are kept for screening current density and induced phase.[14,16]

As a matter of fact, the rather good external field dependence of $I_c$'s proves a uniform Josephson current density tunneling through the junction, which is the result of the good quality junction barrier. This means that the oxide barrier is rather uniform.

An alternative way to get a Fraunhofer pattern for the junction is to use the field in the junction generated by the transport current in the Pb or PbBi strip.[42] According to the calculation made by Huebener, Kampwirth, and Clem,[43] the transport current passing through the thin film strip of thickness $d_s$ and width W produces parallel magnetic field of

$$H_{/}\ (\text{surface}) = 0.8I_p/(d_s + W\ )\ (\text{gauss-cm/Amp})\ , \qquad (3.6)$$

By measuring $I_c$ as a function of transport current $I_p$, a diffraction pattern can be obtained. Shown in Fig. 3.12, are two Fraunhofer patterns of sample SNIS#9 measured at 5.0K by applying the transport current, $I_{py}$, in the bottom Pb thin film lying in the y-direction. The magnetic fields, $H_x$, generated by $I_{py}$, are along the x-direction. In Fig. 3. 12a, $I_c/I_o$ was plotted as a function of $I_{py}$; in Fig. 3.12b, $I_c/I_o$ was plotted as a function of $H_x/H_o$, where $H_o$ = 0.81 gauss for the sample SNIS#9 at 5.0K, and $H_x$ was calculated via Eq. 3.6 from $I_{py}$, with two constants $d_s$ = 410n and W = 55$\mu$m.

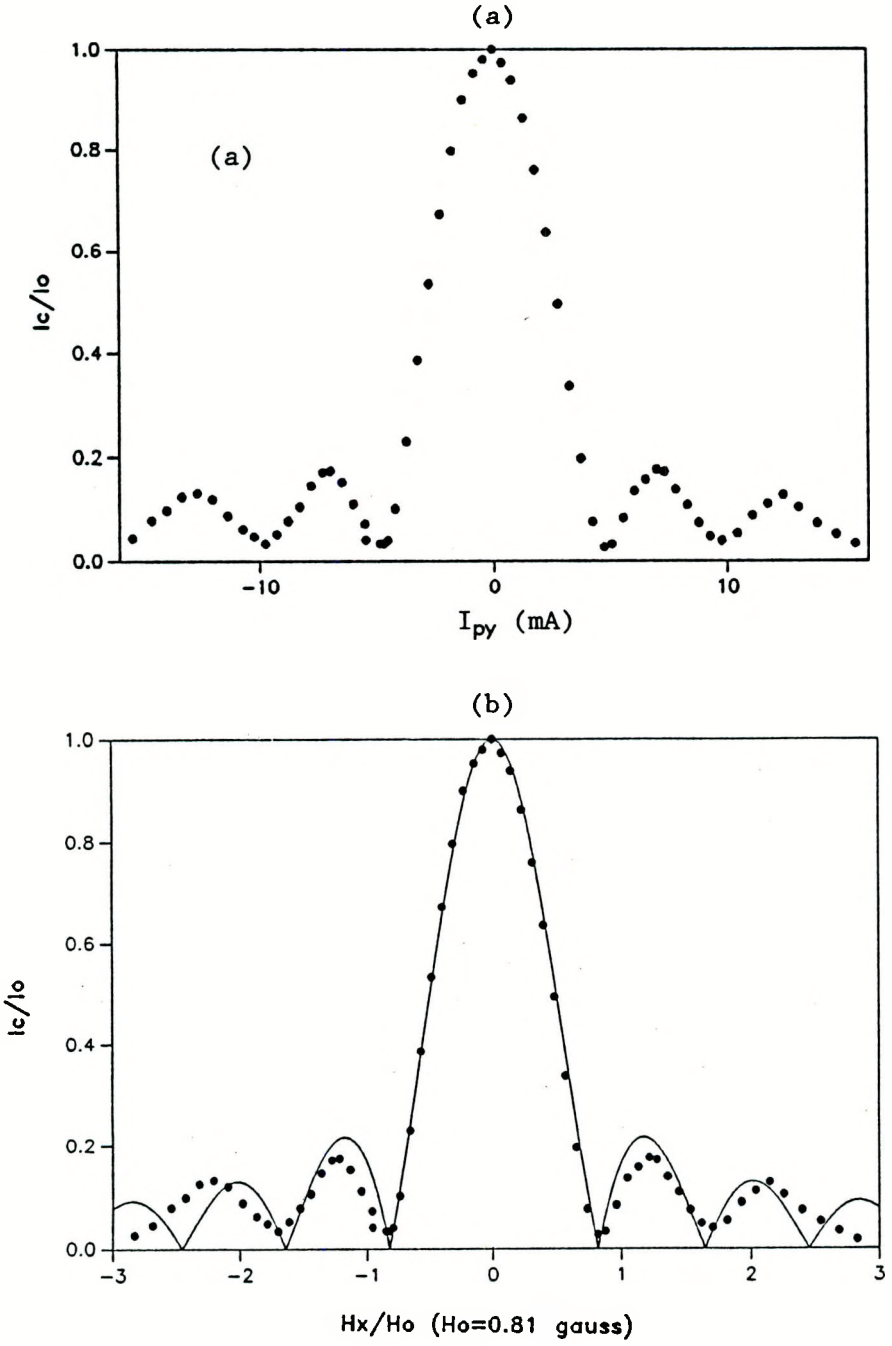


Fig. 3.11. The Fraunhofer patterns measured by applying transport currents, $I_{py}$, in the Pb strip. (a) $I_c/I_o$ is plotted as a function of $I_{py}$; (b) $I_c/I_o$ is plotted as a function of $H_x/H_o$, the pattern is calculated from Fraunhofer formula Eq. 3.5

It must be pointed out that due to the approximation involved in this method, some distortion of the Fraunhofer pattern from $I_p$ itself is not avoidable especially when $H_x$ exceeds $2.5H_o$. However, Most of the features of the diffraction pattern for a junction containing vortices are included in the low field range from $-2H_o$ to $+2H_o$ (see section 2.2). Therefore, it is usually sufficient to do the theoretical fitting in this range. One of the advantages of this method is being able to apply the magnetic field in either the x or y direction that is parallel to the junction. In most of our work on the motion of vortices, the diffraction patterns were measured by applying transport currents, $I_{py}$, in the Pb strip, then converting $I_{py}$ into $H_x$ via Eq. 3.6.

# CHAPTER 4. EXPERIMENTAL RESULTS AND DISCUSSION

In this chapter, we will present our experimental studies on the nature of single vortex motion inside SNIS Josephson junctions and the measurement of elementary pinning force in thin film Pb. First, we will discuss the technique used to create a single vortex inside the Josephson junction via a process by which transport currents nucleate a vortex at the edge of the thin film. Second, we will present experimental results on the single vortex motion to demonstrate that a single vortex can be moved around in SNIS junctions just as that in SNS junctions. By using the transport currents in both strips of the junction, we have been able to move the vortex virtually to most desirable places in the junction. Third, we will present the experimental results on the measurement of the elementary pinning force $f_p$ in thin film Pb. The temperature dependence of $f_p$ will be given, together with the discussion on some possible pinning mechanism associated with those observed results. Finally, some further experiments by means of this technique will be proposed which might lead to applications of these phenomena to microelectronic circuits.

## 4.1. Nucleation of Single Vortex

### 4.1.1. The forces acting on a single vortex in SNIS junctions

In studying single vortex motion, there are several forces acting

on the vortex that need to be considered. Even though some theoretical studies on the vortex energy in a single superconducting film have been done by Huebener[44], Tinkham[45] et al. relatively little theoretical work has been reported on the free energy study on an isolated vortex in a cross strip Josephson junction system. Three of the most important forces are the dipole interaction, the vortex-image interaction, and the interaction between the vortex and pinning center, in addition to the Lorentz force between the vortex and any applied transport currents. In this discussion a monopole description is used for mathematical simplicity.

1) The dipole interaction is between two inner poles of a dipole vortex trapped in the junction as shown in Fig. 4.1, where the inner pole from a single vortex trapped in the top superconducting layer tends to pull the one from a single vortex trapped in the bottom superconducting layer closer together. If two inner poles from a dipole are separated by a distance, $\delta$, the effective separation of two superconducting layers is $d_{eff}$, and provided that $\delta \gg d_{eff}$, the coupling force in this simple monopole approximation[46] is

$$F = \Phi_o^2/(8\pi^2 \cdot \delta \cdot d_{eff}) \ . \tag{4.1}$$

The coupling force F reaches a maximum value when two single poles actually line up, i.e., $\delta = d_s$. Then the maximum pinning force is given as

$$F_{Max} = \Phi_o^2/(8\pi^2 \cdot d_{eff}^2) \tag{4.2}$$

For $d_{eff} = 500$nm, the force is about $6.5\times10^{-14}$ N. It will be shown later that this force is about one order of magnitude smaller than the

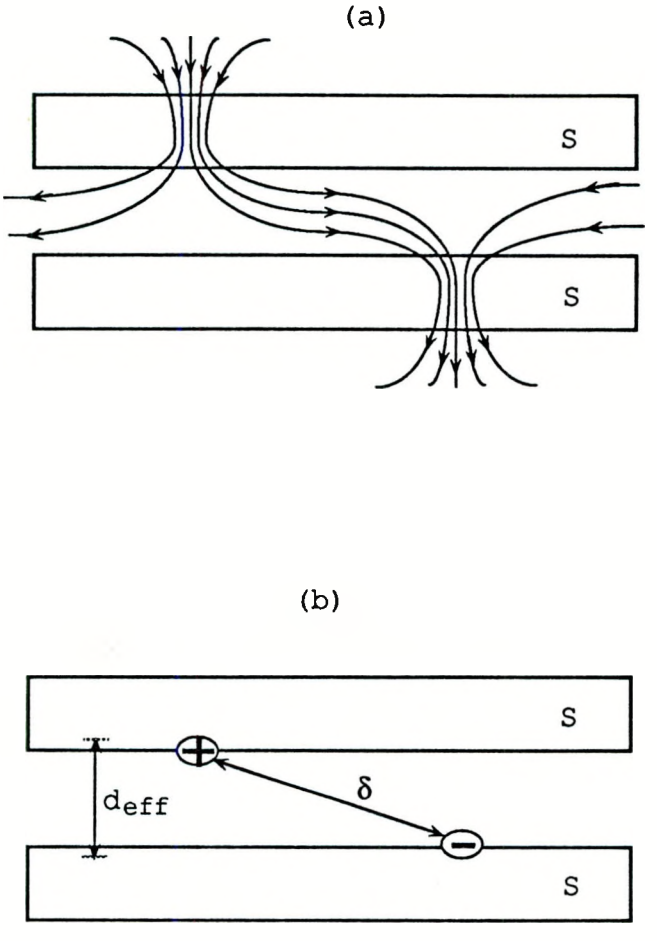


Fig. 4.1. (a) A misaligned dipole vortex, (b) Two magnetic monopole charges separated by a distance $\delta$ are theoretical equivalent to a misaligned dipole vortex

measured pinning force in the present experiment. Thus, in order to decouple the vortex in the bottom superconducting layer from the top superconducting layer, it is necessary to have a normal-metal layer thick enough to reduce the coupling energy between the top and bottom superconducting films.

2) The force from the vortex-image interaction is given by

$$f_m = [\Phi_o^2/(8\pi^2 \cdot d_{eff})] \cdot \sum [p \cdot (\mathbf{r}-\mathbf{r}_o)/|\mathbf{r}-\mathbf{r}_o|^2] \ , \qquad (4.3)$$

where $\mathbf{r}_o$ is the vortex position, $\mathbf{r}$ is the position of the images. p = +1 for same sense images, p = -1 for opposite sense images. The summation is over all images. The force arising from vortex-image interaction is an attractive one which reaches its highest value when the vortex is near the edge. As the vortex moves to the center of the film, this force decreases as $1/r^2$ which is strongly unfavorable to the motion of a single vortex from the edge to the interior of the junction. As soon as a vortex moves a distance about several times $d_{eff}$, this force gets much smaller. For example, 3$\mu$m ( ~ 5×$d_{eff}$ for sample SNIS#9 at 6.6K) away from the edge, the force $f_m$ is reduced by a factor of 25 from the value of $f_m$ for the vortex in a distance of $d_{eff}$ away from the edge. It will be shown in section 4.4.1, that $f_m$ can be totally neglected, if a vortex is more than one quarter of the width of junction away from the edge.

3) The pinning force, $F_p$, arising from the interaction between a vortex and pinning centers is the most important force holding the vortex inside the junction. $F_p$ arises from spatial variation in material parameters, such as the electron mean free path or the size

of the precipitates. The range beyond this distance is limited to the coherence length for core pinning or the penetration depth for magnetic pinning. $F_p$ differs from one kind of pinning center to another and is short ranged to those characteristic lengths. Whether a vortex can exist inside the junction depends on the strength of these pinning forces.

4.1.2. Vortex nucleation current and flux entry field

In the presence of a transport current $I_p$, a strong transverse magnetic field is built up near the film edge, since currents flow predominantly along the edge of the strip. At values of transport current, $I_p$, large enough to allow the local magnetic field at the edge of the film to exceed the critical field, $H_{c1}$ for type II superconducting material, the mixed-state structure appears along the edge of the film and vortices are nucleated. Usually a vortex will not enter the film at $H_{c1}$, however, because the image forces and the Lorentz forces from the circulating Meissner currents create an additional barrier to flux entry up to a flux entry field $H_{en}$. If $I_p$ is increased further to allow the local magnetic field to exceed these barriers for flux entry, $H_{en}$, the vortex breaks off and travels toward the film interior, driven by the interaction between the vortices and the transport currents. While in the vicinity of the film edge, the newly-formed vortex inhibits further nucleation through the effect of its return flux on the edge. If there are some pinning centers that are strong enough to trap the incoming vortex, the vortex will remain

in the film even after $I_p$ is reduced to zero.

In the four layer SNIS junction situation, the vortex nucleation process has some similarities to that for a thin film. However, the geometric aspect of a junction makes the problem theoretically much more difficult to handle than that of just an isolated thin film involved, because we have to consider the new factors that affect the problem, such as the superconducting coupling between top and bottom layers which could significantly alter the structure of the current density distribution both inside and outside the junction. So far, there is no theory available on vortex nucleation in the junction area by transport currents. The case for a cross strip junction differs from that for an isolated superconducting thin film, because of the so-called "grounding problem"[48] from the counter superconducting electrode. If a transport current is applied through the bottom layer of superconducting film, some currents originally flowing along the bottom surface of this film will be ejected to the top surface around the junction area because of the partial grounding effect from the top superconducting film. This grounding problem makes the current density distribution in the junction vicinity quite different from an isolated superconducting film. Since there is no adequate theory available at the time being, we will use the treatment by Huebener, Clem et al.[43,47] based on a single superconducting film as a very rough approximation to deal with the nucleation problem in the junction situation. Care is needed in using the theory to interpret experimental data which will be discussed later.

The Gibbs free energy of a flux line per unit length is given by Huebener[44], for a semi-infinite superconducting slab,

$$\frac{G}{L} = \frac{\phi_o}{4\pi}\cdot\left[H_a\cdot\exp\left(\frac{-x}{\lambda_L}\right)-\frac{1}{2}\cdot\frac{\phi_o}{2\pi\lambda_L^2}\cdot K_o\left(\frac{2x}{\lambda_L}\right) - (H_a-H_{c1})\right] , \qquad (4.4)$$

where x: distance from the edge,

$H_a$: perpendicular magnetic field,

$K_o$: zeroth order modified Bessel function, and

$H_{c1}$: lower critical field.

The first term contains the interaction between the vortex line and the external field. The second term describes the attractive interaction between the vortex line with its image lines. The third term represents the energy of the vortex line inside the superconductor far away from the surface.

The magnetic field around the superconducting strip of thickness $d_s$ and width W, generated by the transport current, $I_p$, is expressed in terms of $I_p$ as[43]

$$H_{//}(\text{surface}) = 0.8I_p/(d_s + W) \quad (\text{gauss-cm/Amp}) , \qquad (4.5a)$$

$$H_{\perp}(\text{edge}) = 0.4I_p/d_s \quad (\text{gauss-cm/Amp}) . \qquad (4.5b)$$

As a matter of fact, a vortex may not be nucleated immediately after the transverse field at the edge reaches the value of $H_{c1}$, due to the free-energy barrier near the edge, as given in Eq. 4.4. By including the free-energy barrier into consideration, the minimum flux entry field has been calculated by Clem[47] as

$$H_{en}(T) = H_{c1}(T)\cdot[1 + (2Wa_n)^{1/2}/4d_s] , \qquad (4.6)$$

where $a_n$ is the radius of the vortex core. Here, the aspect ratio can

make $H_{en}$ significantly higher than $H_{c1}$, because the condition $Wa_n >> d_s^2$ is normally true for our junctions. For example, at 6.6K, the minimum nucleation current for the Pb film was found to be 41mA, which gives $H_{en}$ = 430 gauss. However, $H_c(T=6.6K)$ for bulk Pb is about 130 gauss, using $H_c(0)$ = 803 gauss.

Combining Eq. 4.5b with Eq. 4.6, we obtain the minimum flux entry current, or so-called nucleation current $I_n$, as

$$I_n = [H_{c1}(T)/0.4]\cdot[d_s + 0.25\cdot(2a_nW)^{1/2}] \ , \qquad (4.7)$$

Bulk Pb is a type-I superconductor, but, as shown by Tinkham[49], a Pb film less than about 500nm thick will behave as a type II material and a fluxoid enters as a single quantum of flux. Therefore, we will simply use the same term "vortex" to describe the flux line in both Pb and PbBi thin films. Since the superconducting transition temperature of lightly Bi doped Pb thin films does not change much from that of a pure Pb thin film, for our sample SNIS#9, $T_c^{Pb}$ = 7.28K, $T_c^{PbBi}$ = 7.35K, we will use approximately the same value of $H_{c1}$ in the Eq. 4.7 for both Pb and PbBi thin film. The value of $H_{c1}$ could be obtained from the perpendicular thermodynamic critical field, $H_{c\perp}$, for thin film Pb.

Tinkham[49], Cody and Miller[50] have shown that $H_{c\perp}$ for a superconducting film is quite different from the bulk value $H_c$. Both theoretical and experimental studies on the relation between $H_{c\perp}$ and $H_c$ for thin film Pb have been conducted by Cody and Miller.[50] It is given as[50]

$$H_\perp(T,d_s) = \sqrt{2}\cdot\kappa(T,d_s)\cdot H_c(T), \qquad (4.8a)$$

$$\kappa(T,d_s) = [2\sqrt{2}\cdot\pi\cdot\lambda^2(T,d_s)\cdot H_c(T)]/\Phi_o \ , \qquad (4.8b)$$

where the quantity $\kappa(T,d_s)$ is the Ginzburg-Landau parameter which in theory is defined only near $T_c$, but, in the treatment of Tinkham[49], is used in the above form over the entire temperature range. In the thick film limit, i.e., $d_s > 1000$ Å, it has been shown[50] $H_c/H_\perp$ changes as $(1+t^2)$, where $t = T/T_c$. Using $H_c(T) = H_c(0)(1-t^2)$, $H_\perp$ changes as $(1-t^2)/(1+t^2)$. Near $T_c$, $H_\perp$ could be approximated as, ~ $(1-t)$. In the calculation of critical field, we use the value $H_{c\perp}(0) = 470$ gauss[50] for thin film Pb.

The concept used here for the core size of the vortex, $a_n$, is to describe the scale of magnetic flux enclosed in a vortex, not the scale of the normal electrons enclosed in the vortex, $\xi$. For Pb films, $a_n$ is different from that of PbBi, due to the type I nature of bulk Pb. For PbBi films, $a_n$ can be assumed to be equivalent to the penetration depth, $\lambda_L^{PbBi}(T)$. But for Pb film, $a_n$ should be calculated from $\pi a_n^2 \cdot H_c = \Phi_o$, as suggested by Clem[51], which gives $a_n = 2^{3/4}(\lambda\xi)^{1/2}$. Using $\lambda_L(0) = 39$nm, $\xi(0) = 83$nm for Pb, we obtained $a_n(0) = 96$nm, which is quite close to the core size of a vortex in the PbBi film. By inserting all relevant parameters for sample SNIS#9, together with their temperature dependence, we get the nucleation current, $I_n$, near $T_c$ for both Pb and PbBi strips as

$$I_n^{Pb}(T) = 89.4 \cdot (1-t_{Pb}) \cdot [1+2.14(1-t_{Pb})^{-1/4}] \ , \qquad (4.9a)$$

$$I_n^{PbBi}(T) = 132 \cdot (1-t_{PbBi}) \cdot [1+1.51(1-t_{PbBi})^{-1/4}] \ , \qquad (4.9b)$$

where $I_n$ is in units of mA, $t_{Pb} = T/T_c^{Pb}$, $t_{PbBi} = T/T_c^{PbBi}$. In the range of the measurements reported here, $I^{Pb}$ ranges up to 50mA and $I^{PbBi}$ ranges up to 57mA.

4.1.3. Temperature dependence of $I_n$

For experiments to move vortices around the junction, it is important that the current used to push the vortex, $I_p$, be less than the nucleation current, $I_n$. Hence, the first item to be determined is the temperature dependence of $I_n$. This specifies the temperature window where the $f_p$ measurement can be made. This window will be given in section 4.4.3.

To measure the temperature dependence of $I_n$, the sample is warmed up to 9K to eliminate possible pinned vortices in the junction and subsequently cooled down to the desired temperature below $T_c$. The zero field critical current of the junction free of any vortices, $I_o$, is measured as a reference point. Then a transport current, $I_p$, is increased to a certain value through one leg of the junction, and decreased to zero again. Then the critical current $I_{co}$ at zero field is measured to see if $I_{co}$ changed from $I_o$. If such a change does not occur, above process will be repeated with higher $I_p$'s and the value of $I_p$ is recorded, until the change does occur which indicates vortices have being nucleated. The minimum nucleation current $I_n$ is defined as the lowest value of transport current $I_p$ corresponding to the first change of $I_{co}$ from $I_o$.

Fig. 4.2a illustrates the experimental results on the measurement of $I_n^{Pb}$ and $I_n^{PbBi}$ at 6.6K. The two curves shown in the figure are typical ones of $I_{co}/I_o$ changing as a function of $I_p$ in the temperature range from 6.9K to 6.4K. As shown in the Fig. 4.2a, $I_n$ is 40.5mA for Pb film, while 48mA for PbBi film at 6.6K. Often rather

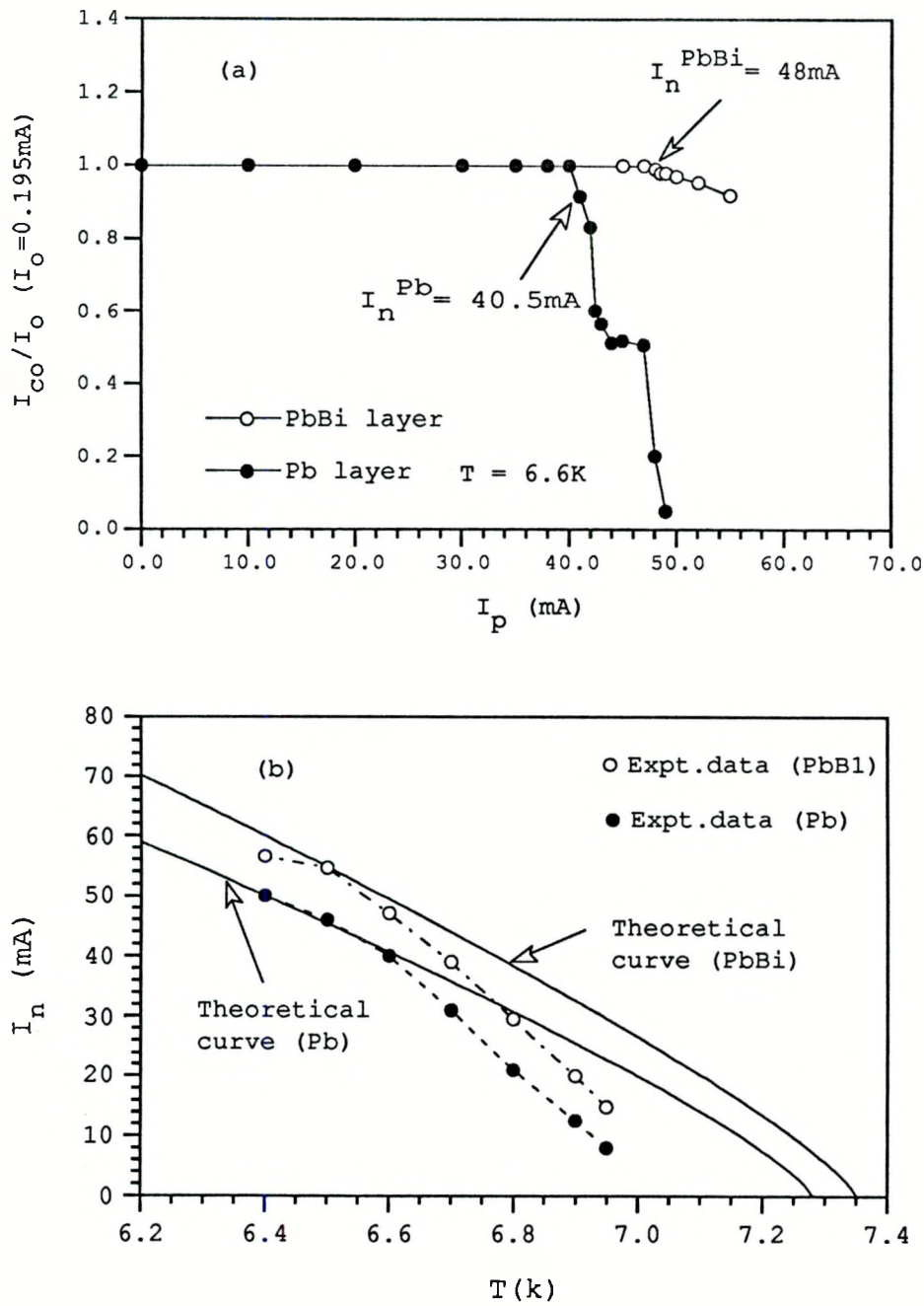


Fig. 4.2. (a) Plots of $I_{co}/I_o$ vs $I_p$ to illustrate the determination of nucleation current $I_n$ at 6.6K. (b) $I_n$ changes as a function of T, the solid lines are calculated by using Eqs. 4.9

small increases in $I_{Pb}$ above $I_n^{Pb}$ will cause a sharp decrease of the value of $I_{co}/I_o$ which indicates the vortex has been pushed quite a distance into the junction. As a contrast, $I_{co}/I_o$ for the PbBi film decreases rather gradually as nucleation currents go up, and the value of $I_n^{PbBi}$ is about 20% higher than $I_n^{Pb}$. Such a slowly changing behavior of $I_{co}/I_o$ as a function of $I_p$ for the PbBi film may be due to relatively strong pinning in PbBi films on the nucleated vortex, or some other mechanism unknown at present time.

The temperature dependence of $I_n$ for both Pb and PbBi layer is shown in Fig. 4.2b. The solid lines are the calculated curves from Eqs. 4.9 using the resistive definition of $T_c$ which are 7.28K for Pb film and 7.35K for PbBi film. The overall agreement between the experimental results and the theory is poor. Considering there are no adjustable parameters in Eqs. 4.9, the agreement is reasonable below 6.7K, or $t < T/T_c = 0.9$. It seems the junction, at temperatures very close to $T_c$, is quite sensitive to the transport currents. However, the reason for that has not been understood.

### 4.1.4. Nucleation of a single vortex

The nucleation of a single vortex using a transport current in the thin film has proved to be very reproducible and equivalent to the field cooling method. Any relatively weakest spot near the edge of the film in the junction area can be the place where the first single vortex is nucleated and subsequently pushed to the interior even before a second one being nucleated. The experiments, concerning the

single vortex motion, reported here were performed on sample SNIS#9, which has sufficiently thick normal layer to allow vortices to penetrate only one of the two superconducting films. The vortex was always nucleated in the Pb layer because of the sharp decreasing character in the $I_{co}/I_o$ vs $I_p$ curve.

The procedure to nucleate a single vortex in the Pb film is as follows:

1) The sample is warmed above 9K, and held for a few minutes to eliminate possible trapped vortices.
2) The sample is slowly cooled through $T_c$ down to 5K and $I_o$ is measured as a reference point.
3) The sample is warmed up slowly to a desired temperature, say 6.6K. The current in the Pb film, $I_{Pb}$, is increased to some value, and then decreased to zero.
4) The sample is cooled back to 5K again. The critical current at zero field, $I_{co}$, is then measured to see if it has changed from $I_o$.
5) If $I_{co}$ has not changed from $I_o$, steps 3 to 4 will be repeated with higher currents $I_{Pb}$, until some change of $I_{co}$ is observed. If $I_{co}$ has changed from $I_o$, a full diffraction pattern $I_c/I_{co}$ vs $H_x$, is normally taken to determine the configuration of the vortices.
6) $I_{co}$ changing from $I_o$ indicates vortices have been nucleated. If a higher value of nucleation current, $I_{Pb}$, was used to nucleate a vortex in a different site, the sample was usually

warmed up to 9K and the whole process was repeated all over again.

The reference temperature was set at 5K in our experiments because the critical currents at temperatures higher than 6K for sample SNIS#9 are too small to give diffraction patterns of sufficiently good quality. But the accuracy of the diffraction patterns measured at 5K permits the determination of the vortex location by performing the theoretical fitting to those diffraction patterns to 1% of the junction width. It was found the diffraction patterns did not change on cooling to 4.2K and warming up to 6.9K so the vortex is believed not to move in this temperature range.

For the Pb film after nucleation, slight increases in $I_{Pb}$ cause a rather fast decline in $I_{co}/I_o$. This is shown in Fig. 4.3, where the value of $I_{co}/I_o$ is plotted versus $I_{Pb}$ for two different temperatures of 6.6K and 6.7K. A study of the full diffraction pattern for each point marked from A to E along the curve at 6.6K shows that the decrease of $I_{co}/I_o$ arises from the motion of a single vortex into the junction, and not from the nucleation of additional vortices near the edge. Site A, at $I_{Pb}$ = 42.5mA; site B, at $I_{Pb}$ = 43.0mA; site C, at $I_{Pb}$ = 44.0mA, site D, at $I_{pb}$ = 45.0mA; site E, at $I_{Pb}$ = 47.0mA; marked on Fig. 4.3 for 6.6K data, correspond to the diffraction patterns of Figs. 4.4a to 4.4e respectively.

One diffraction pattern, $I_c/I_o$ vs $H_x/H_o$, for each site was normally measured. For each diffraction pattern, A through E, the solid lines are least-squares fits of the single vortex model and

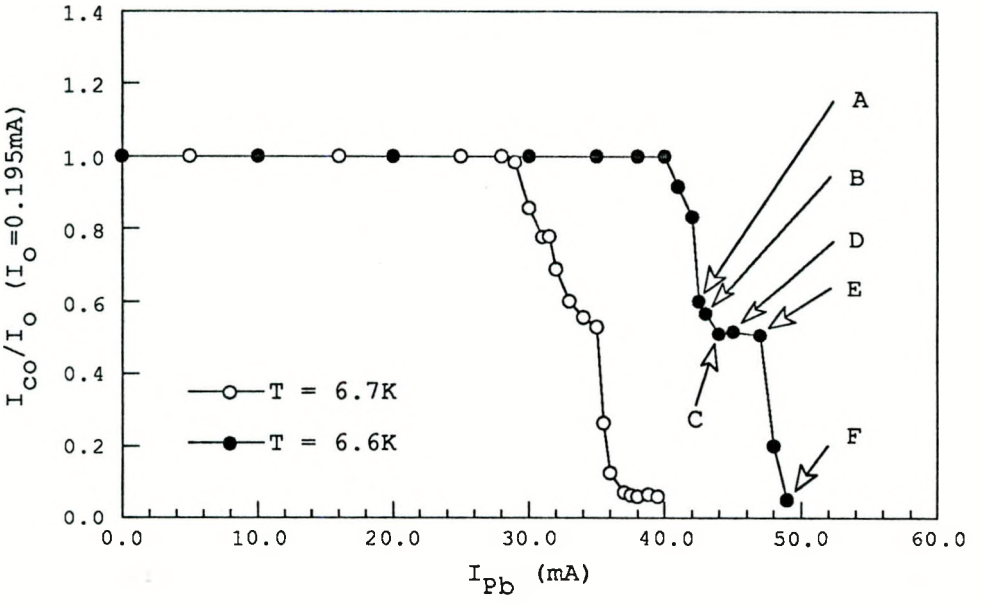


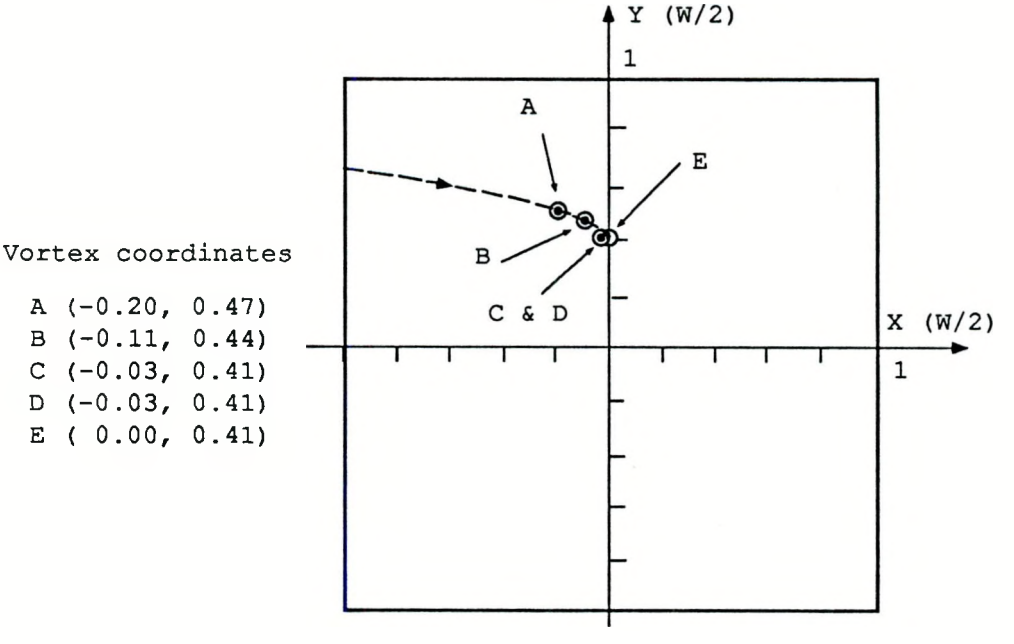


Vortex coordinates

A (-0.20, 0.47)
B (-0.11, 0.44)
C (-0.03, 0.41)
D (-0.03, 0.41)
E ( 0.00, 0.41)

Fig. 4.3. Plot shows changes in $I_{co}/I_o$ as a vortex is nucleated at the edge and propagates into the junction at 6.6K and 6.7K. The sketch shows the sites of the vortex at five locations

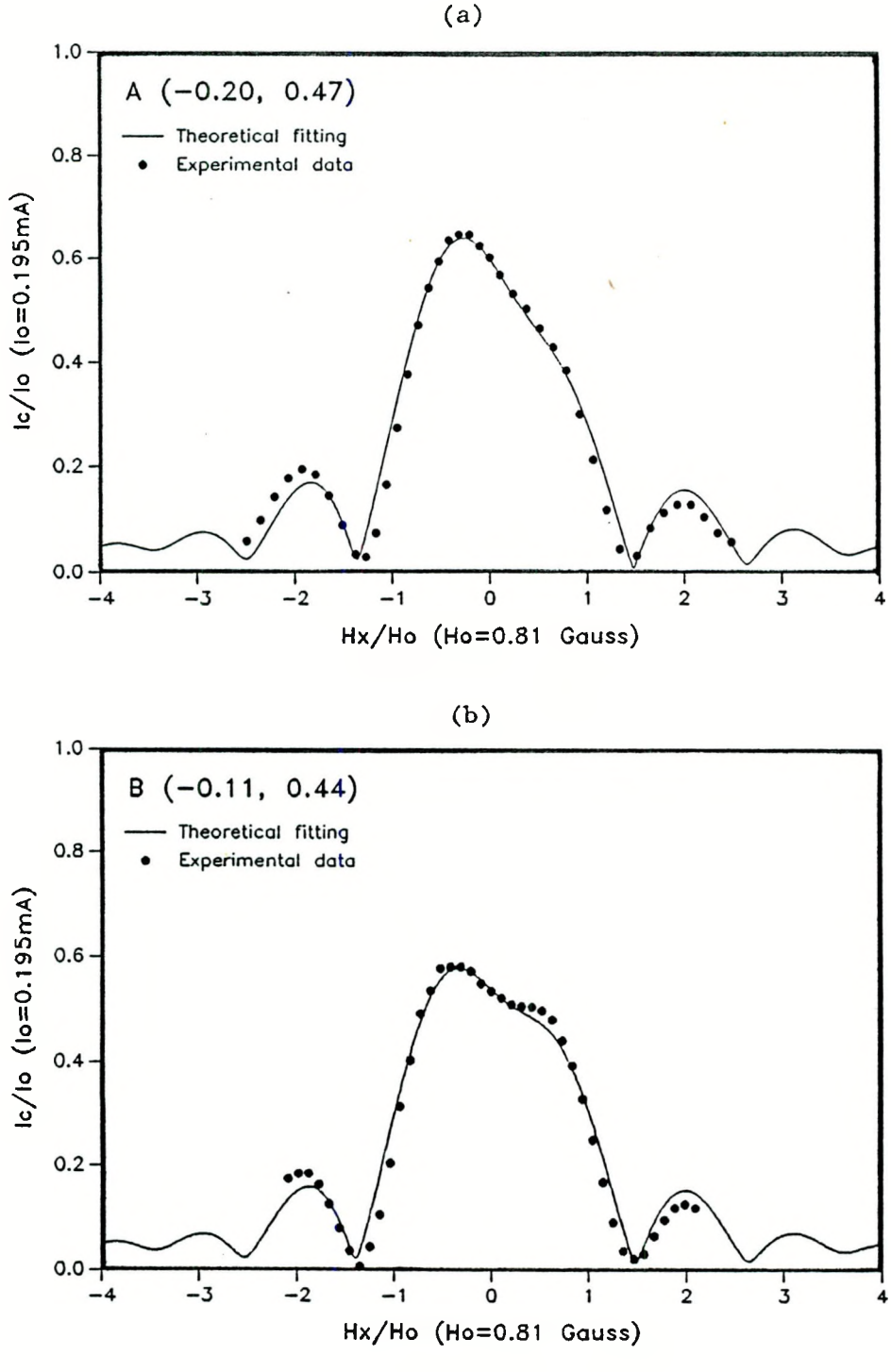


Fig. 4.4. The diffraction pattern $I_c/I_o$ vs $H_x/H_o$ for vortex (a) site A, (b) site B

(c)

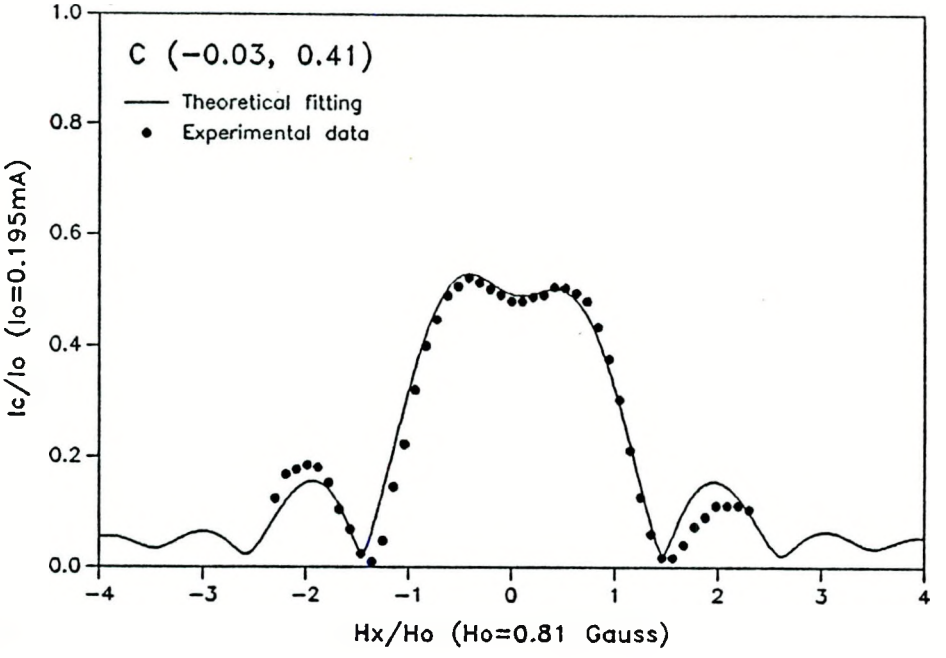


(d)

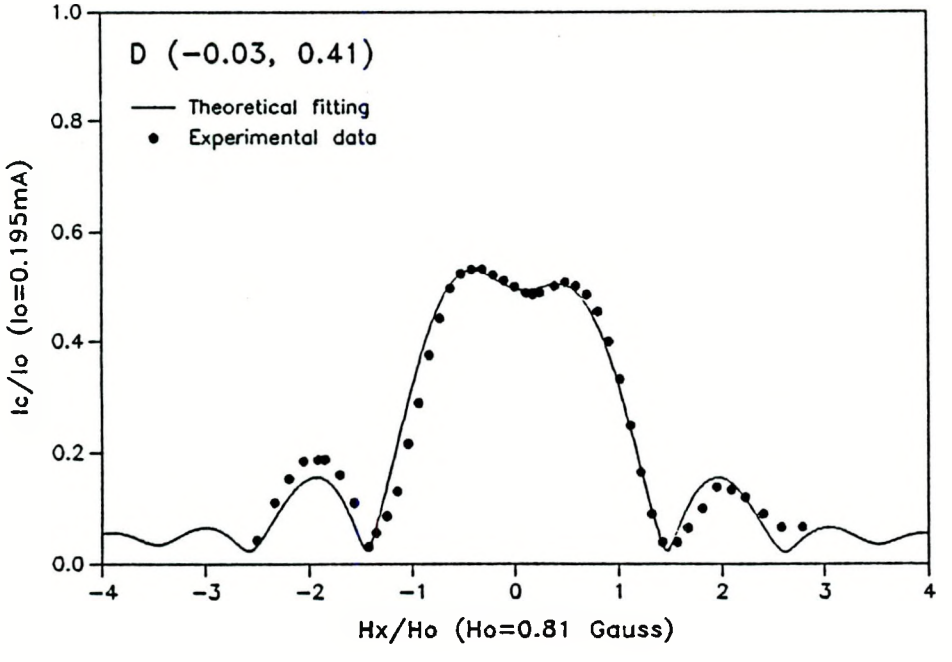


Fig. 4.4. (Continued)
(c) site C, (d) site D

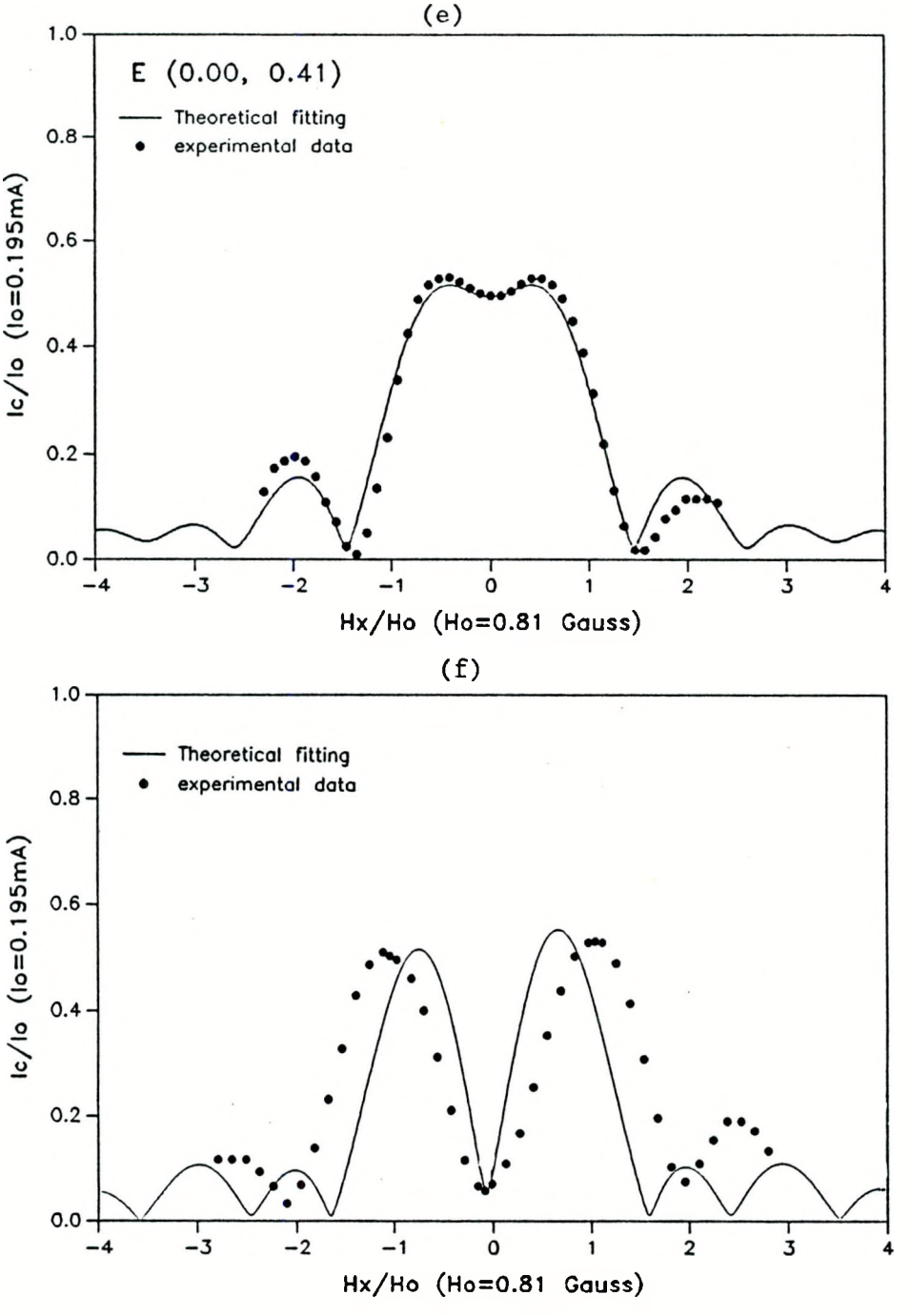


Fig. 4.4. (Continued)

(e) site E

(f) For diffraction pattern F, no single vortex model would be able to describe the data

solid circles are experimental data. The vortex locations were determined to be site A (−0.20, 0.47), site B (−0.11, 0.44), site C (−0.03, 0.41), site D (−0.03, 0.41), and site E (0.00, 0.41) in units of the half-width of the junction, W/2. These locations are illustrated by the sketch shown in Fig. 4.3, where the whole trajectory is plotted. Close to the edge of the junction, diffraction patterns differ very little from a Fraunhofer pattern so it is difficult to specify just where it is along the junction edge. When the vortex is about 15% of W/2 away from the edge, the distortion of the diffraction pattern are large enough to specify the location to about 2% of W/2, or 1% of the total width of the film.

For diffraction patterns C and D, the theoretical fitting gives the same vortex location where we only required the fitting accuracy to reserve two digits after each decimal point, even though it is noticeable their diffraction patterns are a little bit different. Considering the fact our experimental error could be around 2% of W/2 and some already existing discrepancy between the measured Fraunhofer pattern for the junction and theoretical Fraunhofer pattern, we felt that it is reasonable to reserve only two digits after each decimal point when we specify the absolute location of the vortex.

To solve the symmetry problem in determining the proper quadrant where the vortex is located, (to be discussed in detail in section 4.2.3), we measured the diffraction patterns $I_c/I_o$ vs $H_y/H_o$ for some vortex locations. Shown in Fig. 4.5, there are two diffraction patterns, $I_c/I_o$ vs $H_x/H_o$ and $I_c/I_o$ vs $H_y/H_o$ for location D as labeled on

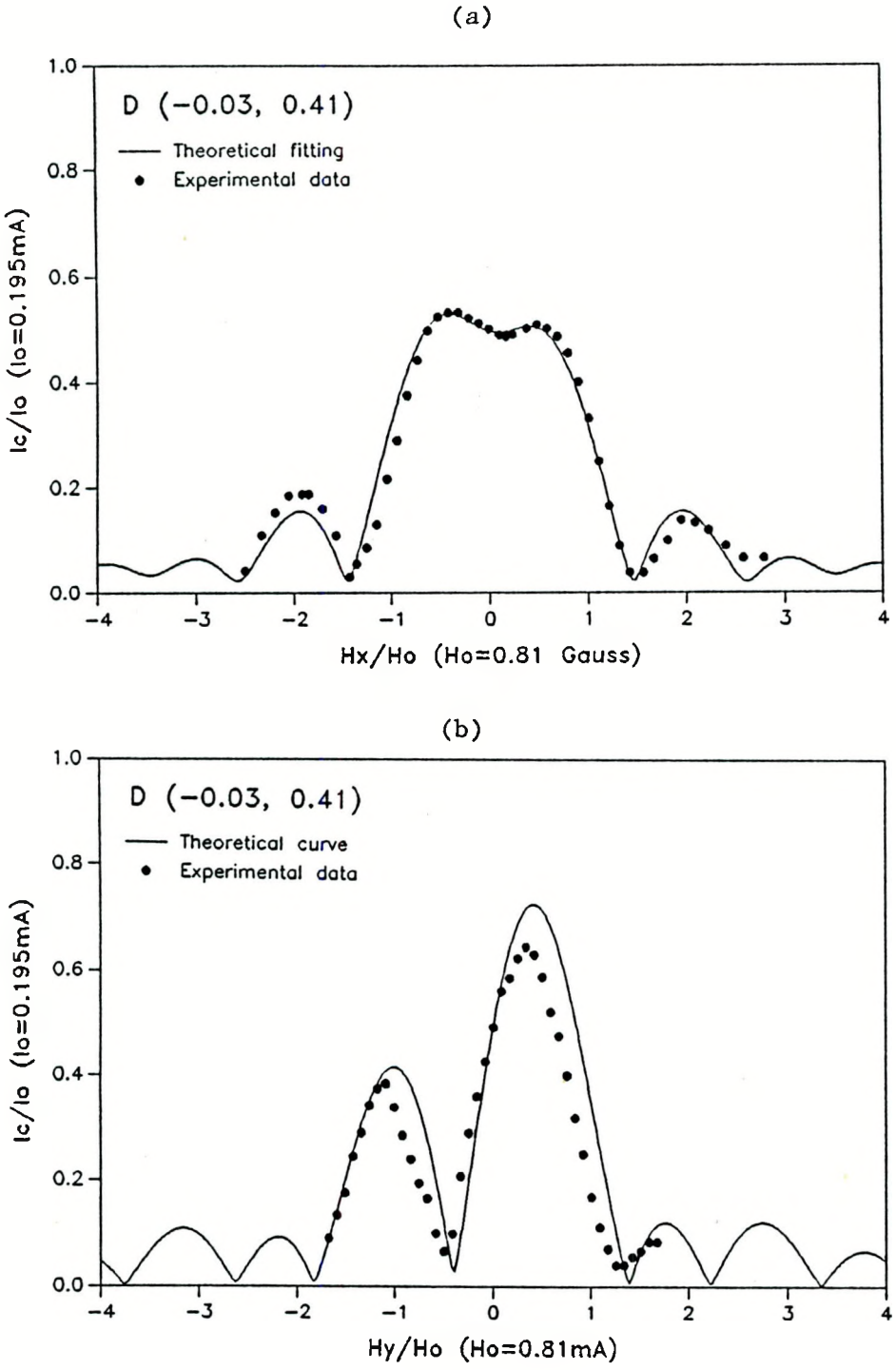


Fig. 4.5. Two diffraction patterns for site D with different parallel field direction (a) $I_c/I_o$ vs $H_x/H_o$, (b) $I_c/I_o$ vs $H_y/H_o$

curve at 6.6K in Fig. 4.3. The fitting to the data, $I_c/I_o$ vs $H_x/H_o$ in Fig. 4.5a, was done with two variable parameters for the single vortex coordinates, which turns out to be (-0.03, 0.41) for site D. The theoretical curve, $I_c/I_o$ vs $H_y/H_o$ shown in Fig. 4.5b, is calculated by assuming the vortex at position D (-0.03, 0.41) determined from the first fitting result to $I_c/I_o$ vs $H_x/H_o$ curve. Here, it should be noted that the theoretical curve, $I_c/I_o$ vs $H_y/H_o$, is not the vortex fitting curve, but a calculated one to verify only one single vortex is in the junction. Even through the matching between theoretical curve and experimental data for $I_c/I_o$ vs $H_y/H_o$ is not as good as $I_c/I_o$ vs $H_x/H_o$, the result is acceptable.

If $I_{Pb}$ is increased to 49mA or site F in Fig. 4.3, it is not possible to model the diffraction pattern with one vortex in the junction. As shown in Fig. 4.4f, if the data are fit at zero field, the peaks at higher field are too far apart. The only locations where the $I_c$ is close to zero at zero field $H_x$, are close to the origin. The fit by the solid line is the best fit for the one vortex situation with position at (-0.02, 0.05). Presumably there are multiple vortices existing in the junction. For this case it is difficult to find a unique fit.

If the sample was warmed up to 9K and the whole process was repeated again, the trajectory by which the vortex nucleated was found very close to the one plotted in Fig. 4.3. The exact location of the vortex from two nucleation processes at the same temperature may be slightly different, but the variation in the vortex coordinates was

found to be less than ±0.04 of W/2. For example, by applying $I_{Pb}$ = 45mA, the vortex was always found within the circle of radius of 0.04 of W/2 centered at site D (-0.03, 0.041). Even the nucleation current is the range of $I_{Pb}$ = 45±2mA, the vortex was still found in that circle.

If the nucleation temperature is at 6.7K, we still found a single vortex can be nucleated by applying $I_{Pb}$, but the location of the vortex is little different from that at 6.6K. No systematic study was done at this temperature.

The vortex nucleated by this process was found to be quite stable at the temperature below 6.9K, where the pinning is believed to be strong enough to resist external agitation such as thermally activated flux motion. The stability was confirmed by the identical diffraction patterns when warming the sample to 6.7K, 6.8K, and 6.9K, then cooling back to 5K for measuring. If the sample temperature was raised to 6.92K, a slightly different diffraction pattern was observed so we concluded that the vortex had changed the position. In the time scale, the vortex kept at 6.6K for two days was found to stay at the same location. It is also true for a week at 4.2K. However, it has not been tested for the time longer than one week.

The vortex used later for the study of the vortex motion and measurement of elementary pinning force is created by such a nucleation process which has been proved to be successful and quite reproducible.

The alternative way to create a single vortex in the junction

is to use *Field Cooling Process* (FCP), by which O. B. Hyun[13,15,16] had trapped a single vortex in one of the superconducting layers of his SNS junction. The detailed experimental procedure has been described in his Ph.D dissertation.[16] In the present work, we were not able to trap a single vortex in the junction. Shown in Fig. 4.6a, is the change of the ratio, $I_{co}/I_o$, as a function of cooling field $H_z$ in the unit of $H_{zo}$, where $H_{zo}$ is given by $\Phi_o/S$; and S is the junction area. For sample SNIS#9, the junction area is 55$\mu$m×55$\mu$m so $H_{zo}$ equals 6.8mG. Two steps were found on the $I_{co}/I_o$ versus $H_z$ curve. One shows $I_{co}$ changes 6% of $I_o$, as the field $H_z$ increased to 6.0 mG ($0.9H_{zo}$) and more, while the other shows $I_{co}$ changes 4% of $I_o$ at $H_z$ is equal to and less than −16mG ($2.4H_{zo}$). The asymmetric behavior of the $I_{co}/I_o$ vs $H_z$ curve might be due to some residual fields inside the sample chamber. Such a little change of $I_{co}$ remains the same as the perpendicular field $H_z$ increased up to ±50 mG which is more than seven times the required field, $H_{zo}$, for trapping one vortex in the junction area. Shown in Fig. 4.6b is the measured diffraction pattern (by open circles) corresponding to $H_z$ = 10mG. Very little distortion of the diffraction pattern leaves a large uncertainty in determining the vortex location. Such a pattern does not change even as the highest possible depinning currents are applied. It probably means one or more vortex dipoles with slight misalignment are trapped in the junction. Presumably, the normal layer in junction SNIS#9 is not thick enough to effectively decouple the two superconducting layers so that it is not possible to trap a vortex only in one of the superconducting films and it leaks

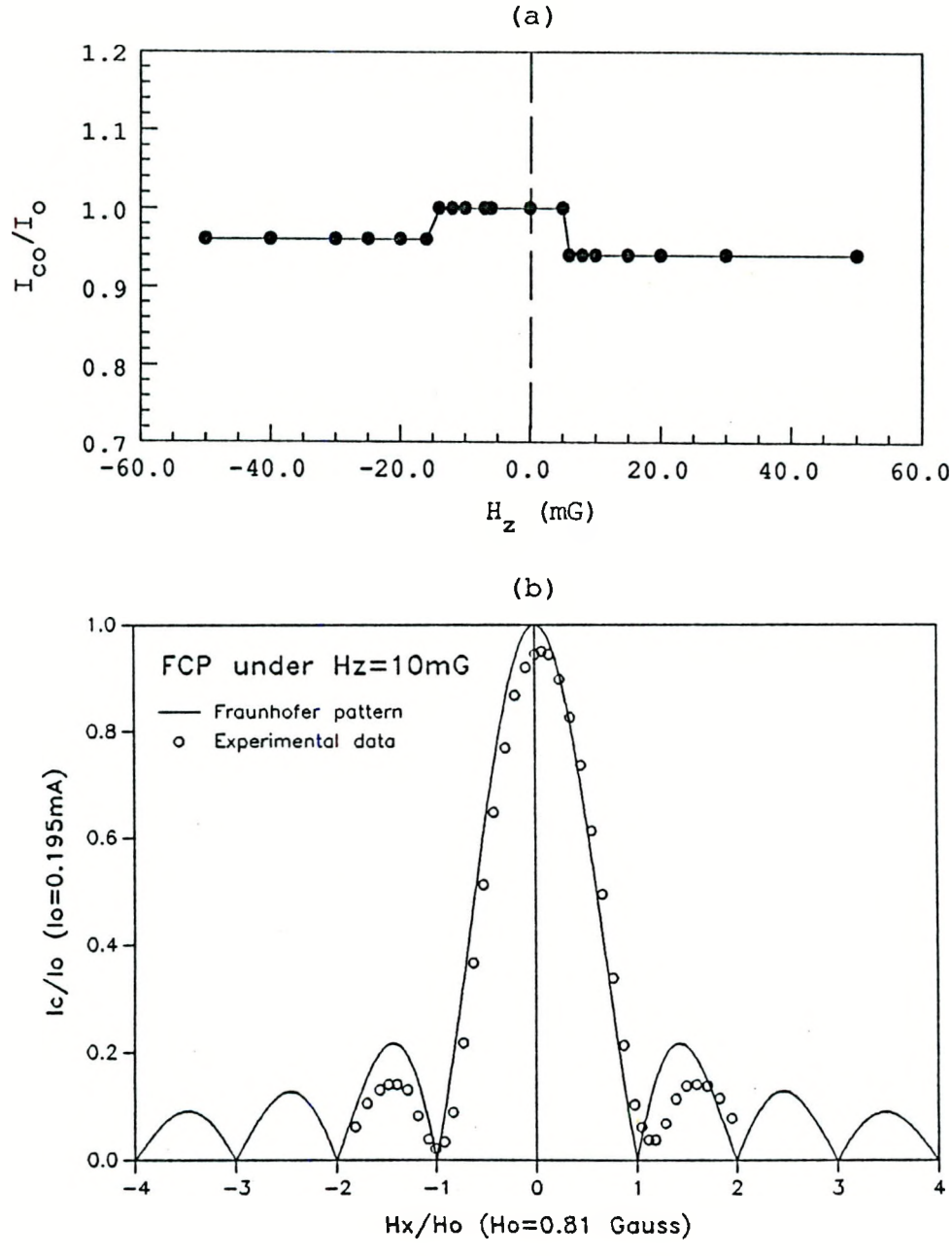


Fig. 4.6. (a) $I_{co}/I_o$ vs $H_z$, after the field cooling process
(b) The measured diffraction pattern (open circles), after the sample cooled under $H_z$ = 10mG. The solid line is the theoretical Fraunhofer pattern using $H_o$ = 0.81 Gauss

out the edge of the junction. But it is thick enough to use $I_n$ to nucleate a vortex which might be more favorable method for trapping a vortex in only one film. No further study was made on the field cooling process.

## 4.2. Experimental Study on Single Vortex Motion

In the previous section, we presented the experimental results to show that a single vortex can be nucleated in the junction by a transport current in a Pb film. In this section, we will give some other experimental results to demonstrate that such a nucleated single vortex can be moved around by a driven force from transport currents in either one of the strips of the junction.

Throughout this section, the vortex considered is nucleated by the technique described previously, and is always in the Pb film. It will be assumed to move like a rigid long slender magnet bar with two opposite magnetic monopoles embedded on the opposite surfaces within the depth $\lambda_L$ of the Pb layer, even though this treatment may lack theoretical justification.

In the first part of this section, we will briefly discuss the x-direction motion of the vortex driven by the Lorentz force from the transport currents in its own trapped layer, which is the Pb film oriented along the y-direction. Then, we will demonstrate how a vortex trapped in the Pb layer can be moved in the y-direction by

applying transport currents in a different PbBi layer. The symmetry-related problem of determining the vortex type will be solved at the end of this section. The elementary pinning force will be discussed merely for the purpose of comparing the strength of various pinning centers. This topic, together with the temperature dependence of $f_p$, will be discussed in more detail in the following section.

### 4.2.1. Vortex motion along the x direction

It is well known that the direction of motion of the vortex in the material depends on the driving Lorentz force and the restraining pinning force. The vortex then goes along the path of minimum free energy. If the strength of each pinning center is different, and their locations are distributed randomly, the outgoing path of a vortex driven by the Lorentz force via a transport current may not be exactly the same as the return path when the current is reversed.

In order to find out how the vortex moves under the influence of a transport current $I_{Pb}$, a careful experiment was carried out to investigate this vortex motion mystery. Is there a reversible path by which the vortex can be moved back? How long is such a reversible path as compared to the size of the junction? How does the temperature affect the vortex motion? What is the distance between two nearby pinning centers?

The obvious direction to push a vortex in the Pb film is along the x-direction using $I_{Pb}$ ( same as $I_{py}$ in the sketch shown in Fig. 3.10 ) to create the Lorentz force. The vortex just nucleated at 6.6K

is normally trapped at a very strong pinning center. Usually, it was not possible to move it by $I_{Pb}$ in either the +x or -x direction without further nucleation of the vortex. The only way to move it is to increase the sample temperature, for example to 6.8K. It was found that if the vortex were pinned in the area near the film center, such as those sites marked as C, D, and E in Fig. 4.3., then the vortex could actually be quite easily moved at 6.8K.

By applying 45mA transport current in the Pb layer. we nucleated a vortex labeled as A in Fig. 4.7, and it was found to be locate at (-0.02, 0.40) from its diffraction pattern. Then the temperature of the sample was raised and held at 6.80K to perform the depinning experiment. It should be mentioned again the depinning currents we used in the whole experiment were always contolled below the corresponding nucleation current at the same temperature.

First of all, we begin to push the vortex in the +x direction by slowly applying a depinning current $I_{Pb}$ to a certain value. A diffraction pattern was then measured to see if any change can be observed within the accuracy of our experimental technique. The difference between two adjacent values of $I_{Pb}$ is controlled to 1.0mA or less in order to detect as small a vortex moving displacement as possible. Every different location of the vortex during the motion was determined from its corresponding diffraction pattern. Shown in Fig. 4.7a is a plot of the X co-ordinate of the vortex as a function of depinning current $I_{Pb}$, showing the stepwise progress of the vortex across the junction under the influence of increasing $I_{Pb}$. For a

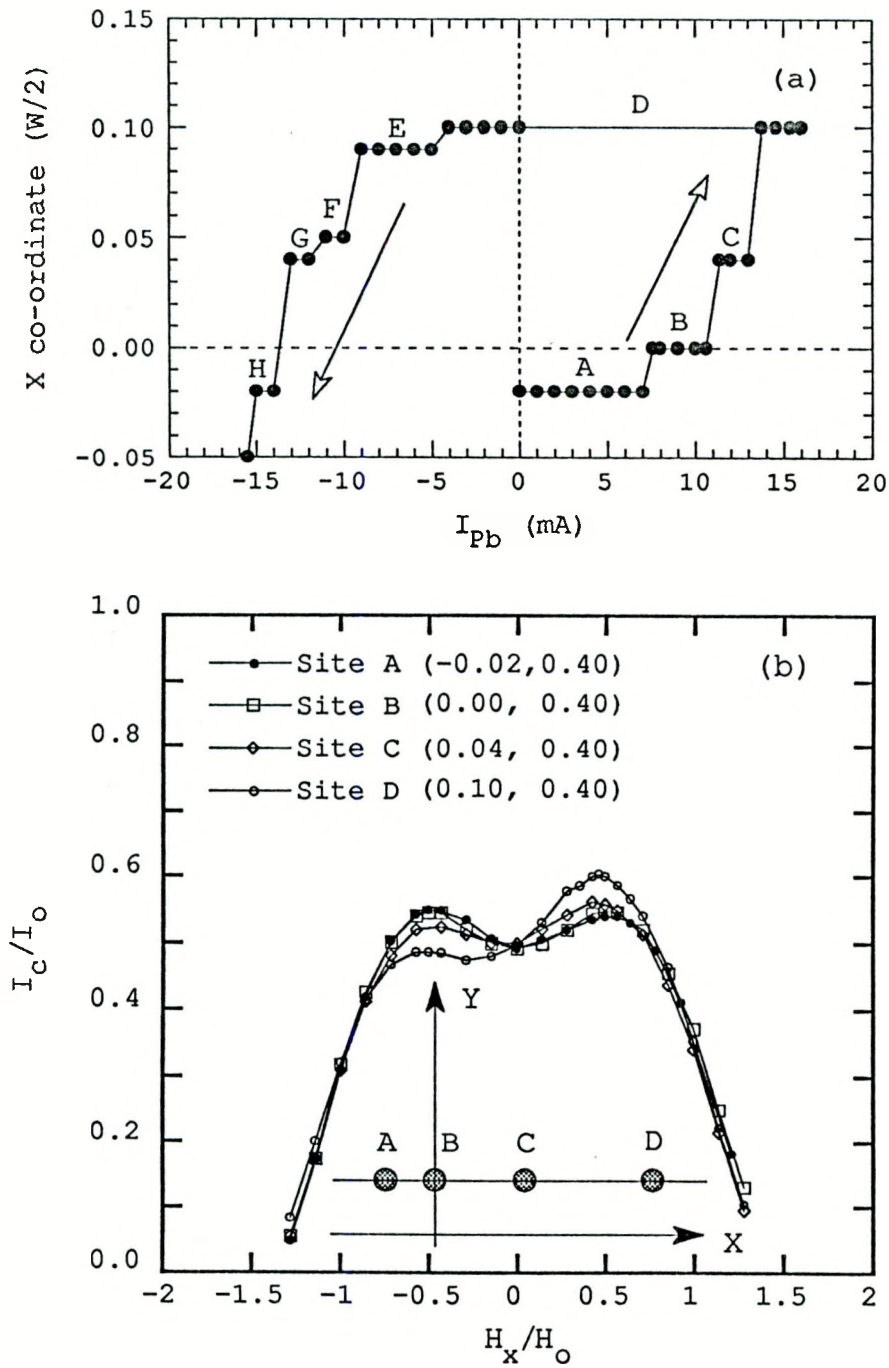


Fig. 4.7. (a) Vortex X co-ordinate plot showing the stepwise progress of the vortex driven by $I_{Pb}$, (b) Changes in diffraction patterns indicate the vortex progresses from site A to D

vortex driven along the x-direction from A (-0.02, 0.40) to D (0.10, 0.40), two intermediate stops were found, marked as B (0.00, 0.40) and C (0.04, 0.40). The total distance between A and D is 0.10 in units of W/2, which is about 2.5$\mu$m, so that two average pinning sites in our Pb film are separated by 0.5$\mu$m to 1.0$\mu$m.

Shown in Fig. 4.7b, are the center part of the diffraction patterns corresponding to four different pinning sites A through D respectively to show how they change when the vortex moves. Since those pinning sites are quite close together, such a change is not very much from one to another. But it is obvious to see that two equal height peaks characterize the diffraction pattern (shown by open squares) for the vortex pinned at site B which is the center of the film. When the vortex moves away from the center, one of the peaks in the diffraction starts increasing, while the other one decreases. This is clearly demonstrated by the diffraction pattern for site C (0.04, 0.40), shown by open diamonds, and the one for site D (0.10, 0.40), shown by open circles. The inset shown in Fig. 4.7b represents their relative positions.

At the point when the vortex was trapped at position D, we reversed the direction of $I_{Pb}$. It was found that the vortex followed the original path back. When $I_{Pb}$ reached the value of -14 mA, the vortex moved to position H, which was found to have the identical diffraction pattern as that for A. It was believed the vortex had essentially returned to its starting position A. However, the other places where the vortex stopped in between site D and H were different

from those between sites A and D.

It is quite difficult to answer whether such a "reversible" moving path is just a coincidence, since we did not perform the same experiments to many other paths. Generally speaking, it was found that the vortex often can be pushed back to its original place by reversing the current direction, providing the displacement was less than 5% of w/2. If the vortex travelling quite a distance ( > 5% of W/2), a simple reversal of $I_{Pb}$ often does not bring the vortex back, which has been demonstrated in a rather simple experiment performed as follows.

If, at the time when the vortex was removed to point D, $I_{Pb}$ was not reversed as described above, but increased a little more to 16.6mA, ( note! $I_n^{Pb}(6.8K) > 19mA$ ) we got a rather different situation. The vortex was moved much further away from the center of the film, to a new position $D^*$ (0.31, 0.49). Shown by the solid circles in Fig. 4.8, is again the plot of X coordinate of the vortex, as a function of $I_{Pb}$. It is similar to the plot shown in Fig. 4.7a, but there is one more step corresponding to $I_{Pb}$ = 16.6mA. At this location, it was impossible to depin the vortex by any value of $I_{Pb}$ less than $I_n^{Pb}$ at 6.8K. Presumably, the vortex was pinned by a very strong pinning center.

Also shown in Fig. 4.8, is the experimental result at 6.7K for the x-direction motion of the vortex initially pinned at the same position A as the one at 6.8K. It was found that the vortex could be moved back and forth by applying current $I_{Pb}$ in a similar fashion to

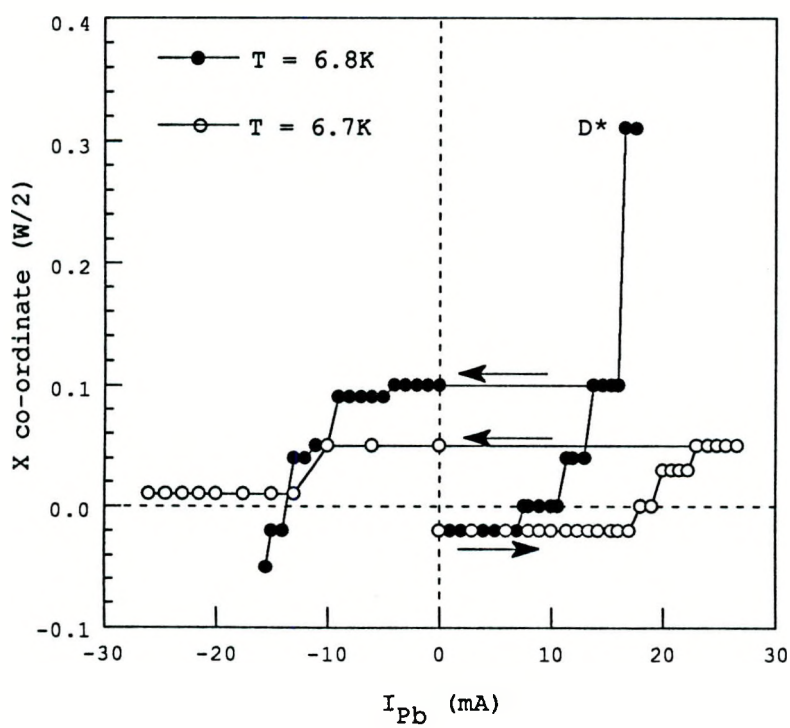


Fig. 4.8. The plot of X coordinate of the vortex as a function of $I_{Pb}$ for temperatures at 6.7K and 6.8K. $I_{Pb}$ is first increased from zero to some positive value, then reversed the direction as shown by arrows

the case at T = 6.8K. However, the vortex could not be returned back to the original position A within the limit of $I_{Pb} < I_n^{Pb}$ either.

When the sample temperature was increased to 6.9K, the vortex was extremely sensitive to the transport current. Small value of $I_{Pb}$ (less than 0.2mA) could drive the vortex quite a distance, and the result was not reproducible. Presumably, the thermal activation energy at 6.9K is comparable to the pinning potential of many pinning centers in our Pb film so the motion of the vortex is very sensitive to the fluctuation.

### 4.2.2. Vortex motion along the y direction

In order to move the vortex along the y direction, the Lorentz force exerted on the vortex has to be along the y axis. Such a force can be obtained by applying a transport current in the PbBi film. However, in this case, the vortex and currents are not in the same film so that the interaction of vortex with this current is not so straightforward as where the current is in the Pb film.

As illustrated in Fig. 4.9, the transport current $I_{PbBi}$ in the top PbBi film creates a magnetic field in the barrier region which in turn induces screening currents, $I_{in}$, flowing along the x direction across the top surface of the Pb film. These currents then produce a Lorentz force on the vortex in the Pb film along the y direction.

To illustrate the y direction motion, a vortex is nucleated in the Pb film and moved in the x direction to site A as shown in Fig. 4.10. The diffraction pattern and theoretical fitting give the

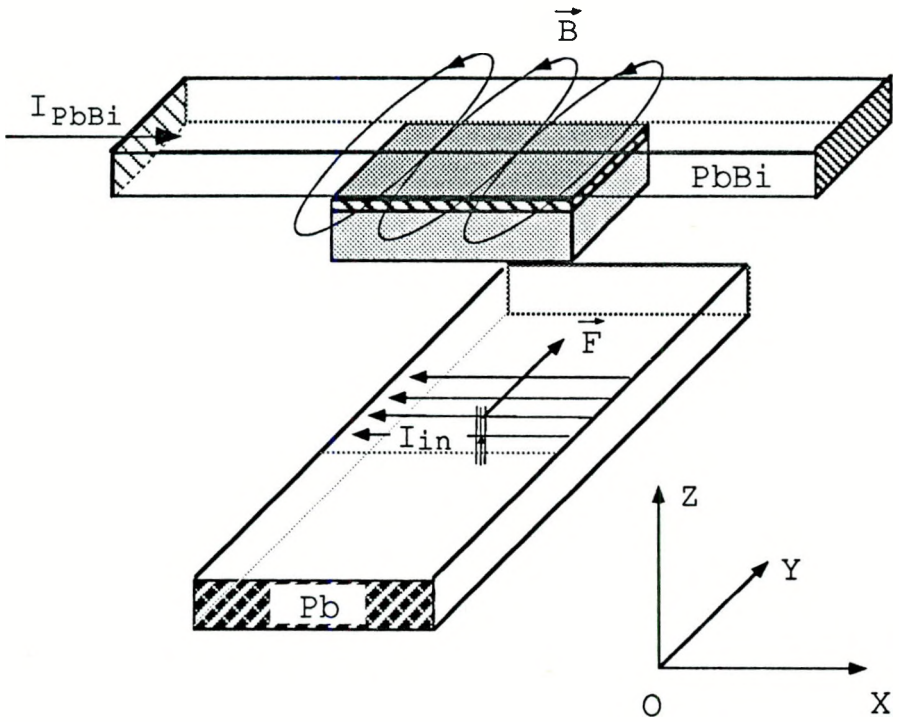


Fig. 4.9. Junction geometry showing the currents induced in the Pb film, $I_{in}$, by transport currents in the PbBi film, $I_{PbBi}$. Hence the vortex in the Pb film is pushed by a Lorentz force along the y direction

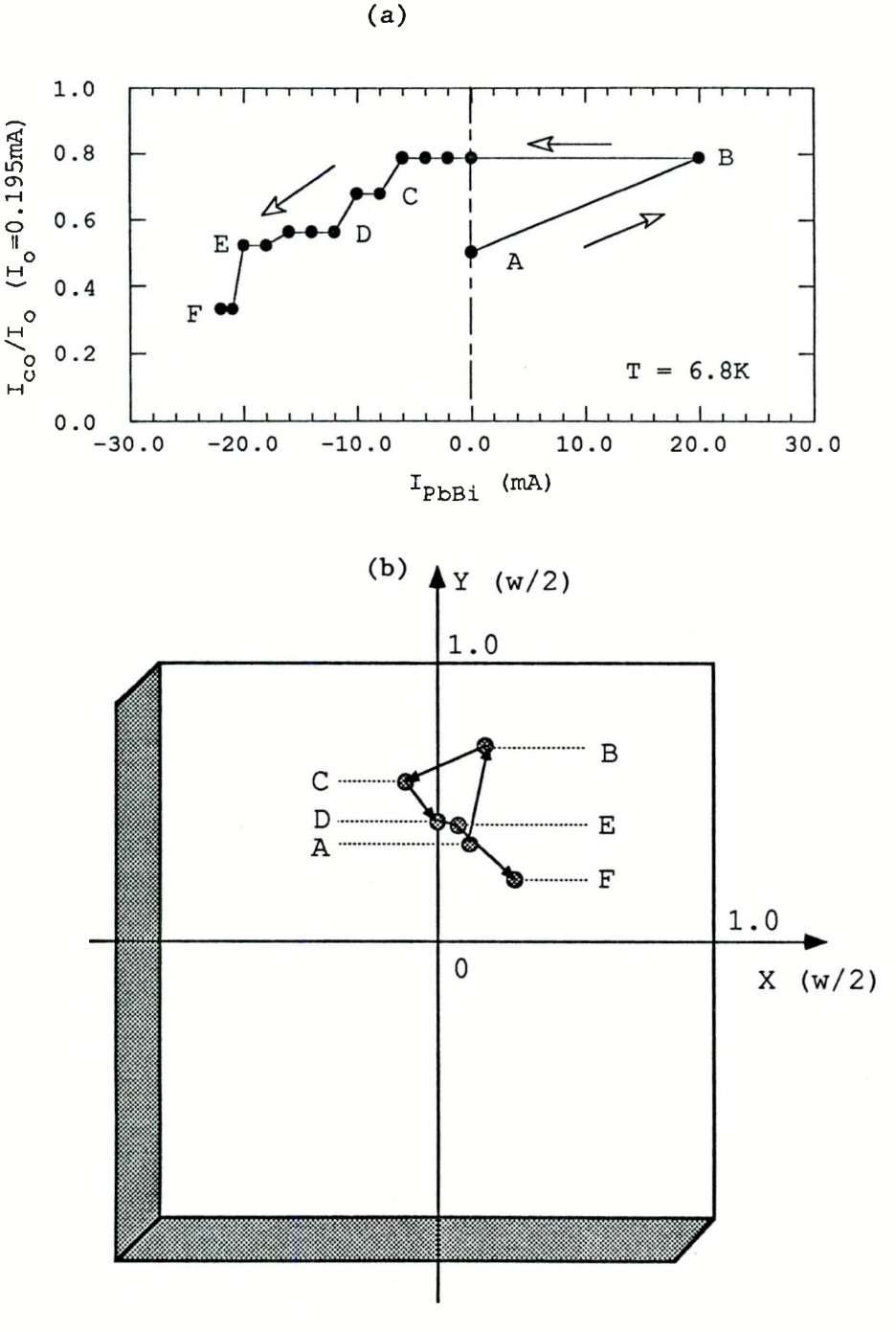


Fig. 4.10. (a) Plot of $I_{co}/I_o$ vs pushing currents $I_{PbBi}$
(b) Trajectory of a vortex in the junction. The vortex is pushed along the y direction from A to B, C, D, E, F

vortex location as A (0.075, 0.038). Then, the sample temperature was raised to 6.8K in order to keep the depinning current much lower than the corresponding nucleation current $I_n^{PbBi}$. Hence, the data shown in this part of section were taken at 6.8K.

We first applied a depinning current $I_{PbBi}$ of 20mA. The vortex was moved along the +y-axis to point B (0.12, 0.665). By reversing the current $I_{PbBi}$, the vortex can be moved in the negative y direction. A simple reversal of $I_{PbBi}$ did not push the vortex back to site A but instead a rather smaller current of -5mA moved the vortex to site C. Further increasing the current $I_{PbBi}$ moves the vortex to position D, E, and F. Their relative locations in the junction are marked in the trajectory in Fig. 4.10b. It is found the direction of the vortex is quite different from the direction of the Lorentz force. In the experiment, where we push the vortex along the x direction, we also found a little bit of side motion, in addition to the one along the direction of the Lorentz force. This presumably reflects the array of pinning potentials, created by the defects in the Pb film, seen by the vortex as it moves.

The $I_{co}/I_o$ plot of Fig. 4.10a shows the same plateau-like structure as in the Figures 4.7 and 4.8. The picture that emerges from these data is that slight increases in the Lorentz force often cause further motion of the vortex but at certain locations, there are plateaus of strong pinning where substantial increase in $I_{PbBi}$ or $I_{Pb}$ are needed to move the vortex.

Shown in Figures 4.11a through 4.11f, are those measured

(a)

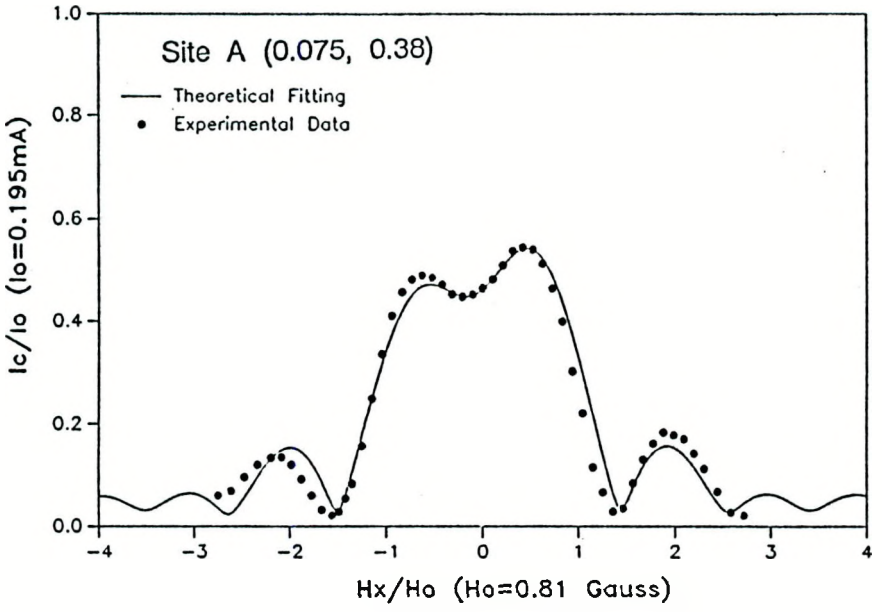


(b)

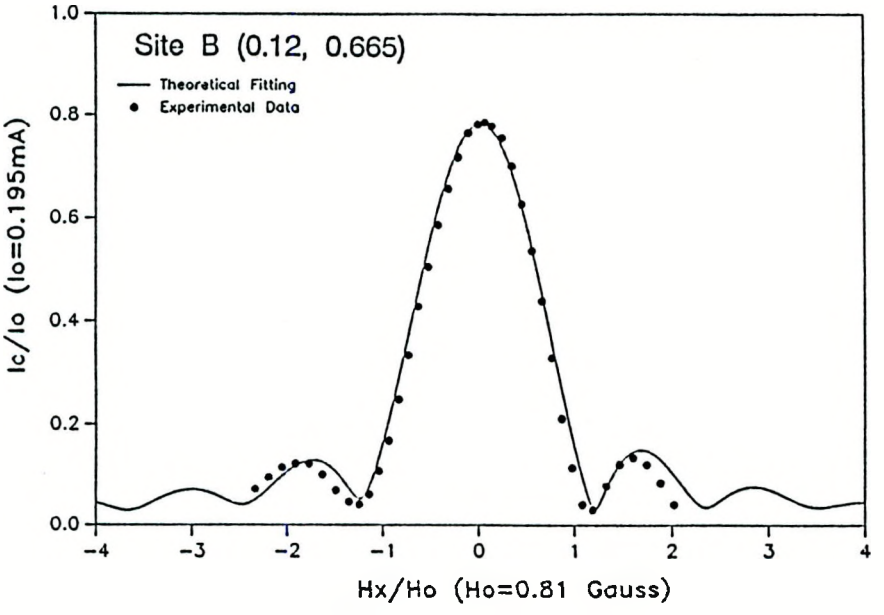


Fig. 4.11. Diffraction patterns for (a) site A, (b) site B

(c)

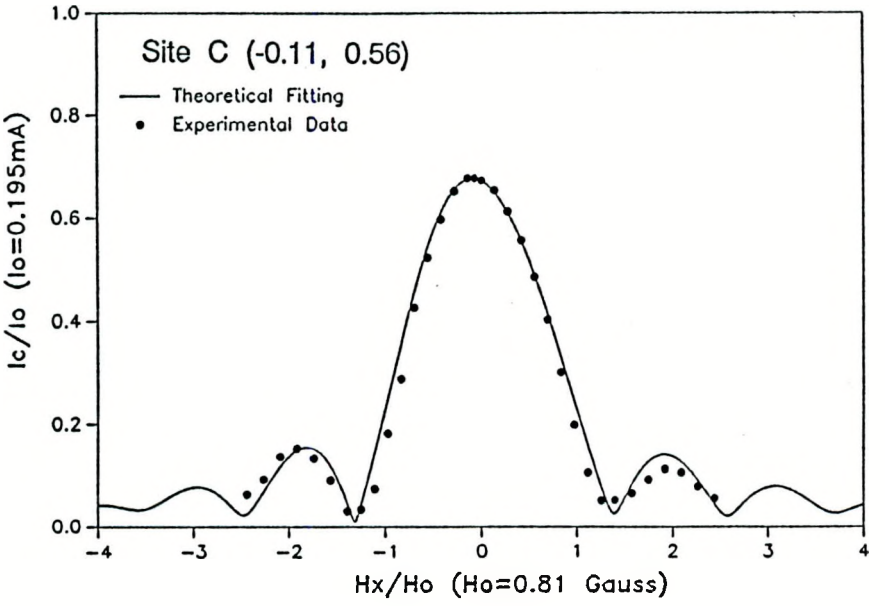


(d)

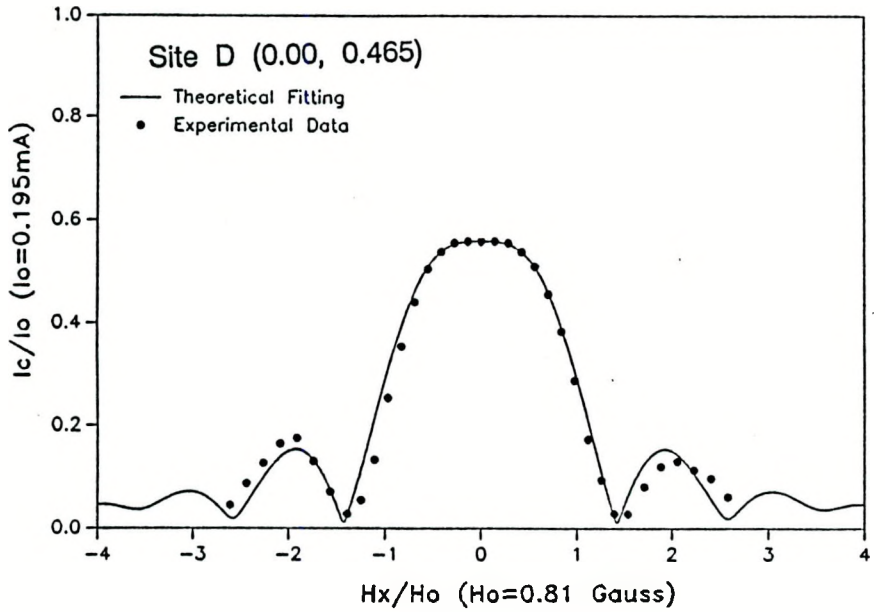


Fig. 4.11. (Continued)
(c) site C, (d) site D

(e)

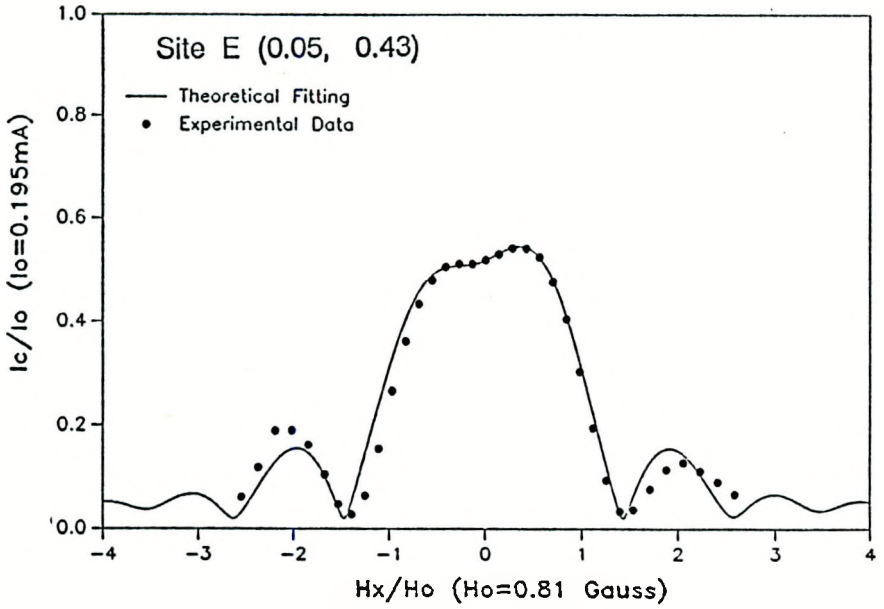


(f)

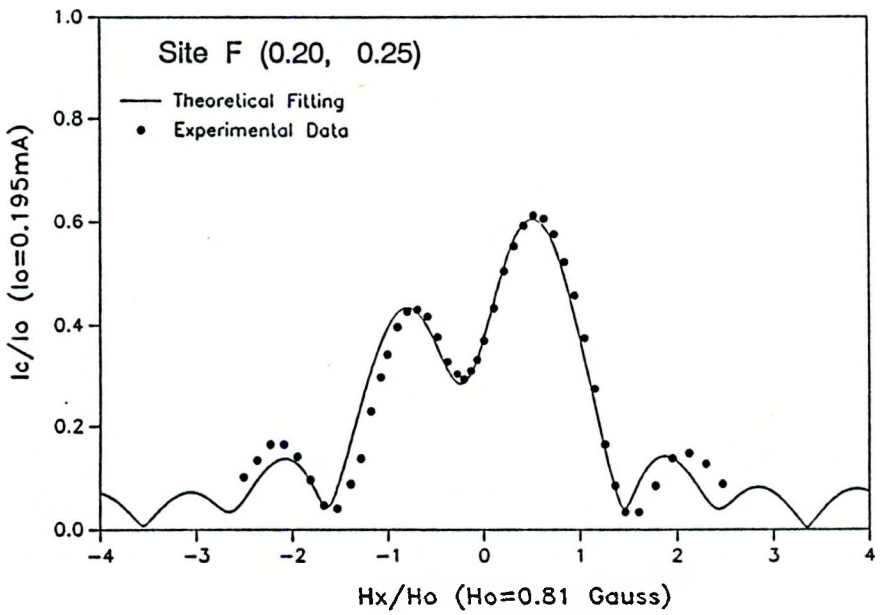


Fig. 4.11. (Continued)
(e) site E, (f) site F

diffraction patterns, together with their theoretical fittings. It is obvious to see that as the vortex gets closer to the edge of the junction, its diffraction pattern becomes more like a Fraunhofer pattern type.

4.2.3. Symmetry breaking and determination of the vortex type

Up to this point, we have not said anything about how we determined the type of the vortex nucleated in our junction and the quadrant where the nucleated vortex is pinned. This ambiguity arises from the geometric symmetry of a square junction. To solve this symmetry problem, we could break the symmetry by observing the motion of the vortex in response to the Lorentz force from an external perpendicular field.

For the bottom Pb film centered along the y-axis, as shown in Fig. 4.12a, the positive y direction transport current will nucleate a positive vortex at the film edge and push it to the second or third quadrant, while an equivalent negative vortex is pushed to first or forth quadrant, as shown in Fig. 4.12a, where ⊙ represents a positive vortex and ⊗ represents a negative vortex. The diffraction pattern, $I_c$ vs $H_x$, for any of the four locations is identical. But from the diffraction pattern, $I_c$ vs $H_y$, we found only locations #2 and #4 are possible, since the highest peak in the diffraction pattern happens on the $+H_y$ side which gives either a positive vortex in the +y half plane, or an equivalent negative vortex in the -y half plane (for example, see Fig. 4.5b). The other proof for this is to look at the direction

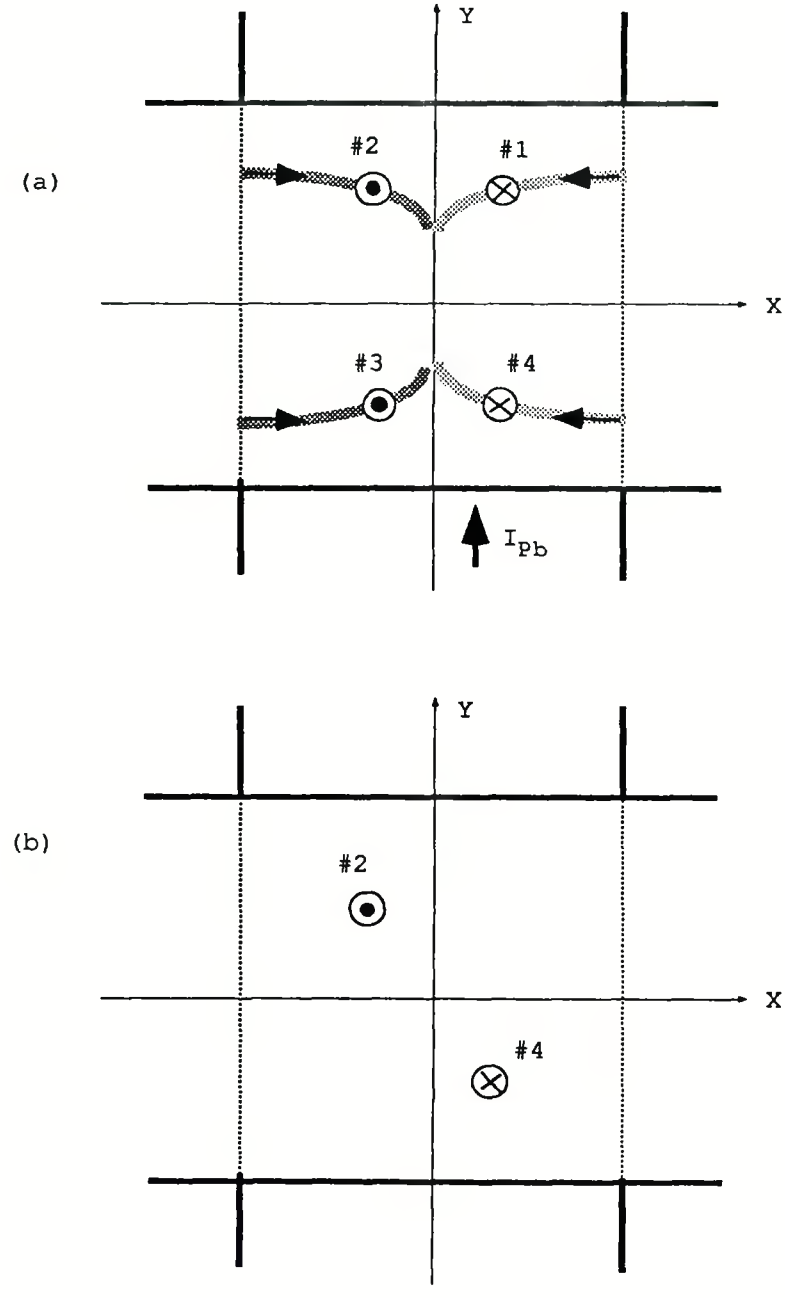


Fig. 4.12. (a) Four possible vortex locations as nucleate by transport current $I_{Pb}$, where ⊙ stands for a positive vortex, ⊗ for a negative one

(b) Two locations allowed as determined from the diffraction patterns, $I_c$ vs $H_x$ and $I_c$ vs $I_y$

of the motion of the vortex driven by the depinning current $I_{PbBi}$. Referring to the sketch shown in Fig. 4.9, a current $I_{PbBi}$ along +x will push a positive vortex along the positive y direction, but along the negative y direction for a negative vortex. The experimental results shown in Fig. 4.10. tell us the vortex actually moves toward the edge of the junction so that the only possible location allowed is either #2 or #4, as shown in Fig. 4.12b.

In order to distinguish the location #2 from #4, another depinning experiment via perpendicular magnetic field $H_\perp$ has been performed. This idea has been illustrated in part by Miller[14], and Hyun[16], in their earlier works. The perpendicular magnetic field $H_\perp$ produces a parallel magnetic field in the junction barrier as shown in Fig. 4.13, which in turn generate induced screening currents on the top surface of the bottom Pb film. These currents will push a positive vortex toward the edge, while pushing a negative one toward the center.

At 6.70k, we did such a vortex depinning experiment by using the perpendicular field $H_\perp$. It was found that the vortex starts moving toward the edge of the junction from location A, as shown in Fig. 4.7, when $H_\perp$ is equal to 0.9 Gauss, which is much less than the vortex nucleation field $H_\perp$ = 1.6 Gauss, at 6.70K, measured earlier. Consequently, the $I_c$ vs $H_x$ and $I_c$ vs $H_y$ diffraction patterns plus the direction of the motion of the vortex under the Lorentz force resulting from $I_{PbBi}$ and $H_\perp$ confirm that a vortex was nucleated in the second quadrant.

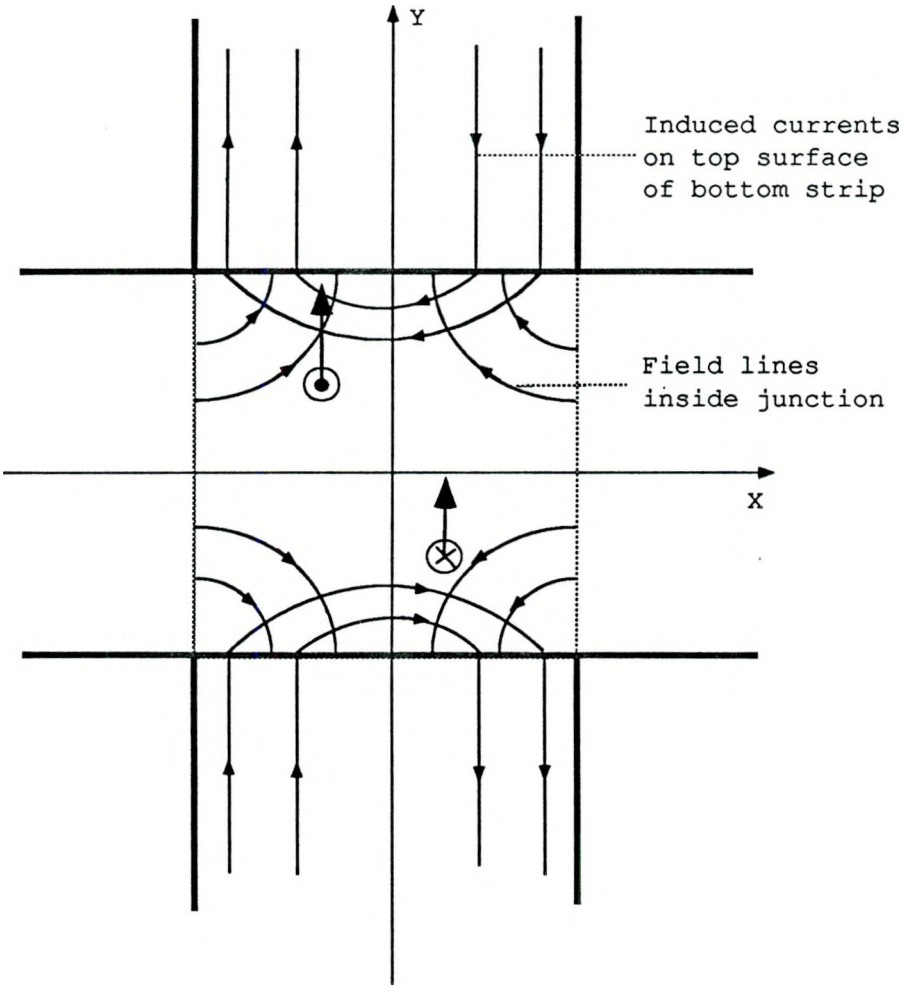


Fig. 4.13. The magnetic field lines in the junction barrier and induce screening currents on the top surface of the bottom Pb film generated by a perpendicular magnetic field $H_{\perp}$

## 4.3. Experimental Study on the Elementary Pinning Force $f_p$ in Pb Thin Film

### 4.3.1. Elementary pinning force in Pb thin film

The elementary pinning force, $f_p$, is studied through measuring the minimum amount of depinning current, $I_d$, applied to remove a single vortex from a particular pinning center. In measurement of the elementary pinning force $f_p$ in thin film Pb, it is important to know the spacial variation of the current density, J, so that the Lorentz force per unit length of vortex, $J\times\Phi_o/c$, can be related to the total current, $I_{Pb}$.

Yet, there has been no analytical solution available for the transport current density distribution in the junction area for a square cross-type junction. Barone et al.[48] obtained the current density distribution through analog modeling the electric field distribution in an electric bath which provides the same boundary conditions of the problem. Some approximate solutions to this problem have been used by Barone et al.[48] Hebard and Fulton[52]. According to their results, in the area about 30% of W/2 away from the edge of the film, where W is the width of the film, the current density distribution is similar to an isolated superconducting film. Here we use this approximation for a cross strip junction.

For our experiments, twice the penetration depth is less than the film thickness, which, in turn, is less than the film width, i.e., $2\lambda < d_s < W$. Hence, to a good approximation,[48,52] the current per unit width of the junction is given by

$$I' = (I_{Pb}/\pi)\cdot[(W/2)^2-x^2]^{-1/2} ,$$

where x is measured from the film center. Thus, the elementary pinning force on the vortex is

$$f_p = [(J\cdot\Phi_o)/c]\cdot d_s = (I'\cdot\Phi_o)/c ,$$

using Gaussian units where c is the speed of light. Near the center of the film, I' can be approximated by $I' = (2I_p)/(\pi W)$. Calling depinning current $I_d$ and using $W = 55\mu m$ and converting to practical units gives

$$f_p = 2.4\times10^{-11}\cdot I_d , \qquad (4.10)$$

in units of N/A.

In the measurement of $f_p$, we first nucleate a vortex and push it to a position very close to the center of the film so as to justify the condition for Eq. 4.10. The location of the vortex is determined from its diffraction pattern, as shown in Fig. 4.14a, labeled as site M (−0.008, 0.458). Then a transport current $I_{Pb}$ is applied to depin the vortex. In Fig. 4.15a (note the expanded scale) $I_{co}/I_c$ is plotted as a function of $I_{Pb}$, where each step corresponds to an individual pinning site. The location of site N (−0.038, 0.0463) marked on the plot is also determined by its diffraction pattern, as shown in Fig. 4.14b. The precision of measuring the position of the vortex and the depinning current $I_d$ is rather high, as illustrated in Fig. 4.15. Even the absolute value for each coordinate of actual pinning site M, N may not be the exactly same as shown In Fig. 4.14, the relative difference of the diffraction patterns is clearly resolvable in our experiments. Illustrated in Fig. 4.15b, are the patterns in the same plot. The

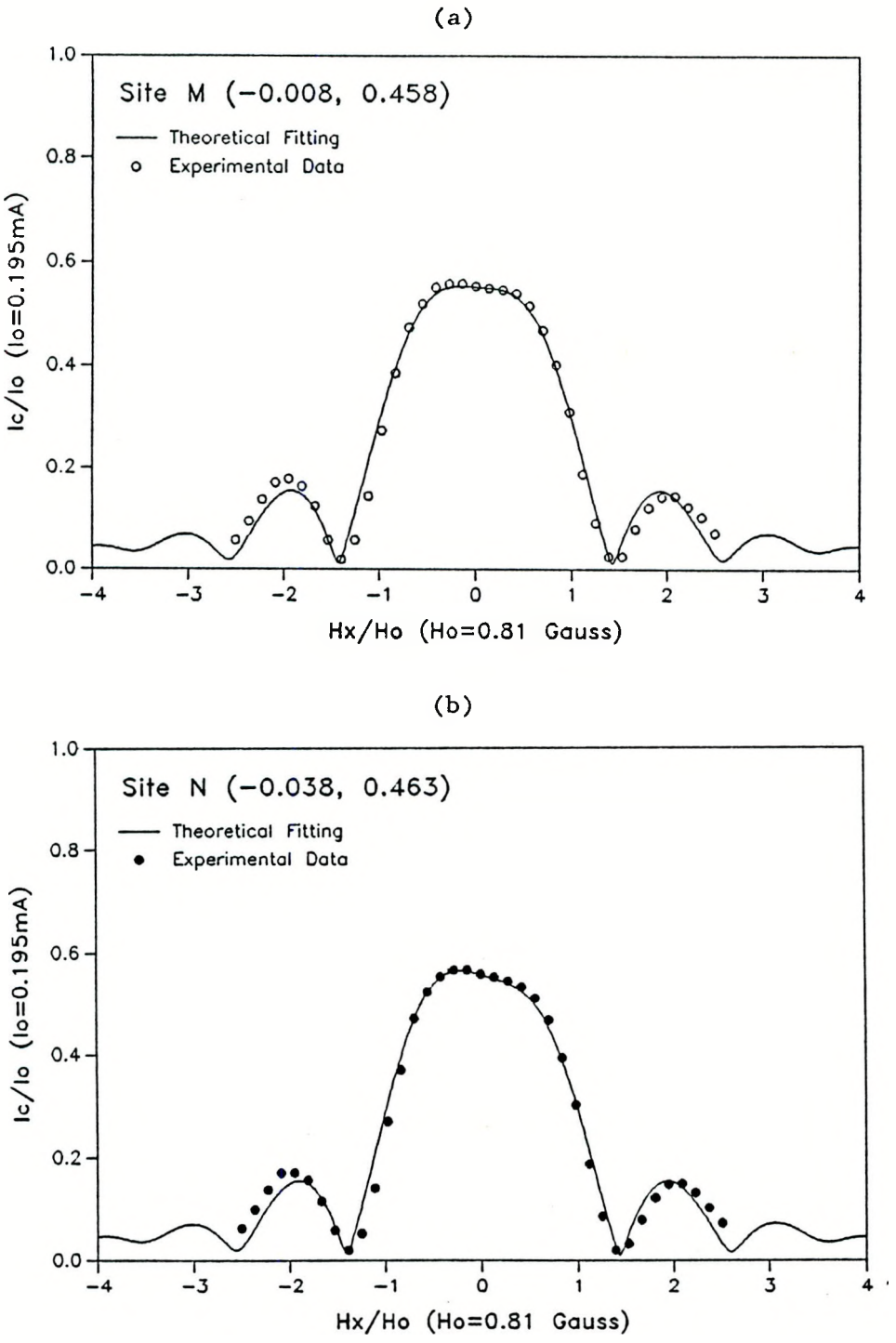


Fig. 4.14. Diffraction patterns for (a) site M, (b) site N

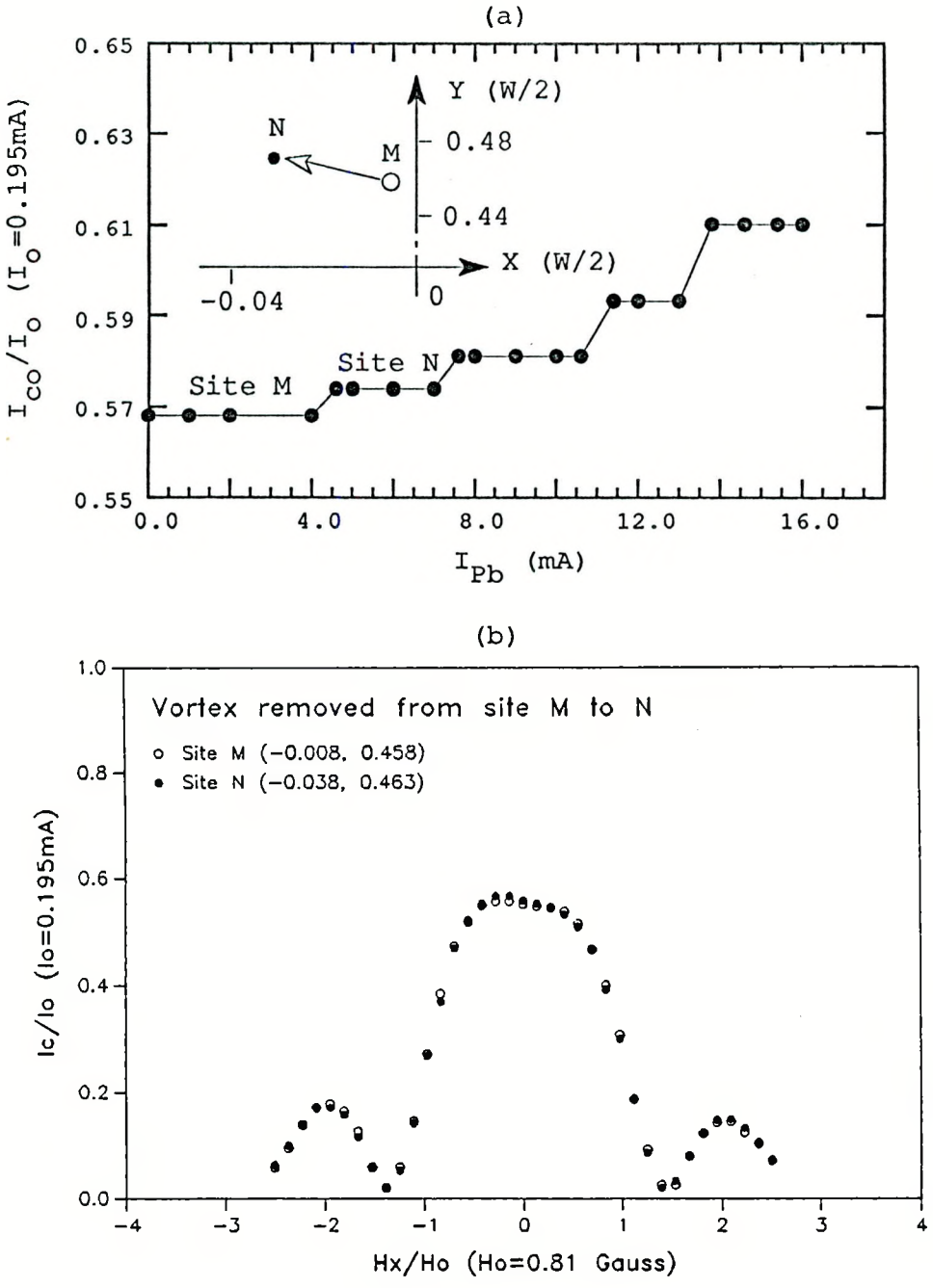


Fig. 4.15. Plot to show the precision in locating the vortex
(a) Expanded plot of $I_{co}/I_o$ vs $I_{Pb}$. The inset shows two pinning sites M and N located about 0.8$\mu$m apart
(b) Diffraction patterns for the sites M and N

relative positions are shown by the inset of Fig. 4.15a. Each step in Fig. 4.15a corresponds to a distance of about 1% of the junction width so the precision is rather good. In addition, the pinning sites are about 0.5$\mu$m to 1.0$\mu$m apart in this region of the Pb film.

The data shown in Fig. 4.15a were taken at 6.80K. A depinning current of 4.3 mA, for example, is required to remove the vortex from pinning site M, so that $f_p(M) = 1.03\times10^{-13}$ N or $f_p(M)/d_s = 2.7\times10^{-7}$ N/m. For pinning site N, $I_d$ = 7.3 mA, so $f_p(N) = 1.75\times10^{-13}$ N or $f_p(N)/d_s = 4.6\times10^{-7}$ N/m. These pinning forces are about a factor of 10 less than that found by Hyun et al.[13,15]

The calculation for $f_p$ so far does not include the vortex-image interaction. It is useful to estimate the range of such interaction as a comparison to what we calculated for $f_p$. Using $d_{eff}$ = 700nm, width of the junction W = 55$\mu$m, we get from Eq. 4.3.

$$f_m = (2.82\times10^{-14}\text{N})\cdot\textstyle\sum p(W/2)/|\mathbf{r}-\mathbf{r}_o| \ .$$

For a vortex at location M (-0.008, 0.458), the numerical value of $\sum p(W/2)/|\mathbf{r}-\mathbf{r}_o|$ has been calculated to be 0.58. Hence $f_m = 1.64\times10^{-14}$ N, it is about one order of magnitude smaller than the lowest value of $f_p$ directly calculated from $I_d$ so that the vortex-image interaction can be ignored in the calculation of elementary pinning force for those pinning sites about a distance of W/4 away from the edge of the junction.

### 4.4.2. Temperature dependence of $f_p$

For these Pb films, there seem to be two distinct regimes for

the temperature dependence of $f_p$ as shown by Fig. 4.16, where the depinning current for site M is plotted in two different ways. Above 6.85K, the vortex is not stable and seems to move spontaneously in response to the noise in the system. No values of $f_p$ are reported for this region.

No simple relation seems to describe the temperature dependence of $f_p$. Below 6.5K, the data show $I_d^{2/3}$ approximately linear in T as was found[13,15] for a PbBi film. Above 6.5K, the data show $I_d$ approximately linear in T. One possible interpretation of these results is that, close to $T_c$, surface roughness controls the scale of pinning potential.

The elementary pinning force is expressed as

$$f_p = \partial u(x)/\partial x \ , \tag{4.11}$$

where u(x) is the vortex energy, $u = [(H_c)^2/8\pi]\cdot(\pi\xi^2)\cdot d_s$, and $d_s$ is the length of the vortex, also the thickness of the superconducting film. By inserting the expression for the vortex energy, u, into Eq. 4.11, we obtain the elementary pinning force as

$$f_p = [(H_c)^2/8\pi]\cdot(\pi\xi^2)\cdot\delta d_s/\delta w \ , \tag{4.12}$$

so that

$$f_p \propto H_c^2\cdot\xi^2 \ ,$$

When the thickness variation, $\delta d_s$, contributes to the pinning potential, the scale of the surface roughness, $\delta w$, determines $\partial x$. Since $H_c \sim 1/(\lambda\xi)$, and $\lambda$ changes as $(1-T/T_c)^{-1/2}$ near $T_c$, we obtain

$$f_p \sim 1/(\lambda)^2 \sim (1-t)$$

near $T_c$, where $t = T/T_c$.

Direct measurements of the surface roughness by an optical

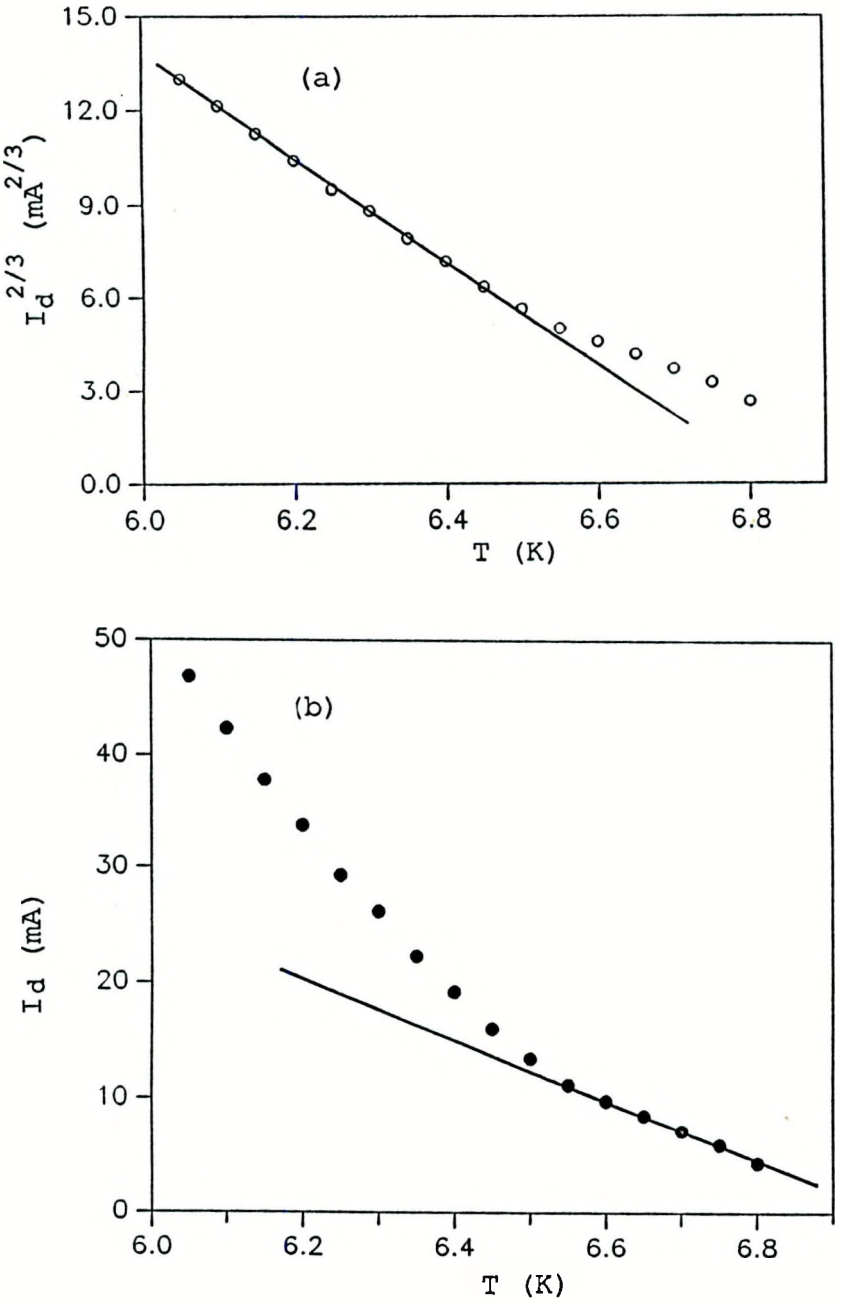


Fig. 4.16. Temperature dependence of $f_p$, or equivalently $I_d$
(a) Below 6.5K, $I_d^{2/3}$ is approximately linear in T
(b) Above 6.5K, $I_d$ is approximately linear in T

microscope and SEM indicate a scale of 0.5 $\mu$m to 1.0 $\mu$m for the surface roughness which is the same scale found as the average separation distance between two nearby pinning sites in the Pb film.

Now, let us make an estimation of the order of magnitude of the surface pinning force. For pure Pb, $H_c(0) = 803$ Gauss, so $H_c(6.6K) \approx 140$ Gauss. $\xi(6.6K)$ for pure Pb has the same order of magnitude as $\xi(0)$, which is ~ 800 Å. The average distance of two nearby pinning centers in these Pb films has been found between 0.5 $\mu$m to 1.0 $\mu$m so that we use 0.35 $\mu$m as an average value for $\delta w$. The value of the thickness variation, $\delta d_s$, has not been measured directly. As a rough estimation, we assume $\delta d_s$ to be around a few tens of nanometers in a 380 nm thick Pb film so we take $\delta d_s \approx 38$ nm (10% of $d_s$). By inserting all relevant parameters involved in Eq. 4.12, we get

$$f_p = 1.7 \times 10^{-13} \text{ N} ,$$

at 6.6K, which has the same order of magnitude as the measured value of $f_p$ at 6.6K, which is $2.2 \times 10^{-13}$ N.

If the defects from the interior of the Pb film cause the pinning, the scale of the pinning potential for $\partial x$ is replaced by the coherence length,[13,15] so that

$$\begin{aligned} f_p &\propto H_c^2 \cdot \xi \cdot d_s \\ &\sim 1/(\lambda^2 \cdot \xi) \\ &\sim (1-t)^{3/2} , \end{aligned}$$

near $T_c$, where $\xi \sim (1-t)^{-1/2}$ near $T_c$.

As a conclusion to the observed pinning behavior in thin film

Pb, the surface pinning seems to be more effective at T > 6.5K. However, at T < 6.5K, the interior pinning becomes more effective.

4.3.3. The window for depinning experiment

As long as there is only one single vortex in the junction, the analysis of the diffraction pattern to find the location of the vortex is straight forward. If there are two or more vortices present, however, it is very difficult to determine the location of either vortex uniquely, and the motion of many vortices is more complicated. Hence, to perform the vortex depinning experiment, it is necessary to keep the maximum depinning current, $I_d$, smaller than the minimum vortex nucleation current, $I_n$, so that there is only one vortex present. Otherwise, the experiment will be complicated by additional nucleation. Fortunately, there is a temperature regime for the Pb films, where the nucleation current, $I_n$, is much higher than the depinning current, $I_d$. This kind of window was also observed in the granular Al thin films by M. Fang[53] and in the PbBi thin films by O. B. Hyun[16].

Illustrated in Fig. 4.17, are the plots of $I_n^{Pb}$ vs T and $I_d^{Pb}$ vs T for pinning site M (−0.008, 0.458) to show the window for a pure Pb film, represented by the shaded area. It is obvious that the depinning experiments could be performed at least to 6.0K without exceeding the $I_n^{Pb}$ limit. As a contrast, the window for a PbBi film was found by Hyun[16] to be quite narrow, where the temperature has to be higher than 6.7K so that the region for the depinning experiments in a

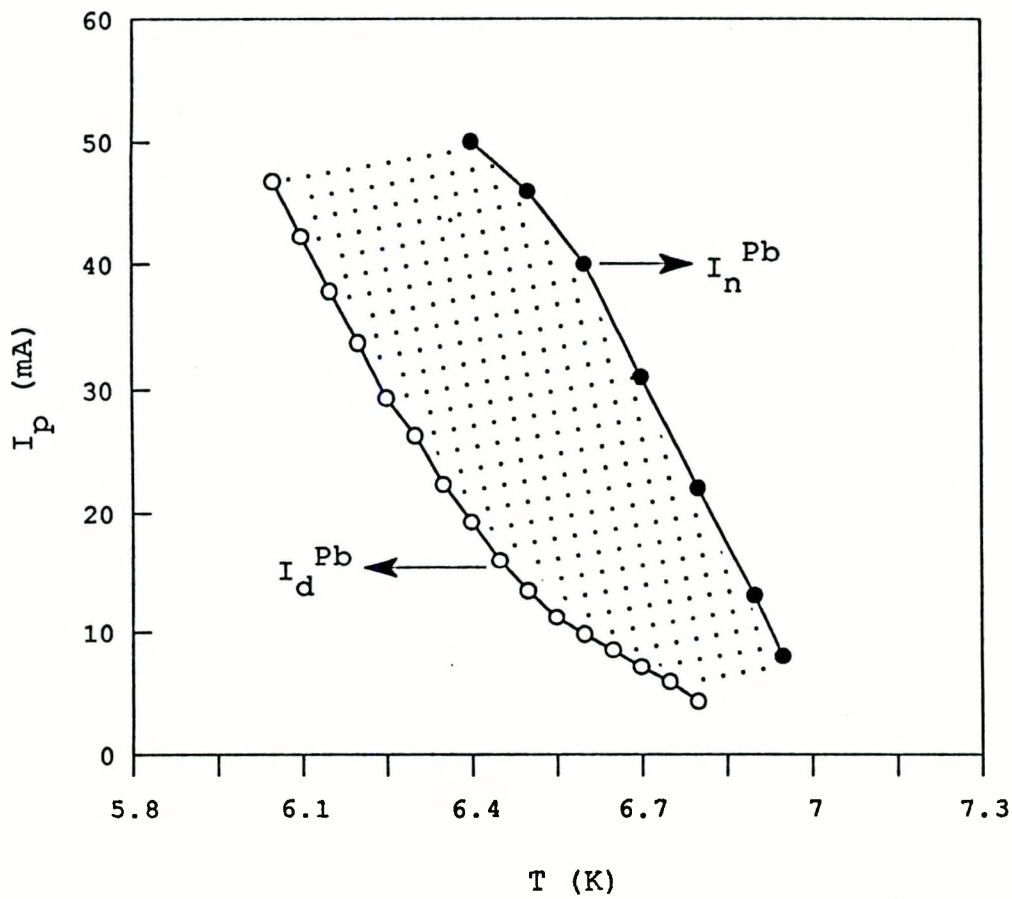


Fig. 4.17. Temperature dependence of vortex nucleation current, $I_n^{Pb}$, and vortex depinning current, $I_d^{Pb}$. The shaded region is the window for the vortex depinning experiments

PbBi film is much smaller than that in a Pb film. Presumably this is due to the low pinning nature of pure Pb.

## 4.4. Applications and Future Experiments

The basic concept of a flux shuttle, based on the motion of a single vortex, was demonstrated by Hyun and Finnemore.[13,15] The SNS Josephson junction used by them, however, has a very low junction resistance, in the range of a micro-ohm, so that a SQUID had to be used to detect the voltage signal which was of the order of a few tenths of a nanovolt. From a practical point of view, this makes the device slow and rather difficult to use in large junction arrays. Now, with this new family of SNIS Josephson junctions, the junction impedance has been increased to a few tens of ohms so that a conventional micro-voltmeter will suffice to detect the Josephson voltage in the range of tens of millivolts.

The way in which this particular junction could be used as a flux shuttle is illustrated in Fig. 4.18. Fig. 4.18a shows two vortex pinning sites A and B whose locations have been determined to be A (0.075, 0.38) and B (0.12, 0.665) from their diffraction patterns. In Fig. 4.18b, there are two zero magnetic field V-I characteristics marked A or B for the junction containing one single vortex A or B respectively. In performing the logic, the write operation can be done by moving the vortex in between sites A and B; the read operation

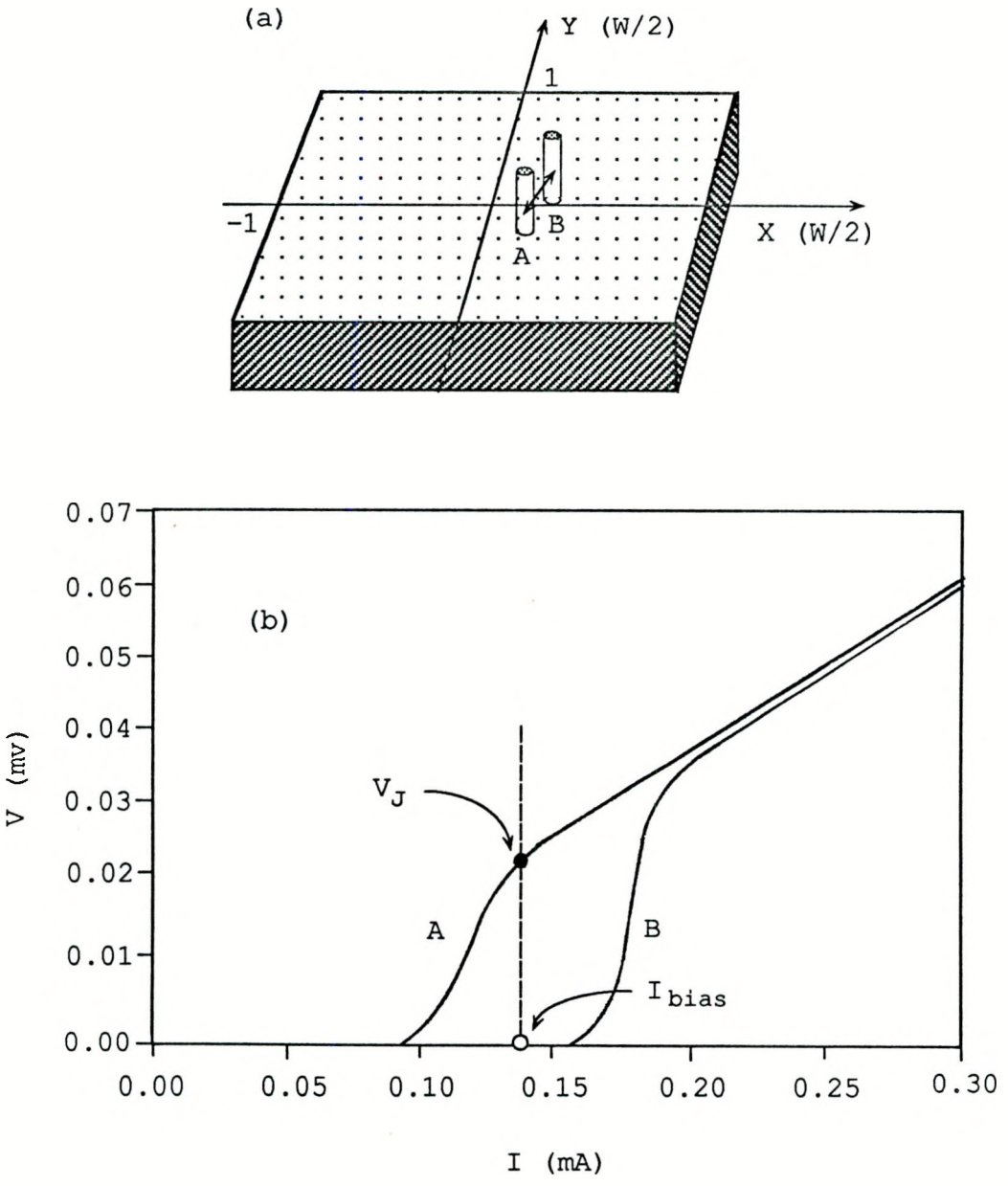


Fig. 4.18. Sketch to show the concept of a flux shuttle
(a) Two pinning sites A (0.075, 0.38) and B (0.12, 0.665)
(b) V–I curves for the junction containing a single vortex pinned at site A or B respectively. The voltage responses, $V_J$ and Ø at $I_{bias}$, serve as binary states

can be done by applying a proper amount of bias current, $I_{bias}$, and measuring the voltage $V_J$ or zero to read the vortex location A or B. Thus, two distinct voltage states $V_J$ and zero can be used to serve as binary states 1 and Ø.

In order to use this concept, it is necessary to control the motion of the vortex in between two distinct pinning sites such as site A or B, shown in Fig. 4.18. In the present work, the pinning centers inside the junctions are naturally formed defects and the motion between two pinning sites, separated by a large distance, is normally not reversible. Therefore, a specific path has to be artificially made so as to confine the vortex. Methods have been proposed by Hyun and Finnemore[16] to make the pair potential of a desired region lower than the other part of the superconducting film in the junction area.

By etching or milling a narrow ditch on the surface of the superconducting film, the thinner part provides a shorter vortex length and hence a lower vortex line energy so as to confine the vortex. Another method is to deposit a thin normal metal strip less than a hundred nanometers thick, and of submicron width on the substrate which is positioned just underneath the bottom superconducting film, or right on the top superconducting film. The order parameter of the superconducting film in this narrow region will be suppressed because normal electrons will reduce the pairing so that a vortex could be restricted inside this region. Using this method, the superconducting film could be maintained with good quality. With

sophisticated lithography technology, a submicron wide normal metal strip can be fabricated without too much difficulty. Cu or Ag narrow strip under the Pb layer of the Pb–Al–$Al_xO_y$–PbBi junction could be used to constrain the path of the vortex.

# CHAPTER 5. CONCLUSIONS

The motion of an Abrikosov vortex in cross-strip SNIS Josephson junctions has been studied. Vortices can be nucleated and moved to essentially any location in the junction so that this type of junctions is well suited for the development of an Abrikosov vortex memory devices.

After a vortex has been nucleated in the Pb strip, it can be pushed across the strip by currents along the Pb strip in the x direction. Alternatively, a current in the counter electrode can be used to induce currents across the Pb strip which will move the vortex along the y direction. Voltages in this SNIS junction are in the $\mu$V to mV range so conventional electronics will suffice for the detection. This is a vast improvement over the SNS devices that require a SQUID detector.

All of the basic physical phenomena of the SNS junctions also applies to the higher impedance SNIS junctions. The location of the vortex in the junction was determined from its diffraction pattern. The precision in reading the location of a vortex is about $\pm 0.3$ $\mu$m in a junction 55 $\mu$m wide. By moving the vortex around, many pinning centers in thin film Pb have been found. The vortex moves stepwise from one pinning center to another under the influence of depinning currents. The average nearby pinning centers in these Pb films are separated about 1.0 $\mu$m.

The elementary pinning force $f_p$ in pure Pb has been found to be

on the order of $10^{-13}$ N, a value much smaller than that found for Pb–Bi at the same reduced temperature $t = T/T_c = 0.9$. Detailed studies show that, generally, the pinning force is asymmetric and differs from one pinning center to another. The temperature dependence of $f_p$ in the Pb film for one particular pinning center M (–0.008, 0.458) has been measured at temperature lower than 6.85K. It was found $f_p \sim (1-T/T_c)$ above 6.5K, $f_p \sim (1-T/T_c)^{2/3}$ below 6.5K. For temperatures higher than 6.90K, the vortex was found not to be stable. The depinning current for the pinning site M was much less than the vortex nucleation current so that the experiment on vortex motion can be done at temperatures down to at least 6.0K.

# BIBLIOGRAPHY


1. A. M. Cambell and J. E. Evetts, Adv. Phys. **21**, 199 (1972).
2. A. I. Larkin and Y. N. Ovchinnikov, J. Low Temp. Phys. **34** 409 (1979).
3. E. V. Thuneberg, J. Kurkijarvi and D. Rainer, Phys. Rev. Lett. **48**, 1853 (1982); E. V. Thuneberg, J. Kurkijarvi and D. Rainer, Phys. Rev. B **29**, 3913 (1984).
4. P. H. Kes, IEEE Transactions on Magnetics, Vol. Mag-**23**, No.2.
5. M. Daeumling, J. M. Seuntjeus and D. C. Larbalestier, Nature **346**, 332 (1990).
6. T. L. Hylton and M. R. Beasley, Phys. Rev. B **41**, 11669 (1990).
7. G. J. Dolan et al. Phys. Rev. Lett. **50**, 337 (1990).
8. T. A. Fulton, A. F. Hebard, L. N. Dunkleberger and R. H. Eick, Solid State Commun. **22**, 493 (1978); A. F. Hebard and R. H. Eick, J. Appl. Phys. **40**, 848 (1982).
9. H. R. Kerchner, J. Low Temp. Phys. **50**, 337 (1983).
10. J. Mannhart et al. Phys. Lett. A **122**, 439 (1987).
11. A. DasGupta et al. Philos. Mag. **38**, 367 (1978).
12. L. H. Allen and J. H. Claassen, Phys. Rev. B **39**, 2054 (1989).
13. O. B. Hyun, D. K. Finnemore, L. A. Schwartzkopf and J. R. Clem, Phys. Rev. Lett. **58**, 599 (1987).
14. S. L. Miller, K. R. Biagi, J. R. Clem and D. K. Finnemore, Phys. Rev. B **31**, 2684 (1985).

15. O. B. Hyun, J. R. Clem and D. K. Finnemore, Phys. Rev. B 40, 175 (1989).

16. O. B. Hyun, Ph.D. dissertation, Iowa State University, (1987).

17. B. D. Josephson, Adv. Phys. **14**, 419 (1965).

18. A. Barone and G. Paterno, *Physics and Application of the Josephson Effect* (John Wiley & Sons, 1982), p. 69.

19. J. R. Clem, Private Communication, Physics Department, Iowa State University (unpublished).

20. A. J. Gilbert et al. Solid State Comm. **31**, 109 (1978).

21. P. Nedellee, L. Domoulin and E. Guyon, J. of Low Temp. Phys. **24**, 663 (1976).

23. J. L. Milles and P. H. Smith, J. Electroch. Soc. **110**, 1240 (1963).

24. J. A. Blackburn, H. J. Smith and N. L. Rowell, Phys. Rev. B **11**, 1053 (1975).

25. J. Clarke, Phys. Rev. B 4, 2963 (1971).

A. Barone, and G. Paterno, *Physics and Application of the Josephson Effect* (John Wiley & Sons, 1982), p. 121.

26. N. F. Pedersen, J. Mygrid et al. LT15, 1232–1233 (1978).

27. R. F. Broom, J. of Appl. Phys. **47**, 5432 (1976).

28. P. K. Hansma and G. I. Rocklin, J. of Appl. Phys. 43, 4721 (1972).

29. O. H. Soeresen, J. Mygind and N. F. Pedersen, Phys. Rev. Lett. **39**, 1018 (1977).

30. N. L. Rowell and H. J. T. Smith, Can. J. Phys. **54**, 223 (1976).

31. J. P. Romagnan, A. Gilabert, J. C. Noiray and E. Guyon, Solid State Commun. 14, 83 (1974).

32. N. R. Werthamer, Phys. Rev. **36**, 2240 (1963).

33. P. G. de Gennes, Rev. Mod. Phys. **36**, 225 (1964).

34. A. Barone and G. Paterno, *Physics and Application of the Josephson Effect* (John Wiley & Sons, 1982), p. 200.

35. O. B. Hyun, Ph.D. dissertation, Iowa State University, (1987).

36. S. Greenspoon and H. J. T. Smith, Can. J. Phys. **49**, 1350 (1976).

37. C. Kittel, *Solid State Physics* (John Wiley & Sons, 1976), p. 154.

38. C. Kittel, *Solid State Physics* (John Wiley & Sons, 1976), p. 167.

39. A. B. Pippard, Phil. Tran. Roy. Soc. **A 250**, 325 (1957).

40. J. Clarke, Proc. Roy. Soc. (London), Ser. **A**, **308**, 447 (1969).

41. A. Gilabert et al. Solid State Commun. **31**, 109 (1979).

42. O. B. Hyun and D. K. Finnemore, J. Appl. Phys. **60**, 1214 (1986).

43. R. P. Huebener, R. T. Kampwirth and J. R. Clem, J. Low Temp. Phys. **6**, 275 (1972).

44. R. P. Huebener, *Magnetic Flux Structures in Superconductors* (Springer-Verlag, Berlin-Heidelberg, 1979), Chapter 4.

45. M. Tinkham, *Introduction to Superconductivity* (McGraw-Hill, New York, 1975), p. 210-211.

46. J. R. Clem, Phys. Rev. **B** 12, 1742 (1975).

47. J. R. Clem, R. P. Huebener and D. E. Gallus, J. Low Temp. Phys. **12**, 449 (1971).

48. A. Barone et. al. J. Appl. Phys. **53**, 5802 (1982).

49. M. Tinkham, Phys. Rev. **129**, 2413 (1963); M. Tinkham, Rev. Mod.

Phys. **36**, 268 (1964).

50. G. D. Cody and R. E. Miller, Phys. Rev. **173**, 481 (1968).

51. J. R. Clem, Private Communication, Physics Department, Iowa State University (unpublished).

52. A. F. Hebard and T. A. Fulton, Phys. Rev. Lett. **35**, 1310 (1975).

53. M. M. Fang, Ph.D. dissertation, Iowa State University, (1986).

# ACKNOWLEDGMENTS

The author wishes to express deep appreciation to Dr. D. K. Finnemore for his valuable guidance throughout the course of this research and especially for his continuing encouragement and support for the work I have done in his group.

The author also wishes to thank Dr. O. B. Hyun for his valuable assistance and discussion concerning laboratory techniques. Thanks are also extended to Mr. J. E. Ostenson for his advice in so many areas; to Dr. J. R. Clem for his helpful discussion in the theoretical aspects of this work; to the post-doctorals and students in Dr. Finnemore's group for many inspiring discussions.

Finally, the author also wishes to thank his wife for her support and understanding during the final year this work was carried out.

This work was performed at Ames Laboratory under contract no. W-7405-eng-82 with the U. S. Department of Energy. The United States government has assigned the DOE Report number IS-T 1565 to this thesis.